"Every individual matters.
Every individual has a role to play.
Every individual makes a difference."
Jane Goodall

Table of Contents

1. INTRODUCTION 12

1.1 The Clinical Context: The Need for Continuous and Personalized Monitoring 12

1.2 From the Point Of Care (PoC) Devices at Wearable Technologies 1

1.2.1 Wearable devices: an overview 2

1.3 Sensors in Healthcare 2

1.3.1 Introducing Sensors 2

1.3.2 Electrochemical Sensor 3

1.3.3 Electrochemical Sensors in Healthcare 5

2. BIOCOMPATIBLE MATERIALS AND FABRICATION TECHNIQUES FOR WEARABLE SENSORS 7

2.1 Material Biocompatibility: A Primary Consideration in Wearable Sensor Development 7

2.2 Materials for Substrates and Supports 8

2.2.1 PDMS 8

2.2.2 Paper-based substrates 9

2.2.3 Polyimide (Kapton) 10

2.2.4 Other materials 11

2.3 Fabrication Techniques For Wearable Electrochemical Sensors 11

2.3.1 Screen-printing 12

2.3.2 3D printing 13

2.3.3 Laser-Induced Graphene 15

2.3.4 Other Fabrication Techniques 15

2.4 Modification of the Sensing Area 17

2.4.1 Metal Nanoparticles 17

2.4.2 Conductive Polymers 18

2.4.3 Molecularly Imprinted Polymers (MIPs): Biomimetic Receptors for Selective Sensing 19

2.5 Conclusions 21

3. DEVELOPMENT OF A POC SENSOR FOR LITHIUM MONITOTING IN BIPOLAR DISORDER 22

3.1 Mental Disorders and The Imperative For Personalized Pharmacotherapy 22

3.2 The Role of Lithium in Bipolar Disorder Management 23

3.3 Lithium Detection In Peripheral Biofluids Using a Smart Electrochemical Sensor 24

3.3.1 State of Art 24

3.3.2 Chemicals 25

3.3.3 Apparatus 25

3.3.4 Preparation of (Au&Ag)NPs-modified Graphite Screen-Printed Electrodes 26

3.3.5 Study of the Electrochemical Performance of (Au&Ag)NPs-Modified Screen-Printed Electrodes 26

3.3.6 Preparation of Lithium Sensor 27

3.3.7 Lithium Detection 27

3.3.8 Selectivity Assessment via the Fixed Interference Method (FIM) 28

3.3.9 Validation in Synthetic Biofluids as Proof-of-Concept 28

3.3.10 Results and Discussion 29

3.3.10.1 (Au&Ag)NPs Electrodeposition and Surface Characterization 29

3.3.10.2 Optimization of The Amount of Lithium Selective Membrane 32

3.3.10.3 Optimization of The Supporting Electrolyte Concentration 33

3.3.10.4 Lithium Detection in Standard Solutions 35

3.3.10.5 Interference Study 36

3.3.10.6 Analysis In Synthetic Saliva and Sweat 36

3.3.11 Conclusion 37

3.4 Acknowledgment 38

4. TOWARD WEARABLE NEUROLOGICAL HEALTH MONITORING: A SWEAT-BASED SENSOR FOR DOPAMINE 39

4.1 Neurological Disorders and the Diagnostic Challenge 39

4.2 The Potential Role of Sweat In the Early Diagnosis of Neurological Disorders 40

4.3 Sweat Dopamine Monitoring Using Amino Acid-Based Electrochemical Sensors 41

4.3.1 State of Art 41

4.3.2 Chemicals 42

4.3.3 Apparatus 43

4.3.4 Electrochemical Sensors Modifications 43
4.3.5 Electrochemical Characterisation 44
4.3.6 Dopamine Detection with Cyclic Voltammetry (CV) and Differential Pulsed Voltammetry (DPV) in Standard solutions 45
4.3.7 Sensor Validation in Artificial Sweat 46
4.3.8 Results and Discussion 46
4.3.8.1 Modification of GSPEs with Poly-L-Cysteine (PLC), Poly-l-Aspartic Acid (PLA) and Gold Nanoparticles 46
4.3.8.2 Electrochemical Characterisation of Modified GSPEs 51
4.3.8.3 Dopamine Detection in Buffer Solutions 57
4.3.8.4 Selectivity Assessment 58
4.3.8.5 Real Sample Analysis: Artificial Sweat Sample 59
4.3.9 Conclusions 61

4.4 Acknowledgment 62

5. WEARABLE THERAPEUTIC DRUG MONITORING: A SWEAT-BASED SENSOR FOR LEVODOPA IN PARKISON'S DISEASE MANAGEMENT 63

5.1 Therapeutic Drug Monitoring in Neurological Disorders 63

5.2 Plasma-Treated Carbon Sensor coupled to PDMS-based Microfluidic platform for the Determination of Levodopa in Sweat 64

5.2.1 State of Art 64
5.2.2 Chemicals 66
5.2.3 Apparatus 67
5.2.4 Microfluidic Network Preparation and Characterisation 68
5.2.5 Plasma Treatment of the Carbon Sensor and Electrochemical and Morphological Characterization 69
5.2.6 Dopamine and Levodopa Electrochemical Detection 70
5.2.7 Real Sample Analysis in Microfluidic Chamber 70
5.2.8 Computational Fluid Dynamics (CFD) Simulation 72
5.2.9 Results and Discussion 72
5.2.9.1 Principle and Design of the PDMS-based Microfluidic Device 72
5.2.9.2 Electrochemical Characterisation of Plasma-Treated CSPE 76
5.2.9.3 Sweat Analysis In Microfluidic Chamber 83
5.2.10 Conclusion 85

5.3 Acknowledgment 86

6. RETHINKING AFFINITY SENSING: HOW SYNTHETIC RECEPTORS AND LASER-INDUCE GRAPHENE ELECTRODES ARE REDEFINING WEARABLE ELECTROCHEMICAL ANALYTICS 87

6.1 Affinity Sensing in Clinical Trials....87

6.2 Electrochemical Affinity Sensing Paradigm....88

6.3 Bio-Inspired Receptors on Laser-Induced Graphene electrodes for Chronic Disease Monitoring 89

6.3.1 State of Art....90

6.3.2 Chemicals....91

6.3.3 Apparatus....91

6.3.4 Synthetic Receptor Functionalisation....91

6.3.5 Rebinding Assay....92

6.3.6 Results and Discussion....92

6.3.6.1 Surface Characterization: Direct Visualization of NanoMIPs Immobilization on LIG 92

6.3.6.2 Functional Validation: Comparative Rebinding Performance on SPGE and LIG Electrodes 94

6.3.6.3 Specificity Assessment....95

6.3.7 Conclusion....97

6.4 Acknowledgment....98

7. REMARKABLE CONCLUSIONS.... 100

8. REFERENCES 104

PREFACE

Abstract

The convergence of global health trends, including ageing populations, the rinsing prevalence of chronic neurological and psychiatric disorders, and the growing imperative for sustainable healthcare systems, has catalysed a fundamental shift in medical practice. The vision of personalised medicine, which tailors' therapeutic strategies to the individual patient, has moved from a theoretical ideal to an operational necessity. However, its realisation is critically hampered by a technological gap: the lack of tools for frequent, unobtrusive, and quantitative monitoring of key physiological and pharmacological parameters outside of clinical settings. Indeed, conventional diagnostic methods, reliant on centralised laboratory analysis of blood samples, provide high accuracy but are inherently incompatible with the demands of continuous, longitudinal health management. Their invasiveness, cost, and logistical complexity create a significant burden for patients and clinicians alike, often leading to suboptimal therapeutic outcomes. This persistent challenge has defined the central ambition of this doctoral thesis: to contribute to bridging this gap by advancing the frontier of wearable electrochemical sensors. These devices promise to transform episodic measurements into continuous data streams, offering a dynamic window into an individual's health status. The journey documented in this thesis is rooted in the conviction that for such sensors to transition from promising prototypes to integral components of daily healthcare, their development must be guided by a holistic framework that transcends mere analytical performance. The REASSURED criteria, encompassing Real-time connectivity, Ease of specimen collection, Affordability, Sensitivity, Specificity, User-friendliness, Rapid and robust operation, Equipment free, and Deliverability, served as the foundational compass for this research, constantly reminding us that a sensor's ultimate value is determined not in buffer solution, but in the complex, variable context of a patient's life.

This work is structured to reflect a logical progression from establishing the clinical and technological foundations to the integration of functional prototypes and the exploration of novel sensing paradigms.

- *Chapter 1* introduces the clinical context, outlining the imperative for continuous and personalised monitoring in modern healthcare. It traces the evolution from centralised laboratory analysis to Point-of-Care and, ultimately, wearable

technologies, positioning electrochemical sensors as a key enabler within the Healthcare 4.0 paradigm.

- *Chapter 2* provides the essential material science toolkit, detailing the biocompatible substrates, fabrication techniques, and surface modification strategies that form the physical and chemical backbone of any wearable sensor. It discusses materials such as polyimide, polydimethylsiloxane (PDMS), and paper, alongside techniques including screen-printing, 3D printing, and laser induced graphene, as well as the critical role of nanomaterials and polymers in crafting the sensing interface.
- *Chapter 3* details the development of a Point-of-Care potentiometric sensor for monitoring lithium in bipolar disorders. It demonstrates how a graphite screen-printed electrode, modified with a bimetallic nanostructured and a lithium-selective membrane, can achieve sensitive and selective detection in synthetic sweat and saliva, offering a viable route for non-invasive therapeutic drug monitoring.
- *Chapter 4* addresses the need for greater biocompatibility in long-term wearables by developing a sweat-based sensor for the neurotransmitter dopamine. This work centres on an electrochemical platform constructed from the biocompatible polymer poly-L-cysteine and electrodeposited gold nanoparticles, validating its performance in undiluted artificial sweat for potential neurological health monitoring.
- *Chapter 5* represents a significant step towards system integration, presenting a wearable therapeutic drug monitoring platform for levodopa in Parkinson's disease. This work combines a plasma-treated carbon sensor with a hydrophilic PDMS-based microfluidic patch for passive sweat sampling. The single-step plasma treatment serves the dual purpose of activating the sensor and sealing the microfluidic system, resulting in an integrated device capable of quantifying levodopa in a complex sweat matrix.
- *Chapter 6* undertakes a paradigm shift in affinity sensing by exploring the integration of fully synthetic, peptide-imprinted nanoMIPs with flexible laser-induced graphene electrodes. This "nanoMIP-on-LIG" approach aims to overcome the limitations of biological receptors, demonstrating preserved molecular recognition and enhanced signal transduction on a durable, scalable substrate suitable for next-generation wearable diagnostic.

SCIENTIFIC PRODUCTION

Papers

- Vitale, I.A.; Selvolini, G.; Marrazza, G. Smart Sensor for Lithium Detection: An Environmental Application. *Chemosensors* **2023**, *11*, 77. https://doi.org/10.3390/chemosensors11020077
- I. A. Vitale, N. Fuochi, D. Martella, C. Parmeggiani, G. Marrazza, and I. Palchetti, "Skin-contact wearable electrochemical biosensing tools: A perspective for the wellbeing of neurological patients," TrAC Trends in Analytical Chemistry, vol. 180, p. 117965, Nov. 2024, doi:10.1016/j.trac.2024.117965.
- I. A. Vitale, G. Selvolini, S. Failli, C. Truzzi, G. Marrazza, Mercury Detection in Novel Foods by a Smart Pocket Sensor, Electroanalysis 2024, 36, e202400192. https://doi.org/10.1002/elan.202400192
- Giovanna Marrazza, Murugan Ramalingam, Abinaya Jaisankar, Lijia Cheng, Giulia Selvolini, Ilaria Antonia Vitale, Advancements and emerging technologies in biosensors for rapid and accurate virus detection, TrAC Trends in Analytical Chemistry, Volume 172, 2024, 117609, ISSN 0165-9936, https://doi.org/10.1016/j.trac.2024.117609.I.
- I. A. Vitale, N. Fuochi, R. Rossi, M. Catarzi, D. Martella, C. Parmeggiani, G. Marrazza, and I. Palchetti, "Plasma-treated carbon sensor coupled to a microfluidic platform for the determination of levodopa in sweat, Electrochimica Acta, Volume 559,2026,148559, ISSN 0013-4686, https://doi.org/10.1016/j.electacta.2026.148559.

Proceedings

- Vitale, I.A., Selvolini, G., Marrazza, G. (2025). Lithium Detection in Peripheral Biofluids Using a Smart Electrochemical Sensor. In: Conoci, S., Di Natale, C., Prodi, L., Valenti, G. (eds) Sensors and Microsystems. AISEM 2024. Lecture Notes in Electrical Engineering, vol 1334. Springer, Cham. https://doi.org/10.1007/978-3-031-82076-2_4
- Vitale, I.A.; Selvolini, G.; Truzzi, C.; Marrazza, G. Smart Sensor for Mercury Detection in Novel Food. *Proceedings* **2024**, *97*, 232. https://doi.org/10.3390/proceedings2024097232

- Vitale, I.A.; Palchetti, I.; Marrazza, G. Developing a Wearable Sensing Platform for Well-Being Monitoring in Individuals with Dopamine-Related Neurological Disorders. *Proceedings* **2024**, *104*, 35. https://doi.org/10.3390/proceedings2024104035

***In-Fieri* Materials**

- I. A. Vitale, I. Palchetti, G. Marrazza, Amino Acid-Based Electrochemical Sensor for Monitoring Dopamine in Sweat, Brazilian Journal of Chemistry, 2025. **(accepted)**

1. INTRODUCTION

1.1 THE CLINICAL CONTEXT: THE NEED FOR CONTINUOUS AND PERSONALIZED MONITORING

In the last decade, medical practice has been shaped by a new paradigm centred on personalised therapies and continuous monitoring of a plethora of physiological parameters, which is essential for understanding and managing numerous diseases. A key enabler of this shift is *telemedicine***,** defined by the World Health Organization (WHO) as 'the delivery of healthcare services across distance by all healthcare professionals using information and communication technologies for the exchange of valid information, for the diagnosis, treatment and prevention of diseases and injuries' [1,2]

While modern digital technologies have solidified telemedicine as a cornerstone of contemporary healthcare, its conceptual foundation is not new. The evolution of telemedicine has, in fact, closely followed the progress of communication technologies. Early inventions, such as telegraph and telephone, first introduced the possibility of remote medical consultation. This concept expanded exponentially with the advent of the internet and continues to evolve with current digital tools [3,4].

Indeed, the widespread usage of wireless tolls – such as Wi-Fi, cellular networks (including 4 and 5G), and Bluetooth Low Energy (BLE) - has empowered the scientific and engineering community to significantly enhance device performance [5]. This progress has facilitated the creation of a seamlessly connected world, paving the way for the rise of telemedicine and telehealth as integral component of daily life [4]. This technological convergence is driving the adoption of new healthcare approaches, notably *precision medicine* [6] and *personalized medicine* [7], which aim to tailor medical decisions and treatments to individual patient characteristics.

Although these two terms are used interchangeably, a nuanced distinction exists [8]. *Precision Medicine* generally refers to an approach that categorises patients into sub-groups based on shared biomarkers, such as genetic profiles, to determine the most effective therapeutic strategy for their specific type of disease . It moves away from the "one-size-fits-all" model by using tools like genomic sequencing to target specific molecular alterations [9]. On the other hand, *Personalised Medicine*, can be considered a

broader, more holistic concept. It encompasses not only the molecular and genetic dimension but also factors such as patients' lifestyle, environment, and preferences to design a truly unique care-delivery plan for each individual [10]. In this sense, precision medicine is a powerful tool that *enable* the broader vision of personalized medicine.

Given these considerations, it becomes evident that analytical chemistry plays a pivotal role in this framework. It is responsible for the design, development, optimization, and validation of the methodologies and technologies that enable the quantification and monitoring of specific molecules. This is essential for improving diagnoses and developing tailored therapies, while simultaneously leveraging new device fabrication techniques to ensure a seamless integration of wireless systems, ultimately contributing to the realization of the *Healthcare 4.0* paradigm [11,12].

1.2 From the Point Of Care (PoC) Devices at Wearable Technologies

In order to deeply understand the evolution of medical devices over recent decades- a progression central to realizing *Healthcare 4.0*- it is essential to begin by examining conventional techniques used for parameter determination. These established methods, while foundational, highlight the limitations that Point-of-Care (PoC) devices and subsequent wearable technologies aim to overcome.

Traditionally, the gold standard for clinical diagnosis has relied on centralized laboratory analysis [13]. This process involves the collection of biological samples such as blood or urine from the patient, their transportation to a specialized lab, processing by trained personnel, and analysis using large, high-throughput instruments like spectrophotometers or chromatographs [14–17].

While this approach provides highly accurate results, it introduces significant delay -often hours or even days- between sample collection and the availability of results for the clinician. This time lag, coupled with the need for complex logistics and the excessive costs, makes the traditional laboratory model unsuitable for situations requiring immediate clinical decisions, as an example in drug repositioning [18]. It was within this gap that PoC technology emerged as a disruptive paradigm [19]. PoCs have been designed to perform analytical tests immediately at the site or patient care, whether in a doctor's office, an ambulance, or the patient's home [20]. By providing results within minutes ("sample-to-answer" time), they enable rapid diagnosis and timely intervention. Common

PoC devices available in clinical and home practice are aimed at detecting markers such as glucose [21], brain natriuretic peptide [22], glycated haemoglobin [23], coagulation [24], thyroid stimulating hormones [25], SARS-CoV-2 antibody [26], human chorionic gonadotropin [27] and others.

However, although PoC devices have significantly reduced the time-to-result window compared to classical lab analysis, they still present some limitations. Crucially, a PoC device provides only intermittent, snapshot measurement, which are useful for diagnosing acute conditions or detecting pathogens but are insufficient for managing chronic diseases. Effective management of chronic conditions requires continuous monitoring of health status to adjust therapies in real-time [28]. This critical need opens the possibility for a new generation of PoC systems, known as *wearable devices*, which aim to provide a continuous stream of physiological data.

1.2.1 Wearable devices: an overview

The term 'wearable devices' usually refers to a field of technology that includes devices capable of monitoring a variety of daily physiological and motor activities [29]. Nowadays, the wearable devices available on the market include smart watches, virtual reality glasses, skin patches, smart garments and others, within the aim of tracking critical physiological parameters or assessing athletic performance [30]. For example, it is possible to continuously measure heart beat rate via ECG, body temperature or blood pressure by easily wearing a common watch, also called 'smartwatch', that can communicate with a mobile phone and in some cases also to store the information into a cloud [31].

The development of all modern wearable technologies can be traced back to pioneering work such as that of Grossman in the 2004, who designed one of the first shirts capable of collecting and analysing data on breathing and heart rate, heralding the era of so-called "smart wearables" [32]. In this context, sensors play a pivotal role as the fundamental components driving the continuous advancement of wearable diagnostic technologies.

1.3 SENSORS IN HEALTHCARE

1.3.1 Introducing Sensors

The International Union of Pure and Applied Chemistry (IUPAC) defined a **sensor** as a device that responds to a specific physical or chemical property in its environment-or to

an applied stimulus- by generating a signal that can be read by an observer or an instrument [33].

In summary, a sensor is a device that qualitatively or quantitatively detects a change in its environment and converts this information into a reliable signal via a transducer [34,35]. Based on the transducer's operating principle, sensors can be categorised as follows:

- *Electrochemical*. These sensors detect a target species by converting a biochemical recognition event or a redox reaction into a measurable electrical signa (e.g. a change in current or potential) [36].
- *Optical*. These sensors utilise a change in optical properties (e.g., absorbance, fluorescence, luminescence) resulting from the interaction between the target analyte and a molecular probe [37].
- *Electrochemiluminescent/photoelectrochemical.* These sensors are based on a photoelectric interconversion process, where electrochemical energy is converted into luminous energy, or *vice versa* [38].
- *Piezoelectric.* These sensors generate an electrical signal in response to an applied mechanical stress, which is typically correlated with a change in mass on the sensor surface [39].
- *Thermal*. These sensors measure a change in heath (either absorbed or released) during a chemical reaction or a biochemical interaction [40].
- *Magnetic*. These sensors detect a variation in the magnetic properties of a system induced by the presence of the target analyte [41].

Among these sensor types, electrochemical sensors are particularly interesting for wearable applications due to their intrinsic features, such as low cost, high detection speed, and excellent compatibility with miniaturized technologies.

1.3.2 Electrochemical Sensor

The term *electrochemical sensor* is typically employed to denote a category of chemical sensors that are capable of detecting an analyte or chemical changes through the measurement of an electrical signal, thereby leveraging the utilisation of an electrode. The electrical signal -voltage or current- is related to changes in the analyte's concentration, making these sensors invaluable for numerous applications.

Electrochemical sensors can be categorised based on the types of electrical signal they measure [42]:

1. *Potentiometric sensors* measure the electromotive force (EMF) or potential difference between a reference electrode and a working electrode under conditions of negligible current flow. For a general reaction:

   $$Ox + ne^- \rightarrow Red$$

   the potential is described by the Nernst equation:

   $$E = E° + \frac{0.0592}{n} \log [Ox]$$

   where E is the electrode potential, $E°$ is the standard electrode potential, n is the number of electrons transferred per reactant species in the electrochemical reaction, and $[Ox]$ is the concentration of the oxidized species. This equation demonstrates a logarithmic dependence of the potential on the concentration of the target species, enabling quantitative detection.
2. *Amperometric sensors* quantify the concentration of an electroactive species by measuring the current generated from its oxidation or reduction at an electrode held at a fixed potential The relationship between the charge passed and the moles of the analyte converted is given by Faraday's law:

   $$N = \frac{Q}{nF}$$

   where N is the number of moles of substance transformed, Q is the total electric charge, F is Faraday's constant (~96.485 C/mol), and n is number of electrons transferred. Since current i is the derivative of charge with respect to time

   $$i = \frac{dQ}{dt}$$

   the reaction rate can be expressed as

   $$Rate(mol/s) = \frac{dN}{dt} = \frac{i}{nF}$$

   This establishes a direct link between the measured current and the analyte concentration, allowing for real-time quantification.
3. *Voltammetric sensors* analyse the current response while a variable potential is applied to the working electrode. The resulting current-potential plot, called a voltammogram, provides information about the electrochemical properties of the solution. Common techniques include cyclic voltammetry (CV), stripping

voltammetry (SV), square-wave voltammetry (SWV), linear sweep voltammetry (LSV), differential pulse voltammetry (DPV).

4. *Conductometric sensors* quantify the total ionic concentration in a solution by measuring its electrical conductivity. The conductivity k is related to the solution's resistance R, the electrode area A, and the distance between electrodes L by the equation .

$$k = L/A \cdot R$$

5. *Impedimetric sensors* apply a small amplitude alternating current (AC) voltage across a range of frequencies and measure the resulting impedance. The impedance, often represented as a complex number and plotted on a Nyquist plot, provides information about interfacial properties. A change in the charge transfer resistance (R_{ct}) often correlates with a change in the concentration of the analyte [43].
6. *Coulometric sensors* determine the concentration of the analyte by measuring the total charge (Q) required to completely convert it in an electrochemical reaction. The current (i) is measured over time (t), and the total charge is calculated by integrating the current:

$$Q = \int_0^t i\, dt$$

In light of the aforementioned considerations, it results evident that electrochemical sensors are particularly well-suited for the design and development of wearable devices. This is due to their unique set of features, which include miniaturization, digitalization and adaptability.

1.3.3 Electrochemical Sensors in Healthcare

As has been outlined in the foregoing sections, the scientific community has expressed interested in the development of PoC devices using electrochemical sensors, particularly with regard to their capacity for miniaturisation and digitalisation. Since 2006, when the ASSURED criteria for PoC devices were introduced, the WHO has been a notable proponent of the development of PoC in healthcare, applied to guide the development of diagnosis and treatment of sexually transmitted infections (STIs) in a single visit. **ASSURED** is an acronym standing for **A**ffordable, **S**ensitive, **S**pecific, **U**ser-friendly, **R**apid and robust, **E**quipment-free and **D**eliverable to end users [44]. In order to progress from a PoC device to a wearable device, two additional criteria have been added to

ASSURED: **Real-time** connectivity and **Easy** of sample collection resulting in REASSURED in the field of wearable development [45].

Indeed, a plethora of PoC devices employed in healthcare diagnosis, including pathogens infections [46], biomarkers monitoring [47], pharmacological treatment monitoring [48] are documented in the literature and available on the market.

Guided by the **REASSURED** paradigm, the following chapters detail a logical progression in sensor development, addressing specific challenges within this framework, presenting the design and development of tailored electrochemical sensors for the monitoring of different biomarkers, such as lithium, dopamine, and levodopa, thereby contributing to the advancement of personalised healthcare tools.

2. BIOCOMPATIBLE MATERIALS AND FABRICATION TECHNIQUES FOR WEARABLE SENSORS

2.1 Material Biocompatibility: A Primary Consideration in Wearable Sensor Development

In the context of designing and developing a PoC and wearable devices, it is imperative to evaluate multiple parameters, considering that the device must be worn in direct contact with the human body. Of particular significance among the numerous parameters is that of the biocompatibility in relation to the materials selected for the fabrication of such a device.

The term *biocompatible* generally refers to a material's ability to perform specific function without generating a host response [49]. According to the International Standards Organization (ISO), biocompatibility is defined as the ability of living body tissues to react to inert materials [50].

The critical importance of this requirement is underscored by the severe consequences of material failure. For instance, the use of certain polymerised functional monomers, common in dental resins, can induce allergic contact dermatitis and, in severe cases, life-threatening anaphylactic reactions [51]. Similarly, the corrosion of metallic alloys within the body can lead to the release of toxic ions (e.g. Ni^{2+}; Cr^{3+}, Hg^{2+}), causing local tissue damage or systemic toxicity [52]. Beyond these acute reactions, a material's inability to properly interface with biological tissues can trigger a chronic immune response. This results in persistent inflammation, foreign body reactions, and the formation of fibrotic capsules, which not only compromise patient health, but can also insulate the device and lead to catastrophic sensor failure [53]. Therefore, a deep understanding of host-material interactions is not merely a regulatory hurdle, but a fundamental prerequisite for the successful development of wearable diagnostic platform.

This chapter will provide an overview of the critical aspects of wearable sensor development, including the section of materials, fabrication techniques, and integration of these strategies to achieve successful device design.

2.2 MATERIALS FOR SUBSTRATES AND SUPPORTS

Electrochemical sensors are typically made of three basic components that include a substrate, an active element and an electrode.



Figure 2.2-1 example of an electrochemical sensor.

The choice of an appropriate substrate results crucial in the development of an electrochemical sensor for health application. Indeed, this material can influence several parameters such as sensitivity, limit of detection (LoD), stability, reproducibility and robustness of the sensor itself [54]. Typically, the materials used for the fabrication process has been long wild gold, platinum, silicon and carbon-based materials, such as glassy carbon electrodes. As it is possible to image, those materials are not fully suited for be worn several hours on patient's body, due to their rigidity [55]. Therefore, other materials are required to also guarantee the patients' comfort during wearability, through sensor's flexibility and stretchability, not affecting its biocompatibility.

2.2.1 PDMS

The prime material employed for flexible sensors and electronics fabrication is Poly(dimethyl siloxane) (PDMS) [56], due to its high flexibility and excellent biocompatibility. Indeed, this substrate is well-suited for a wide range of applications, including human-machine interfaces, personal healthcare monitoring, sport performance monitoring and so on [57]. To fully appreciate the versatility of PDMS, is formed from a base polymer of siloxane repeat units [$Si(CH_3)_2$-O-] terminated with vinyl groups, which is cross-linked via a hydrolysation reaction with a silicon-hydride (Si-H) functional cross linker, typically in the presence of a platinum catalyst. This reaction forms stable Si-C bonds between the polymer chains, creating a flexible, three-dimensional elastomeric network. The stoichiometric ratio between the vinyl-terminated base polymer and the Si-H cross-linked directly dictates the cross-linking density; a higher proportion of cross-

linker yields a stiffer, more brittle material, while a lower proportion results in a softer more elastic substrate [56] (**Figure 2.2-2**). However, despite its undoubted advantages, such as high permeability to oxygen and water vapours, PDMS has some inherent limitations. Due to its low surface energy, the adhesion of other materials onto PDMS surface is generally poor, leading to usage of chemical surface modifications or new surficial design [58].

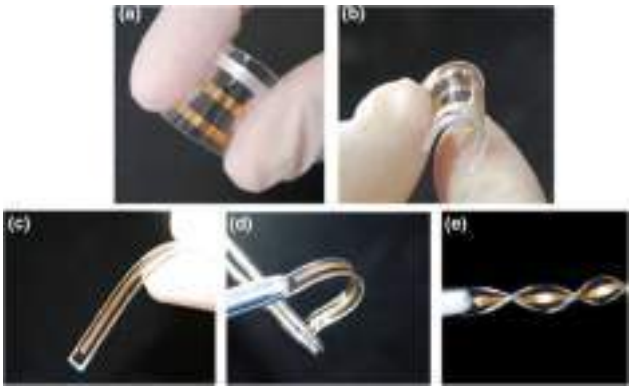

Figure 2.2-2. Pictures of FPT-Sensor. Working electrode: gold, reference electrode: silver and counter electrode: gold. Top view **(a)** and side view **(b)** of the three-electrode sensor, straight **(c),** bend **(d)** and twist **(e)** of the working electrode **[59]**.

Consequently, research is ongoing and continues to refine PDMS surface treatments whilst simultaneously propelling exploration into complementary polymer systems that have the capacity to either integrate with or substitute for it in particular wearable sensing applications.

2.2.2 Paper-based substrates

Paper represents an inexpensive, readily available, and flexible matrix whose inherent capillary action facilitates fluid flow, making it an attractive substrate for fabricating chromatographic devices, including PoC diagnostic [60]. Among the various PoC platforms available, some of the most prevalent paper-based systems are Lateral Flow Assays (LFAs), exemplified by SARS-CoV-2 antigen tests, pregnancy tests and others [46,61,62].

A significant advantage of using paper as a substrate lies in the versatility of its material properties. Indeed, the performance of the final device can be tailored for a specific analyte by selecting from different paper grades. These include standard filter papers, Whatman grade I chromatographic paper (noted for its high alpha-cellulose content),

office paper, cellulose acetate filter paper, and art paper [63]. Each of these papers offers distinct characteristics of wicking, sample retention, and compatibility with detection methods.

In order to prevent an excess of wettability on the surface, it is crucial to consider the use of paper as a substrate during the fabrication process. Wax printing is the method of choice for this purpose, despite the fact that it undergoes softening phenomena when in contact with the human skin at 34°-37 °C [64,65]. These softening phenomena can potentially impair the measurements and reduce the wearing comfort. Consequently, while wax printing remains a prevalent and accessible patterning method, its thermal instability necessitates careful consideration for epidermal applications, driving research into alternative patterning materials or composite substrates with higher thermal tolerance.

2.2.3 Polyimide (Kapton)

Polyimides, a class of high-performance polymers commercially known as Kapton®, are characterised by a repeating molecular backbone containing aromatic rings linked by imide functional groups (-CO-N-CO). This rigid, heterocyclic aromatic structure is responsible for their exceptional properties. The high resonance stability and strong intermolecular forces (e.g. π-π stacking) within this architecture confer outstanding thermal stability and mechanical strength. Simultaneously, the high stable covalent bonds and the lack of easily oxidizable aliphatic chains contribute to their excellent chemical and radiation resistance. These intrinsic properties, combined with low density and good dielectric characteristics, make polyimide an enabling material for advanced fabrication processes in flexible electronics, such as photolithography, where dimensional stability under thermal and chemical stress is paramount. [66].

These properties make polyimide an enabling platform for advanced fabrication techniques rather than a material for end-use consumer device. Its exceptional thermal stability is crucial for processes like photolithography, where it serves as a robust and flexible substrate for creating intricate, miniaturised electrode patterns. This capability is foundational for developing highly sophisticated flexible circuit that are integral to next-generation medical devices, even if the final product incorporates additional biocompatible layers [67–69]. Therefore, the primary role of polyimide in wearable and implantable sensor technology is often as a critical backbone material within a multi-layered stack. It provides the mechanical integrity and electronic foundation upon which

functional sensing elements are built, making it indispensable in research and prototyping for creating reliable, high-performance flexible electronics [66].

2.2.4 Other materials

Beyond PDMS, polyimide, and paper, the flexible electronics landscape leverages a diverse array of other polymers, each selected for specific properties. For example, Parylene-C , a semi-crystalline, linear thermoplastic polymer belonging to the poly(p-xylylene) family, is widely employed not as a substrate but as a conformal, biocompatible coating, providing a crucial barrier against moisture and biofluids for implantable devices [70–72].

Another important material is Ecoflex, a silicon elastomer that offers hyper-elasticity and lower Young's modulus than PDMS. This makes it the material of choice for applications demanding extreme stretchability and intimate integration with soft, dynamic tissues [73,74].

Furthermore, fibre-based sensors constitute a distinct class of wearable electronics where textiles, composed of natural fibres like cotton or linen, or synthetic polymers such as polyester, polyamide, or elastane, serve as the supporting layer. This approach enables the integration of electronic functionality directly into clothing, ensuring user comfort by avoiding direct, continuous skin contact and facilitating everyday use [75].

The meticulous selection of the aforementioned substrate materials, each offering a unique balance of flexibility, biocompatibility, and durability, provides the essential foundation upon which functional sensors are constructed. The subsequent pivotal stage is the implementation of specialised fabrication processes to transform these passive substrates into active, high-performance electrochemical sensing devices.

2.3 Fabrication Techniques For Wearable Electrochemical Sensors

The selection of an appropriate substrate material not only defines the fundamental characteristics of a wearable sensor but also dictates the compatible fabrication techniques for pattering conductive elements, as the material's thermal stability, chemical resistance, and surface energy constrain the viable manufacturing process.

In essence, this process acts as the catalyst that transforms an inert substrate into a functional, high-performance device, thereby enabling precise and reliable analytical

measurement. Moreover, the selected methodology exerts a direct influence on critical aspects such as feature resolution, manufacturing scalability, cost, and, ultimately, the sensor's electrochemical performance. In light of the aforementioned considerations, this section will provide an overview of the most frequently employed fabrication techniques, focusing on the advantages and disadvantages of each technique for wearable devices application. The techniques discussed represent distinct and complementary pathways for realizing next-generation wearable diagnostics.

2.3.1 Screen-printing

Screen-printing is a printing technique that has been extensively employed in the fabrication of electrochemical sensors [76–78]. The principle behind this technique entails the transfer of viscous ink through a patterned mesh screen onto a substrate, thereby transferring a specific conductive design (**Figure 2.3-1**.) This process, also referred to as a push-through process, uses a screen or stencil to define the electrode geometry [79,80].

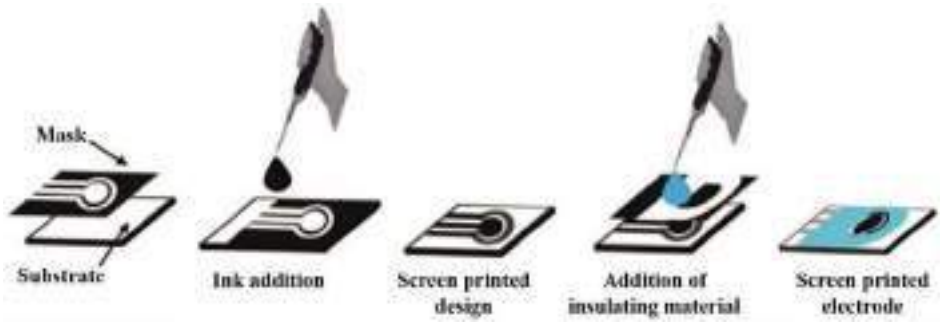

Figure 2.3-1. The construction process of SPEs **[81]**

It results clear that screen-printing offers several advantages, beginning with its compatibility with a wide range of substrates, including flexible and biocompatible polymers [82]. However, the successful translation of this technique hinges on a critical, non-trivial step: the formulation of functional inks. The core challenge lies in the fact that not all conductive materials can be directly used as inks. An effective ink must simultaneously satisfy a triad of often conflicting requirements, including optimal electrical conductivity for sensing, appropriate mechanical properties (e.g. adhesion, flexibility) to withstand deformation and bond to the substrate, and stable electrochemical performance in physiological environments [83]. Consequently, ongoing research is

intensely focused on developing advanced ink composition, tailoring conductive fillers, binders, and solvents, to meet stringent criteria for next-generation wearable electrodes [84].

The aforementioned inks are generally composed of conductive fillers (e.g. carbon, silver), binders (providing adhesion and cohesion), and solvents (to control viscosity) The specific formulation dictates the ink's rheology, which in turn confers the physical and chemical characteristics necessary for successful printing and stable performance on the target substrate [85].

Among all the ink components, the choice of solvent plays a critical role. Indeed, there is a predominant shift towards replacing organic solvents with water-based alternatives due to their cost-effectiveness, environmentally friendly nature, and non-toxic properties. [86]. However, using purely water-based solvents on hydrophobic surfaces (such as PDMS or plastic) remains a significant challenge. The poor interaction and adhesion at the ink-substrate interface can lead to layer delamination or the formation of pinholes, ultimately compromising the sensor's analytical performance [87].

One strategy available for the overcoming of the aforementioned issue, documented in the literature, is the use of co-solvents to decrease the interfacial surface tension between the substrate and the ink [86]. Nevertheless, these persistent challenges highlight why, particularly for applications demanding high biocompatibility and robust interfaces, alternative sensor fabrication technologies are also a critical area of investigation.

2.3.2 3D printing

3D-printing, also known as additive manufacturing, has emerged as a powerful tool for the rapid prototyping and fabrication of electrochemical sensors. Indeed, this techniques builds a three-dimensional object layer-by-layer from a digital model, which greatly facilitates the creation of costume-made shapes and architectures, as illustrated in **Figure 2.3-2** [88].

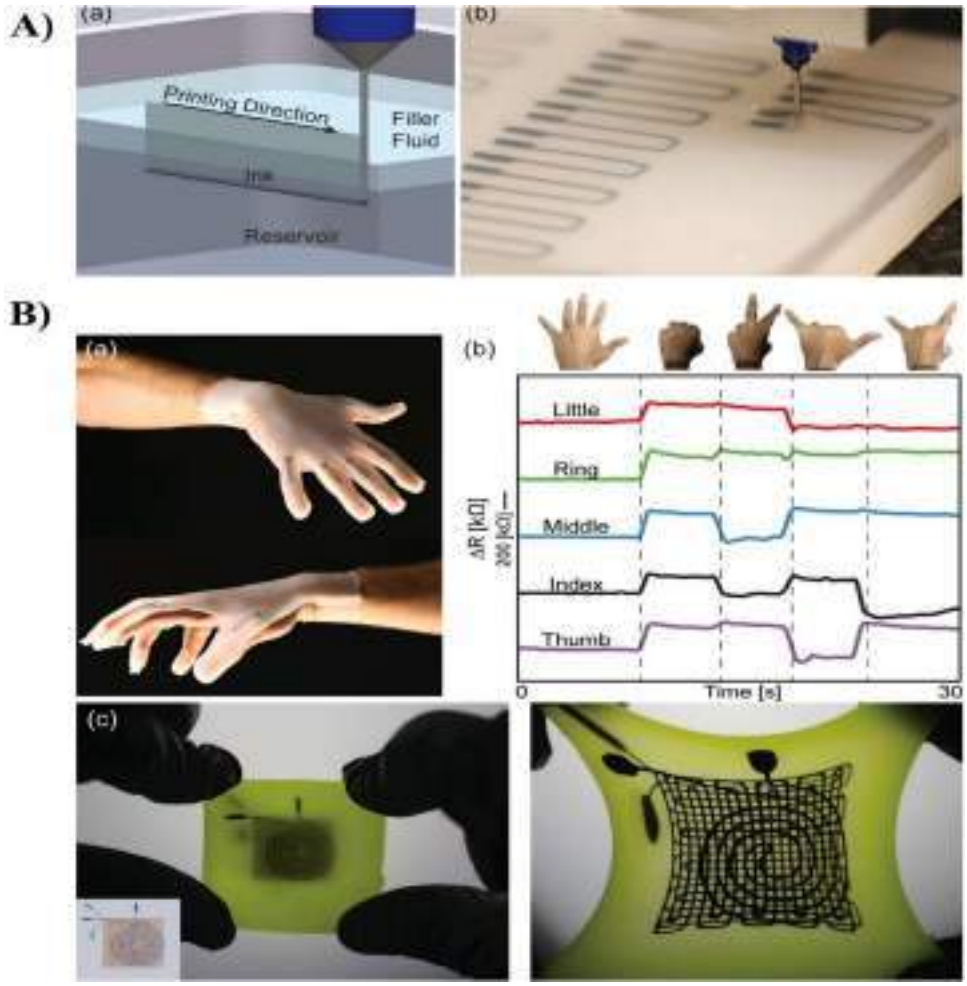

Figure 2.3-2. **(A)** Schematics and optical image of novel embedded 3D printing; and **(B) (a)** photograph of the glove printed using e-3DP**, (b)** change of electrical resistance with respect to the different postures, and **(c)** image of the three layers printed pressure and strain sensor in normal and stretched (left to right) **[89]**

A significant strength of 3D printing in the context of wearable sensors is its intrinsic versatility. The layer-by-layer deposition approach allows for the creation of complex, three-dimensional electrode geometries and fluidic components that are difficult or impossible to achieve with traditional methods [90].

Nevertheless, the accessibility of techniques like Fused Deposition Modeling (FDM) has contributed significantly to the popularity of this technology. Indeed, FDM enables the fabrication of electrochemical sensors using conductive thermoplastic filaments, such as polylactic acid (PLA) blended with cost-effective based-filaments carbon-based materials like graphene or carbon black [91].

Therefore, while the major advantage of this technique is the rapid production of numerous prototype tailored to specific user needs, a key challenge remains in

transitioning these bespoke designs to mass production, as scalability and production speed are currently limited if compared to established techniques such as screen-printing [92].

2.3.3 Laser-Induced Graphene

Laser-Induced Graphene (LIG) is a photothermal process in which a localised high-temperature environment transforms a carbon-rich precursor into porous graphene via laser irradiation [93]. Following the pioneering work of Tour et al., which demonstrated the formation of a 3D graphene foam by irradiating a polyimide film with CO_2 laser, the scientific community has widely adopted this technique for sensor fabrication due to its cost-effectiveness, single-step operation, and rapid production time [94].

A major advantage to LIG technology is its compatibility with a wide plethora of substrates. While PI remains the most common and well-characterized precursor [95]. In **Figure 2.3-3**, LIG has been successfully formed on diverse materials, including paper [96] and even unconventional sources such as coconut shells [97] and others carbonaceous materials [98,99]



Figure 2.3-3. Example of LIG-electrode fabricated on PI film using CO_2

Even though LIG electrodes represent a promising and versatile alternative to disposable screen-printed electrodes, challenges remain in achieving scalability and reproducibility. The standardisation of the manufacturing process and a deeper understanding of the process-structure-property relationship are critical areas requiring further fundamental investigation to fully harness the potential of this technique [100].

2.3.4 Other Fabrication Techniques

To complete the overview of electrochemical sensor fabrication, it is essential to mention other pivotal techniques beyond those previously detailed. For creating high-resolution electrodes, and microelectronics on flexible substrates, a plethora of methodologies exists, with photolithography and inkjet printing being two prominent examples.

Photolithography, for instance, is a fundamental lithographic technique that uses light (typically ultraviolet radiation) to transfer a geometric pattern from a photomask to a light-sensitive chemical (photoresist) on a substrate [101]. The fundamental steps of this process are summarised in **Figure 2.3-4**

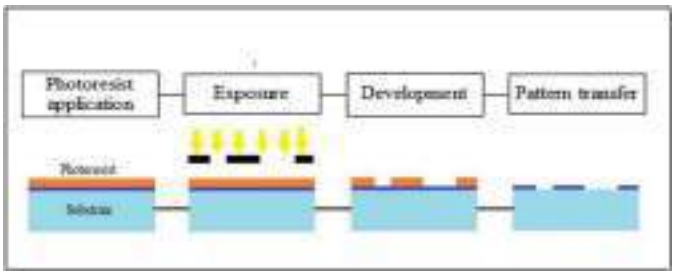

Figure 2.3-4. Basic steps in photolithography **[102]**

The standard procedure used in photolithography, involves a substrate with a photoresist, followed by UV exposure through a photomask. The exposed (or unexposed, depending on the resist type) areas are then dissolved in a developer solution. This pattern resist layer subsequently serves as a stencil for precise pattern transfer via etching of the underlying material or via lift-off process to define metallic structures. [103–105]. The principal advantage of photolithography is its unparalleled feature resolution and reproducibility, making it the cornerstone of microelectronics. However, for wearable applications, its drawbacks include high cost, multi-step complexity, and the use of harsh chemicals, which can be incompatible with some flexible polymeric substrates.

On the other hand, inkjet printing, another widely used technique for soft electronics, is an additive, non-contact method that deposit precise droplet of functional inks directly onto a substrate [106]. This constitutes a digital and maskless process compared with screen-printing, allowing a rapid design changes and the efficient use of often expensive materials, such as conductive nanoparticles, biomolecules, etc.[107].

In conclusion, while techniques like screen-printing and 3D-printing offer greater accessibility and design flexibility for many wearables applications, photolithography and inkjet printing fulfil critical niche roles. Photolithography provides the benchmark for miniaturisation and precision [108] whereas inkjet printing enables high-resolution, digital fabrication of custom circuits with minimal waste [109]. Their existence underscores the diverse toolkit available to sensor designer, where the selection is dictated by a trade-off between resolution, cost, scalability, and material compatibility.

2.4 MODIFICATION OF THE SENSING AREA

The core of an electrochemical sensor is the sensing area of its electrodes. Indeed, this region constates the active element where all Faradic reactions and biochemical recognition events occur, enabling the selective and specific detection of the target analyte [110,111] However, the strategic modification of this sensing area serves not only to confer specificity but also to enhance electron transfer kinetics and mitigate surface fouling [111]. In order to achieve this purpose, several strategies have been proposed in the literature, compelling the deposition of metal-based nanoparticles, the usage of conductive polymers, some carbon-based materials and at last synthetic materials. This section will provide an overview of these modification strategies, namely the deposition of metal-based nanoparticles, the use of conductive polymers, carbon-based materials, and synthetic materials, exploring how each contributes to the creation of more sensitive, selective, and stable electrochemical sensing interfaces.

2.4.1 Metal Nanoparticles

Metals are widely used in electrochemistry for the construction and modification of sensing areas due to their high electrical conductivity, ductility, and, in some cases, excellent biocompatibility. Among them, gold (Au) or titanium (Ti) are particularly suited for implantable or wearable devices because they can remain in prolonged contact with the body without significant degradation or oxidation [50]

A significant advancement lies in the miniaturization of these metals to the nanoscale (10-100 nm), creating **Metal Nanoparticles (MNPs)**. These nano-dimension offers an ideal toolkit for electrochemical sensor development, significantly enhancing biocompatibility, catalytic activity, and overall device performance (https://pubs.acs.org/sharingguidelines).

Gold nanoparticles (AuNPs) hold a special place among MNPs due to their unique physical and chemical properties. Indeed, they exhibit Local Surface Plasmon Resonance (LSPR), a phenomenon involving the interaction between an oscillating electric field and incident light- [112]. Furthermore, AuNPs possess excellent stability and enhance electron transfer kinetics through direct or mediate mechanism, thereby improving the conductivity of the sensing platform [113].

Another important class of MNPs used for the construction of a sensing platform are silver nanoparticles (AgNPs). AgNPs represent another important case, valued for their

cost-effectiveness and stability. In nanobiotechnology, they are widely utilised for their potent inhibitory effects against microbial pathogens, including bacteria and fungi [114]. While classical colloidal synthesis is a common method for producing MNPs like AuNPs and AgNPs [115,116] a major challenge is achieving precise size control. This is critical to ensure batch-to-batch reproducibility and surface stability. To address this, electrochemical deposition is often the preferred method for sensor application.

For instance, AuNPs can be electrodeposited from an aqueous solution of $HAuCl_4$ by reducing Au(III) to Au(0). This is achieved either by applying a constant negative potential for a fixed duration [117] or by cycling the potential a set number of time at an optimal scan rate [118], leading to the direct formation of clustered AuNPs on the electrode surface. The same principle applied to AgNPs electrodeposition, where Ag(I) from an aqueous solution is reduced to Ag(0) directly onto the surface using electrochemical methods [119].

In summary, the ability to precisely electrodeposit MNPs like Au and Ag enables the tailored engineering of the electrode surface, directly enhancing conductivity, catalytic activity, and stability. This establishes metal nanoparticles as a cornerstone material for defining the final performance of wearable electrochemical sensors.

2.4.2 Conductive Polymers

Conventionally, organic polymers have been considered electrical insulators. with most application relying on these insulating properties [120]. However, after the 1977 discovery that iodine-doped polyacetylene exhibits high electronic conductivity, new approaches for modifying sensing surfaces emerged [121].

This particular class of organic polymers, known as conductive polymers, shows certain features such as electrical conductivity, high electron affinity, as intrinsic redox activity [122]. A key physical-chemical peculiarity is their π-electron backbone, which allows for the control of electrical conductivity through an extended π-conjugated system, enabling efficient long-range electron transfer [123,124].

However, one of the most advantageous characteristics is the possibility of functionalising either the polymer or its monomer with distinctive groups to tailor their properties, for instance, to facilitate the immobilisation of bioreceptors [125].

Conductive polymer can be readily prepared via chemical or electrochemical oxidation of their corresponding monomers in various organic or aqueous solvents [120]. As it possible to foresee, electrochemical polymerisation results particularly advantageous as

it allows for the direct deposition of uniform films with well-controlled thickness onto the sensing surface [126].

A review of the literature reveals that polyaniline (PANI) [127], polypyrrole (Ppy) [128], poly(3,4-ethylenedioxythiophene) (PEDOT) [129], polyacetylene (PAc) [130], and polythiophene (PTh) [131] are among the most widely used electrochemically prepared conductive polymers. As demonstrated in **Figure 2.4-1**, the structures of the widely used ones were examined.[132]

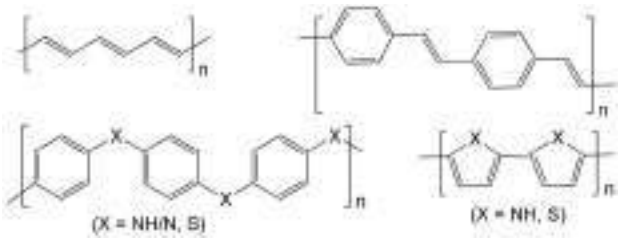

Figure 2.4-1 Chemical structures of some conductive polymers. From top left clockwise: polyacetylene; polyphenylene vinylene; polypyrrole (X = NH) and polythiophene (X = S); and polyaniline (X = NH) and polyphenylene sulphide (X = S).

A significant drawback, however, is that some of these chemicals, in both their monomeric and polymeric forms, can exhibit toxicity and teratogenicity upon direct contact with living organism [133]. This raises concerns regarding their full biocompatibility, which is a critical requirement for wearable platforms.

Consequently, a new class of biocompatible electroactive polymers is emerging, based on the polymerization of amino acids (AA). These AA-based platforms are particularly suited for wearable electrochemical sensors due to their non-toxicity, biocompatibility, biodegradability, water dispersibility, electrochemical stability, and a wide variety of functional side groups (e.g. -COOH, $-NH_2$, or -SH) available for further functionalisation [134,135]. However, the successful integration of these materials into reliable sensing platforms requires a deep understanding of their electropolymerization mechanism and the correlation between their structure and electrochemical performance, a key challenge that will be addressed in the subsequent chapters of this work.

2.4.3 Molecularly Imprinted Polymers (MIPs): Biomimetic Receptors for Selective Sensing

While the above discussed modifications enhance electron transfer and biocompatibility of the sensing area, achieving high specificity towards a target analyte remains a

paramount challenge in complex biological environments. To address this, researchers have developed synthetic receptors capable of molecular recognition, mimicking the natural lock-and-key mechanism of antibodies and enzymes [136].

Among these, Molecularly Imprinted Polymers (MIPs) have emerged as a powerful and versatile strategy. MIPs possess tailored recognition sites that are complementary in shape, size, and functional groups to a specific target molecule, known as the template [137].

The synthetic process for a MIP typically requires four key components: a *template* molecule, a *functional monomer*, a *cross-liker*, and a *polymerization initiator*, each playing a specific role [138]. The cross-linker, for instance, must interact with both the functional monomer and the template to facilitate the formation of a rigid three-dimensional polymer network [139].

MIP synthesis can be performed via two primary strategies: *covalent* and *non-covalent* (*self-assembly*). In the covalent approach, the template is covalently bonded to the functional monomer prior to polymerization. A significant disadvantage of this method is that it can lock the template in a non-native conformation, which may impair the final recognition efficiency [140]. Conversely, the more prevalent non-covalent strategy relies on weaker interactions, such as hydrogen bonding, Van der Waals forces, and ionic or hydrophobic interactions, between the monomer and the template [141]. Indeed, non-covalent MIP synthesis is compatible with various techniques, including electrochemical polymerization [142] and solid-phase synthesis [143]. In solid-phase synthesis, the template is immobilized on a solid support (e.g. glass beads) prior to performing the polymerisation step. After polymerisation, a series of washes are performed: cold solvent removes low-affinity polymers and residual monomers, while a subsequent hot solvent wash releases the high-affinity MIPs from the template [144]. This process typically yields spherical MIP nanoparticles dispersible in aqueous solutions [145].

A major advantage of the non-covalent approach is its compatibility

One of the major advantages of using non-covalent approaches in MIP synthesis is the possibility of using molecular modelling [146]. Computational methods, such as molecular dynamics, can predict monomer-template binding energies, enabling the virtual screening of functional monomers and linkers to significantly increase the electivity of the resulting MIPs [147,148].

Thus, MIPs represent a pivotal integration of material science and molecular design, offering a robust and customizable path to achieving the high specificity required for next-generation wearable sensors in complex biological milieus.

2.5 CONCLUSIONS

The development of wearable electrochemical sensors is fundamentally an exercise in strategic compromise, where material selection, fabrication methodology, and surface engineering must be harmonised to meet a stringent set of requirements defined by the REASSURED criteria. As delineated in this chapter, biocompatibility is not a peripheral concern but a primary design constraint, as the intimate and prolonged contact with the skin dictates the use of non-toxic, flexible, and often stretchable substrates such as PDMS, polyimide, or advanced textiles. However, the choice of substrate inherently influences and restricts the subsequent fabrication pathways. Techniques like screen-printing and 3D printing offer versatility and accessibility for prototyping on flexible polymers, while laser-induced graphene and photolithography provide pathways to high-resolution, miniaturised features, albeit with differing trade-offs in cost, scalability, and material compatibility.

Crucially, the inert substrate and the fabricated conductive pattern merely form the foundational skeleton of a functional sensor. The analytical soul of the device resides in the active sensing interface. Therefore, the deliberate modification of the electrode surface, through the deposition of catalytic nanomaterials, the electropolymerization of conductive or biocompatible polymers, or the integration of synthetic receptors like MIPs, is the critical step that transforms a simple transducer into a sensitive, selective, and stable analytical tool. This multi-layered design philosophy, which progresses from biocompatible substrate to tailored fabrication and finally to functional interface modification, establishes the essential toolkit for creating a viable wearable diagnostic platform.

3. DEVELOPMENT OF A PoC SENSOR FOR LITHIUM MONITORING IN BIPOLAR DISORDER

3.1 Mental Disorders and The Imperative For Personalized Pharmacotherapy

Mental disorders represent a profound and growing global health challenge, characterised as chronic conditions that significantly disrupt an individual's cognition, emotional regulation, and behaviour. Thid disruption leads to a substantial compromise in quality of life and daily functioning, placing a heavy burden on healthcare system and societies worldwide [149]. This broad category encompasses a spectrum of distinct illnesses, including schizophrenia, bipolar disorders (or manic-depressive illness), major depressive disorder, and panic disorder.

In response to this extensive burden, the WHO has explicitly called for a strengthened global response in its Comprehensive Mental Health Action Plan 2013-2030, underscoring the critical need to improve healthcare infrastructures and ensure access to efficient, cost-effective treatments [150].

However, a fundamental obstacle to optimising care for these conditions lies in their very classification. Indeed, current diagnostic frameworks often rely on phenomenological observations rather than objective aetiological or pathophysiological data, making precise diagnosis and treatment personalisation inherently difficult [151].

Given this diagnostic complexity, pharmacotherapy remains a cornerstone of symptoms management. Reflecting this therapeutic reliance, the WHO has classified several psychotropic medications, including lithium carbonate, valproic acid, haloperidol, and fluoxetine, as essential medicines for stabilising patients [152].

This therapeutic reliance, in turn, introduces another significant clinical challenge: the narrow therapeutic window of many psychotropic drugs. Indeed, this precarious balance makes continuous therapeutic drug monitoring not merely beneficial but imperative for long-term patient management. Moreover, the ultimate goal is to maintain a precise drug concentration that ensures therapeutic efficacy while preventing severe, and often life-threatening, iatrogenic poisoning from overdose.

3.2 The Role of Lithium in Bipolar Disorder Management

Among mental disorders, bipolar disorder exemplifies the challenges and necessities of precise pharmacotherapy. It is a chronic condition characterised by alternating manic and major depressive episodes, with a tragically high incidence of mortality by suicide compared to other psychiatric illnesses [153,154], This stark reality intensifies the interest in developing effective early interventions and treatments with specific anti-suicidal medication, among which lithium stands out for its well-documented efficacy [155]. Consequently, Lithium has been consistently included into the WHO Model List of Essential Medicine as one of the most effective and safe treatments for bipolar disorders [150,156]

However, the clinical use of lithium is a paradigm of a critical trade-off between unparalleled efficacy and severe safety risk. Its therapeutic effect is confined to a remarkably narrow range of 0.5 to 0.8 mM in blood serum. This range is dangerously close to the concentration that induce severe intoxication (>1.5 mM), which can lead to significant side effects and, in drastic cases involving levels of 2.0-2.5 mM, death [157,158]. Therefore, continuous monitoring of lithium levels during long-term treatment is not just useful but crucial to prevent dose-related adverse effects and ensure patient safety.

While blood tests remain the gold standard for monitoring lithium and investigating associated physiological changes [159], their invasive nature presents a significant burden, discouraging the frequent sampling required for optimal management. This limitation has driven the exploration of alternative biofluids, such as saliva and sweat, whose ease of sampling, practical availability, and non-invasive collection offer a compelling advantage for developing patient-friendly monitoring tools. Research into the correlation between blood and these peripheral biofluids is particularly promising. For instance, studies have demonstrated that lithium concentrations in saliva and sweat can be 2-3 times higher than in serum, establishing a viable quantitative relationship [158]. These findings pave the way for the development of novel analytical platforms capable of monitoring lithium levels in a continuous or frequent manner, directly addressing the critical need for a PoC testing paradigm that aligns with the principles of personalized and accessible medicine [160,161].

3.3 Lithium Detection In Peripheral Biofluids Using a Smart Electrochemical Sensor

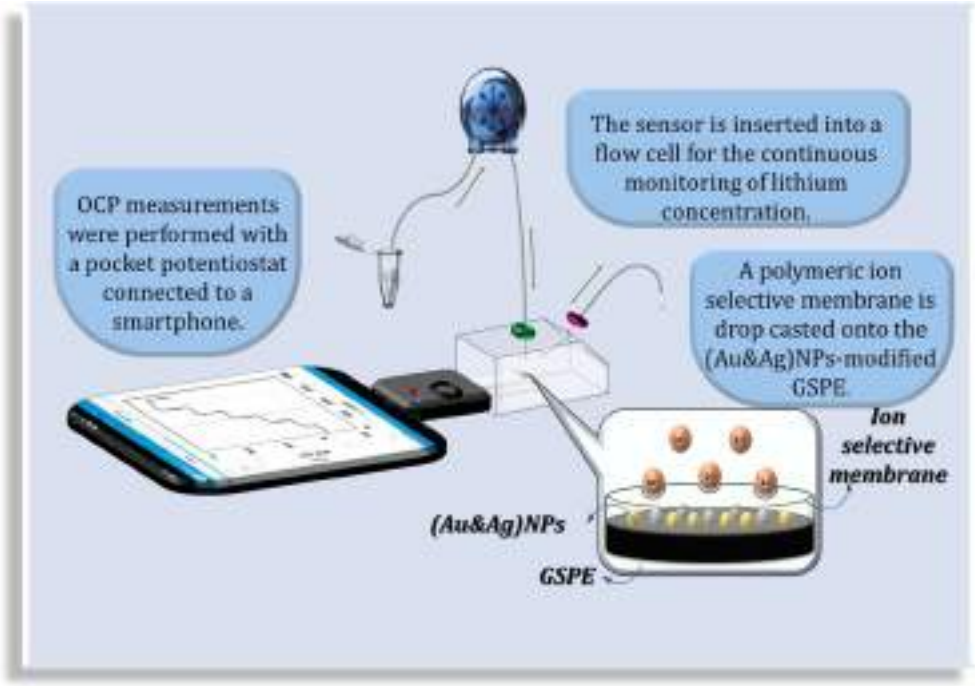

Figure 3.3-1 Graphical abstract. Potentiometric sensing infrastructure for continuous lirhium monitoring. The platform integrates a micro-flow cell setpu with a high-stability solid-contact sensor, fabricated by drop-casting a lithium-selective membrane onto a bimetallic (Au&Ag)NPs-modified GSPE The real-time Open Circuit Potential (OCP) response is transmitted to a smartphone interface, enabling decentralized therapeutic drug monitoring through a portable pocket-size potentiostat.

3.3.1 State of Art

The management of bipolar disorder via lithium therapy is critically constrained by the imperative of frequent monitoring of its narrow therapeutic window. To address this challenge, this section presents the development of a smart, low-cost PoC potentiometric sensor for the rapid detection of lithium ions (Li^+) in peripheral biofluids. The sensing platform was fabricated on graphite screen-printed electrodes (SPEs), which were functionally enhanced through a two-step modification process. First, a bimetallic nanostructured layer was created via the electrodeposition of silver and gold nanoparticles [(Au&Ag)NPs], providing a high surface-area and conductive substrate. Subsequently, a lithium-selective membrane was drop-cast onto this nanostructured surface, to ensure high ion selectivity. The optimised electrochemical platform was thoroughly characterised, and its analytical performance was validated in buffer solutions, as well as in clinically relevant matrices of artificial sweat and saliva. Calibration curves, obtained using a compact, smartphone-connected potentiostat, demonstrated a wide dynamic range

from 10^{-5} M to 10^{-1} M [Li^+] and a low limit of detection (LOD) of 1.6 10^{-6} M. These performance metrics, achieved in complex media, confirm the platform's significant potential for the translation into a practical clinical tool for the decentralised therapeutic drug monitoring of lithium.

3.3.2 Chemicals

Tetrachloroauric acid ($HAuCl_4$), silver nitrate ($AgNO_3$), sulfuric acid 95-97% (H_2SO_4), sodium nitrate ($NaNO_3$), potassium ferrocyanide $K_4[Fe(CN)_6]$, potassium ferricyanide $K_3[Fe(CN)_6]$, potassium chloride (KCl), 6,6-dibenzyl-1,4,8–11-tetraoxacyclotetradecane (lithium ionophore VI), potassium tetrakis (4-chlorophenyl) borate (K-TCPB), 2-nitrophenyl octyl ether (NPOE), polyvinyl chloride (PVC) high molecular weight, tetrahydrofuran (THF), lithium chloride (LiCl), magnesium chloride ($MgCl_2$), ammonium chloride (NH_4Cl), sodium chloride (NaCl), sodium sulphate (Na_2SO_4), sodium bicarbonate ($NaHCO_3$), disodium hydrogen phosphate (Na_2HPO_4), sodium dihydrogen phosphate (NaH_2PO_4), potassium dihydrogen phosphate, (KH_2PO_4), potassium thiocyanate (KSCN), calcium chloride ($CaCl_2$) and urea ($CO(NH_2)_2$) were purchased from Merck (Darmstadt, Germany). All the solutions have been prepared using MilliQ water (MilliQ-Water Purification system, Millipore, UK)

3.3.3 Apparatus

Screen-printed electrochemical cells (SPCs) based on a graphite-working electrode, a graphite-counter electrode, and a silver pseudo-reference electrode (EcoBioServices srl, Sesto Fiorentino, Italy) were used for the electrochemical experiments. The open circuit potential (OCP) measurements were carried out at room temperature using Sensit Smart portable potentiostat/galvanostat (PalmSens BV, Houten, The Netherlands) connected to an Android© smartphone equipped with PSTouch software for data acquisition and elaboration. Potentiometric measurements were also performed with a commercial lithium ion-selective electrode (DX207-Li ISE half-cell electrode, ref. 51107673) and an Ag/AgCl reference electrode (pH electrode InLab reference, ref. 51343190) purchased from Mettler-Toledo S.p.A. (Milan, Italy). The peristaltic pump needed for flow measurements was purchased from Gilson Inc., USA. Dropsens wall-jet microflow cell (ref. DRP-FLWCL) was purchased from Metrohm (Milan, Italy). Scanning electron microscopy (SEM) analysis was carried out using a Gaia 3 microscope (Tescan a.s., Brno, Czech Republic). SEM images were acquired using an acceleration voltage of 5 kV for

the bare-graphite electrodes and 20 kV for the nanostructured electrodes. Energy dispersive X-ray analysis (EDX) was performed to assess the elemental composition of the modified electrode surface.

3.3.4 Preparation of (Au&Ag)NPs-modified Graphite Screen-Printed Electrodes

The surface of the graphite screen-printed electrode (GSPE) was modified with silver and gold bimetallic nanoparticles ((Au&Ag)NPs) using cyclic voltammetry (CV) to produce an enhancement of the electrochemical behaviour of the GSPE. Firstly, 2.5 mM of $AgNO_3$ in a 0.1 M $NaNO_3$ solution was dropped onto the GSPE surface. The potential was cycled from −1.0 V to +0.5 V vs. Ag/AgCl pseudo-reference electrode for 10 times at a 50 mV/s scan rate. Successively, the AgNPs-modified GSPE was washed for three times with deionized water to remove the excess of free ions from the surface. A solution of 2.5 mM $HAuCl_4$ in 0.5 M H_2SO_4 was dropped onto the AgNPs-modified graphite electrode. The potential was cycled from −0.2 V to +1.6 V vs. Ag/AgCl pseudo-reference electrode for 10 times at a 100 mV/s scan rate. The (Au&Ag)NPs/GSPE was then washed with deionized water for three times.

3.3.5 Study of the Electrochemical Performance of (Au&Ag)NPs-Modified Screen-Printed Electrodes

In order to quantitatively evaluate the enhancement provided by the nanostructuration, the electrochemical performance of the (Au&Ag)NPs/GSPE was characterised using CV. The measurements were performed using a 5 mM equimolar solution of $[Fe(CN)_6]^{3-/4-}$ in 0.1 M KCl as a redox-probe. CV scans were recorded with a potential window of -0.5 V to 1.0 V at varying scan rates (25-150 mV/s). The relationship between the peak current and the square root of the scan rate was found to be linear, confirming a diffusion-controlled process. The electroactive surface area was then precisely calculated from the slope of this linear regression using the Randles-Sevcik equation [162]:

$$i_p = 0.446nFAC^0\left(\frac{nFvD_o}{RT}\right)^{1/2}$$

where i_p is the peak current, n i is the number of electrons transferred, F is the Faraday constant (C/mol), A (cm^2) is the electrode surface area, R is the gas constant (8.314 J/(mol·K)), D_o (cm^2/s) is the diffusion coefficient of the oxidized analyte, and C^0 (mol/cm^3) is the analyte bulk concentration. This calculation confirmed significant increase in the electroactive area compared to an unmodified GSPE.

Complementing the electrochemical data, SEM was employed to directly visualize the morphological changes induced by the modification process. The SEM analysis provided clear evidence of the successful formation of a nanostructured surface on the GSPE, revealing the homogeneous distribution of the bimetallic nanoparticles and contrasting sharply with the smooth morphology of the pristine graphite electrode.

3.3.6 Preparation of Lithium Sensor

With the optimised nanostructured transducer in place, the selective element for lithium detection was incorporated. A lithium-selective membrane cocktail was prepared by combining 28% (*w*/*w*) PVC as the matrix, 1% (*w*/*w*) lithium ionophore VI for selectivity, 0.2% (*w*/*w*) K-TCPB as an ion additive, and 70.8% (*w*/*w*) NPOE as a plasticiser. The 100 mg of mixture were dissolved in 1 mL of THF and stirred thoroughly for one hour to ensure homogeneity. A 5 µL aliquot of this solution was drop-cast onto the (Au&Ag)NPs/GSPE surface. The fabricated sensor was left to dry overnight in dark conditions, allowing for the controlled evaporation of the THF solvent and the formation of a stable, functional membrane.

3.3.7 Lithium Detection

The potentiometric response of the finalised sensor was evaluated using OCP measurements. A smart setup was employed, comprising a portable Sensit Smart potentiostat connected to a smartphone for data acquisition and analysis. The sensor was tested in drop configuration (50 µL) with standard Li^+ solutions ranging from 10^{-5} M to 10^{-1} M, using a 0.05 M $MgCl_2$ as the supporting electrolyte solution.

The response time, defined as the time required to reach the 90% of the maximum equilibrium potential [163], was determined for each concentration.

A calibration curve was then constructed by plotting the stable potential value against the logarithm of the Li^+ concentration. The limit of detection (LOD) was rigorously determined according to the method established by Bakker and Pretsch [164]. This approach identifies the LOD as the intersection point of the two linear segments of the potentiometric response function: the Nernstian slope at higher concentrations and the constant baseline potential at lower concentrations, which is governed by the background electrolyte.

The sensor demonstrated excellent operational stability. When stored in dry, dark conditions between measurements, it retained its performances for at least ten

independent calibration cycles, exhibiting good reproducibility with a relative standard deviation (RSD) of less than 10% for the calibration parameters.

3.3.8 Selectivity Assessment via the Fixed Interference Method (FIM)

The practical utility of an ion-selective electrode is critically dependent on its ability to distinguish the target ion in the presence of other, potentially interfering, species. To rigorously evaluate this characteristic, the selectivity of the developed lithium-selective membrane has been quantified using the Fixed Interference Method (FIM). This method involved performing OCP measurements in solutions containing a constant, clinically relevant activity of a potential interfering ion (K^+, Na^+, NH_4^+, Ca^{+2}), while varying the activity of the primary Li^+ ion [165].

The resulting potential values were plotted against the logarithm of the Li^+ activity. The selectivity coefficient, $K^{pot}_{A,B}$, was then determined from the intersection point of the extrapolated linear segments of this plot, using the following established equation:

$$K_{A,B}^{pot} = \frac{a_A}{a_B^{\frac{z_A}{z_B}}}$$

where a_A is the activity of Li^+ at the intersection point, a_B is the fixed activity of the interfering ion, and Z_A and Z_B are the charges of the respective ions. The obtained selectivity coefficients confirmed that the sensor, empowered by the lithium ionophore VI, exhibits a strong presence for Li^+ over the most common cations found in sweat and saliva, a fundamental requirement for accurate analysis in complex biofluids.

3.3.9 Validation in Synthetic Biofluids as Proof-of-Concept

Following the foundational characterisation in buffer solutions, the analytical performance of the sensor was validated in a more realistic complex environment. As a definitive proof-of-concept towards its application for non-invasive monitoring, the sensor was used to quantify lithium in synthetic human sweat and saliva. These matrices were prepared according to the well-established literature protocols [166,167], to mimic the intricate ion composition of their real-world counterparts.

The synthetic sweat was composed of a mixture of KCl (6 mM), NH_4Cl (5 mM), $MgCl_2$ (0.08 mM), $NaHCO_3$ (2.6 mM), Na_2HPO_4 (0.04 mM), adjusted to pH 5.3. The synthetic saliva contained a more complex blend, including NaCl (2.2 mM), KCl (12.9 mM),

KSCN (1.9 mM), KH_2PO_4 (4.8 mM), urea (3.3 mM), Na_2SO_4 (2.4 mM), NH_4Cl (3.3 mM), $CaCl_2$ (1.5 mM), and $NaHCO_3$ (7.5 mM) at pH 6.8.

OCP measurements were conducted under identical conditions to those used for the standard calibration. The sensor demonstrated a stable and reproducible Nernstian response in both synthetic sweat and saliva.

3.3.10 Results and Discussion

3.3.10.1 (Au&Ag)NPs Electrodeposition and Surface Characterization

The electrochemical performance of the graphite screen-printed electrodes (GSPEs) was enhanced through a sequential electrodeposition of silver and gold nanoparticles ((Au&Ag)NPs) via cyclic voltammetry **Figure 3.3-2** shows the typical cyclic voltammograms recorded during this process. The evolution of the Voltammetric profiles over multiple cycles confirming the progressive nucleation and growth of AgNPs from 2.5 mM $AgNO_3$ solution (**Figure 3.3-2a)** and AuNPs from a 2.5 mM $HAuCl_4$ solution (**Figure 3.3-2b**).

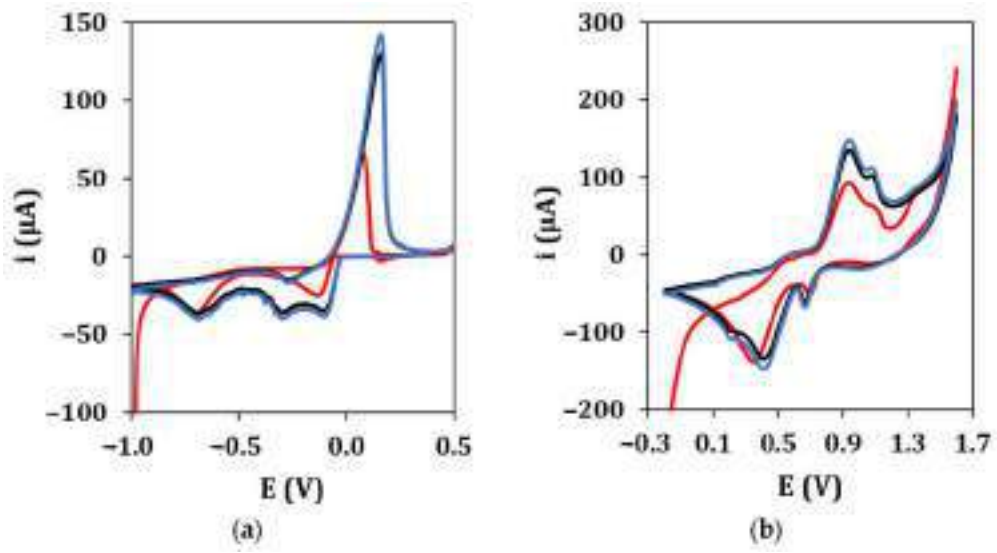

Figure 3.3-2. (a) AgNPs electrodeposition from a 2.5 mM $AgNO_3$ solution in 0.1 M $NaNO_3$ (•: 1st cycle, •: 10th cycle, •: 20th cycle). Experimental conditions: potential range from −1.0 V to +0.5 V, 50 mV/s scan rate. **b)** AuNPs electrodeposition from a 2.5 mM $HAuCl_4$ solution in 0.5 M H_2SO_4 (•: 1st cycle, •: 10th cycle, •: 20th cycle). Experimental conditions: potential range from −0.2 V to +1.6 V, 100 mV/s scan rate. Reprinted with the permission of **[168]**

The impact of this nanostructuration on the electrode's properties was then quantified. Cyclic voltammetry (CV) was performed using a 5 mM equimolar solution of $([Fe(CN)_6]^{-4/-3}$ in 0.1 M KCl as a redox probe. The electroactive surface area was calculated for both bare and modified electrodes by applying the Randles–Sevcik to the data obtained from the plotting the anodic (i_{pa}) and cathodic (i_{pc}) peak currents against the square root of the scan rate (**Figure 3.3-3**).

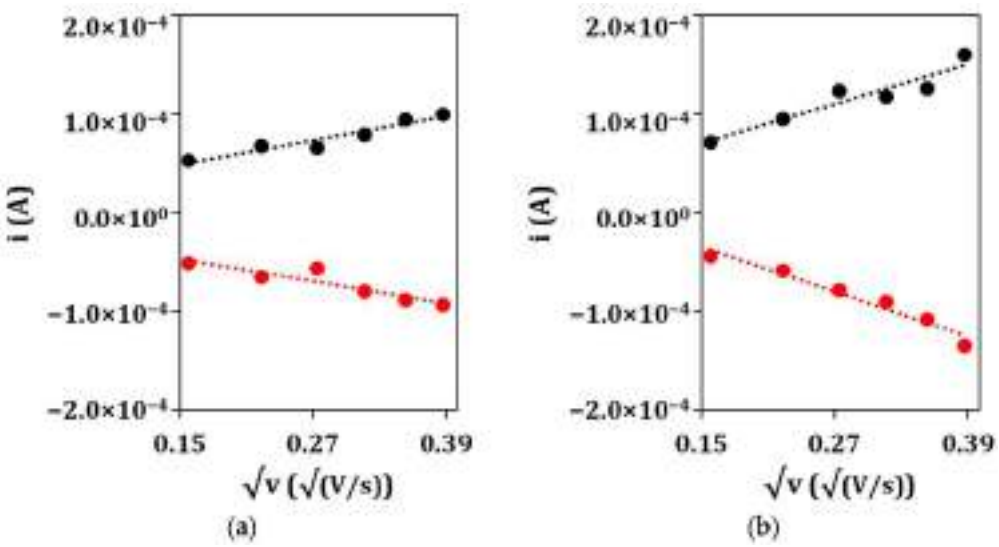

Figure 3.3-3 Plots of anodic (•) and cathodic (•) peak currents vs. the square root of the scan rate for **(a)** bare GSPE and **(b)** (Au&Ag)NPs/GSPE. Reprinted with the permission of **[169].**

The calculated electroactive area values, summarised in

Table 3.3.10-I**,** demonstrate a significant enhancement.

Table 3.3.10-I. Electroactive-area values of unmodified GSPEs and (Au&Ag)NPs/GSPEs.

	A_{anodic} (mm^2)	$A_{cathodic}$ (mm^2)	$\bar{A}$ (mm^2)
GSPE	5.5	5.1	5.3 ± 0.3
(Au&Ag)NPs/GSPE	9.0	10.3	9.6 ± 0.9

The nanostructured (Au&Ag)NPs/GSPE platform exhibited an average electroactive area of 9.6 ± 0.9 mm^2, which is approximately 1.8 times larger than that of the bare GSPE (5.3 ± 0.3 mm^2). This increase is attributed to the deposition of conductive noble metals onto the graphite surface, which boost both conductivity and the available surface area for electron transfer. Notably, the electroactive area of the modified electrode also surpasses

its geometric area (7.1 mm^2), confirming the successful creation of a nanostructured, high-surface-area material.

The observed increase in the electroactive area (from 5.3 to 9.6 mm^2) is not merely a geometric effect but reflects the synergistic contribution of Au and Ag nanoparticles. While AgNPs provide high conductivity, the subsequent deposition of AuNPs creates a hierarchical nanostructure that prevents the passivation of the graphite surface and increases the density of available sites for the redox probe $[Fe(CN)_6[^{3-/4-}$. This nanostructuration is fundamental to lower the charge transfer resistance at the solid-liquid interface.

From a potentiometric perspective, this electrodeposited bimetallic layer serves a dual purpose. It acts as an effective solid contact between the ion-selective membrane and the underlying electrode, facilitating a stable potential by enabling reversible charge transfer [165,170]. Furthermore, the increased surface area and subsequent membrane, promoting stronger adhesion and stability.

The successful modification of the electrode surface was visually confirmed by scanning electron microscopy (SEM). **Figure 3.3-4** compares the morphology of the bare GSPE (**a**) with the (Au&Ag)NPs modified GSPE (**b**). The SEM image clearly shows the presence of nanoparticles with dimensions smaller than 100 nm, randomly distributed across the graphite surface. The effective modification was further verified by energy-dispersive-X-ray (EDX) spectroscopy (**Figure 3.3-4c**), which identified characteristics signal for gold (bands at 2.2, 9.7, and 11.5 keV) and silver (bands around 3.0 keV), unambiguously confirming the co-deposition of both metals.

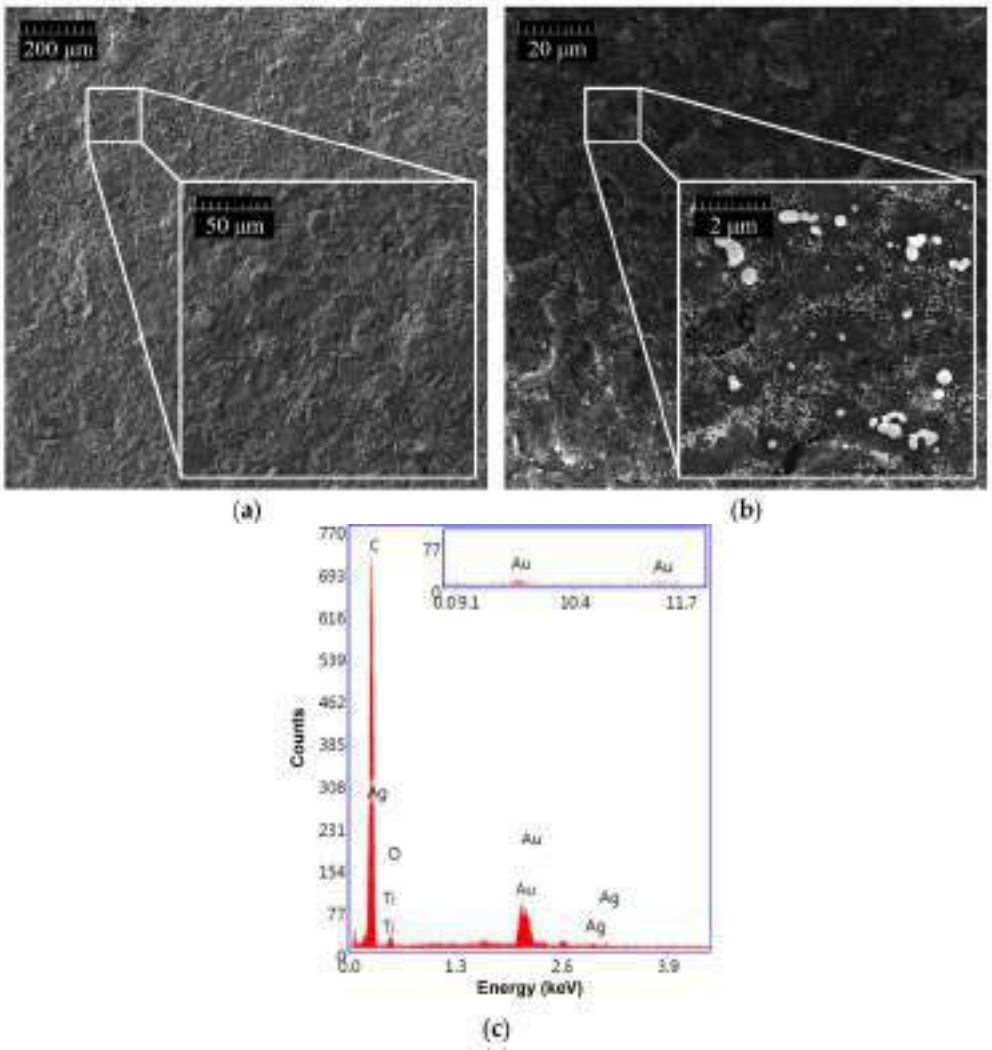

Figure 3.3-4 SEM morphologies of **(a)** bare GSPE and **(b)** (Au&Ag)NPs-modified GSPE. **(c)** EDX spectrum of (Au&Ag)NPs/GSPE.

3.3.10.2 Optimization of The Amount of Lithium Selective Membrane

Achieving a homogeneous and optimally thick coverage of the ion-selective membrane is crucial for a stable and Nernstian sensor response. To this end, the volume of the membrane cocktail deposited onto the (Au&Ag)NPs/GSPE surface was systematically optimised. Sensors were fabricated using 3 µL, 5 µL, and 7 µL of the membrane solution, and their potentiometric response to lithium was characterised (**Table 3.3.10-II**)

Table 3.3.10-II Linear regressions obtained for lithium detection using sensors covered with different volumes of the ion-selective membrane cocktail (n = 5).

Volume (µL)	Slope (mV/decade)
3	47 ± 4
5	58 ± 2
7	46 ± 1

The results reveal a clear trend. Indeed, a volume of 3 µL proved insufficient, yielding a sub-Nernstian slope and poor inter-sensor reproducibility (high standard deviation). This is attributed to incomplete and inhomogeneous coverage of the electrode surface, which fails to provide a consistent population of binding sites. Conversely a volume of 7 µL produced a thicker membrane, resulting in a slower ion-exchange kinetics and a diminished slope, as lithium ions binding to sites in the outer membrane layers become too distant to efficiently influence the phase boundary potential. This decline in performance suggest that an excessive thickness creates a primary resistance to ion migration. In potentiometry, the potential is generated at the phase boundary; a membrane that is too thick may lead to a 'bulk' effect when the slow diffusion of Li^+ ions through the polymer matrix increases the ohmic drop and delays the establishment of a stable equilibrium, thus resulting in a sub-Nernstian slope.

The 5 µL volume emerged as the optimal compromise, delivering a near-Nernstian slope of 58± 2 mV/decade and excellent reproducibility, this volume ensures complete surface coverage with a membrane thickness that facilitates rapid ion diffusion and effective transduction of the binding event. Consequently, 5 µL was selected as the standard volume for all subsequent sensor fabrication.

3.3.10.3 Optimization of The Supporting Electrolyte Concentration

The composition of the measurement solution, particularly the ionic strength provided by a supporting electrolyte, significantly affects the stability and sensitivity of potentiometric sensor. $MgCl_2$ has been chosen for this role, and its concentration has been optimized across a range from 0.01 M to 0.5 M.

The corresponding calibration curves (**Figure 3.3-5**) and their linear regressions (**Table 3.3.10-III**) demonstrate a pronounced dependency of the sensor's performance on this parameter

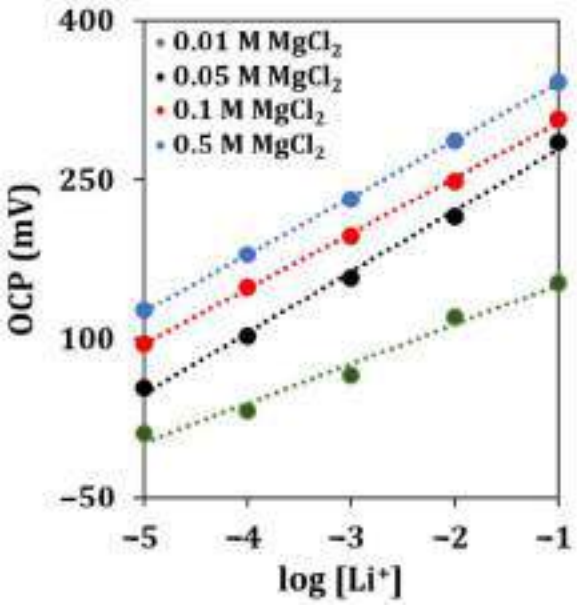

Figure 3.3-5 Lithium calibration curves obtained with different concentrations of the supporting electrolyte solution by OCP measurements (n = 5).

Table 3.3.10-III Analytical performance for lithium detection in standard solutions with different concentrations of $MgCl_2$ supporting electrolyte (n = 5).

[$MgCl_2$] (M)	Slope (mV/decade)
0.01	37 ± 13
0.05	56 ± 2
0.1	52 ± 1
0.5	54 ± 1

A concentration of 0.01 M $MgCl_2$ resulted in an unstable and highly variable sub-Nernstian response, indicating insufficient ionic strength to maintain a stable junction potential and consistent activity coefficient, while higher concentrations (0.1 M and 0.5 M) provided stable and reproducible slopes but with a slight reduction in sensitivity.

The optimal response, characterised by a near-Nernstian slope of 56 ± 2 mV/decade and excellent repeatability, was achieved with a 0.05 M $MgCl_2$ solution. This concentration provides the ideal ionic strength to ensure stable potential readings without introducing significant interference or attenuating the sensor's sensitivity to lithium activity. Therefore, 0.05 M $MgCl_2$ has been established as the standard supporting electrolytes for all further measurements.

3.3.10.4 LITHIUM DETECTION IN STANDARD SOLUTIONS

Under optimized experimental conditions, lithium detection was performed via OCP measurements in a drop configuration. The sensor's response time and signal stability has been assessed by recording the potential over a 100-second interval for solutions of varying lithium concentrations (**Figure 3.3-6a**). The OCP values measured at a fixed time of 90 seconds for each concentration were plotted against the logarithm of the lithium concentration, yielding a linear calibration curve (**Figure 3.3-6b**).

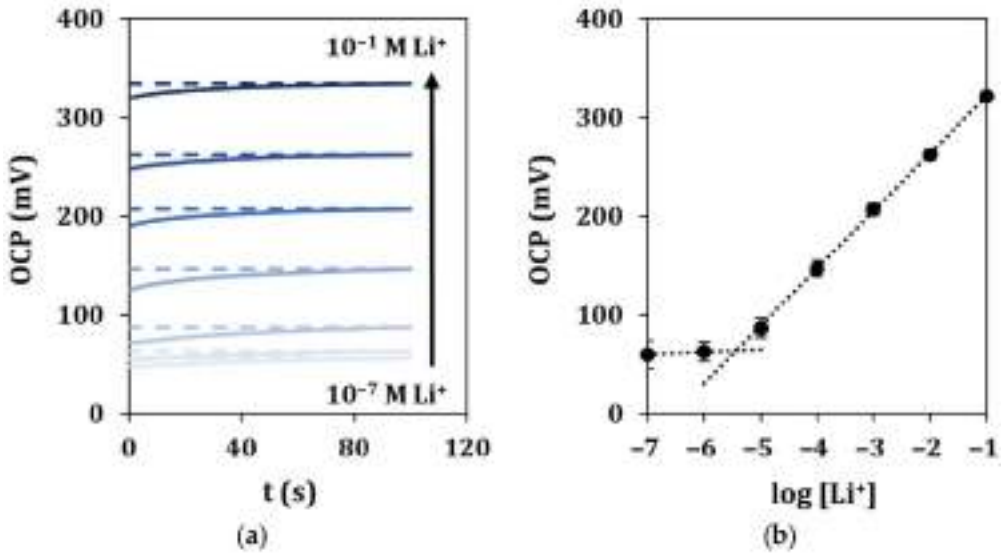

Figure 3.3-6 Lithium detection in standard solutions. **(a)** Recorded OCP signals vs. time for a total duration of 100 s, and **(b)** corresponding calibration curve. Each measurement was repeated at least 5 times using the same sensor (reprinted with the permission of).

The sensor demonstrated an average response time of 45 seconds, defined as the time required to reach 90% of the maximum equilibrium potential. A linear response has been observed across the range of 10^{-5}–10^{-1} M, described by the equation $E = (58 \pm 3)\text{Log}[Li^+] + (380 \pm 7)$, with a correlation coefficient (R^2) of 0.9998. The calculated limit of detection (LOD) was 1.6 10^{-6} M. The sensor exhibited excellent repeatability, with a relative standard deviation (%RSD) value below 4% across five consecutive calibrations. Furthermore, it displayed strong operational stability, showing a low potential drift of only 3 mV/h during continuous 5-hour measurement of a 0.1 M Li^+ solution.

Lastly, the sensor's longevity was also promising. Indeed, while a gradual loss of performance has been observed after 36 hours -likely due to membrane detachment- the sensor maintained full functionality over a standard 48-hour testing period. Notably, its storage stability was outstanding: when stored in dry, dark conditions at room temperature, the sensor retained its original analytical sensitivity for at least one month.

3.3.10.5 INTERFERENCE STUDY

The key performance metric for an ion-selective electrode is its selectivity, quantified by the potentiometric selectivity coefficient ($K^{pot}_{A,B}$). The sensor's selectivity has been evaluated against common physiological cations (K^+, Na^+, NH_4^+, Ca^{2+}) using the Fixed Interference Method. The resulting log($K^{pot}_{A,B}$) values are summarised in **Table 3.3.10-IV**.

Table 3.3.10-IV Potentiometric selectivity coefficient (log $K^{pot}_{A,B}$) for the developed lithium sensor.

Interferent Ion	Log($K^{pot}_{A,B}$)
K^+	-1.89 ± 0.72
Na^+	-2.45 ± 0.51
NH_4^+	-2.55 ± 1.02
Ca^{2+}	-4.82 ± 0.94

As anticipated, the sensor showed the highest selectivity against the doubly charged Ca^{2+} ion. The most significant interference has been observed by K^+ and Na^+, whose ionic radii are similar to that of Li^+, leading to a degree of competition for binding sites within the ion-selective membrane. Nevertheless, the significantly negative selectivity coefficient for all interferents confirm the membrane's strong performance for Li^+, which is sufficient for accurate measurement in complex biofluids where these ions are present. The selectivity coefficients against Na^+ and K^+ (Table 3.3.10-IV) are particularly significant given their high consideration in sweat and saliva. The value of log $K^{pot}_{Li,\ Na}$= -2.45 indicates that sensor is nearly 300 times more sensitive to Li^+ than to Na^+. This discrimination factor, despite the smaller ionic radius of Li^+, confirms that the Lithium Ionophore VI effectively creates a coordination cavity that size-matches the dehydrated lithium ion, successfully excluding larger alkaline cation present in biofluids.

3.3.10.6 ANALYSIS IN SYNTHETIC SALIVA AND SWEAT

Following characterisation in standard solutions, the sensor's performance has been validated in clinically relevant complex matrices: synthetic saliva and sweat. Calibration curves were successfully obtained in both media (**Figure 3.3-7**.

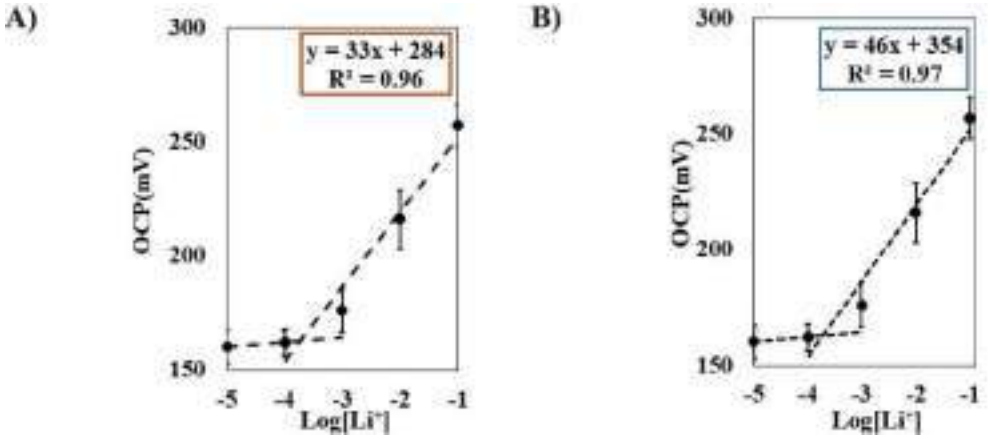

Figure 3.3-7 Lithium detection in synthetic A) saliva and B) sweat. Each measurement was repeated at least 3 times using the same sensor **[168]**.

As it can be observed, the sensor maintained a linear response in the range of 10^{-4}–10^{-1} M Li^+ in these challenging matrices. The calculated LODs were 0.4 mM in synthetic sweat and 1.5 mM in synthetic saliva. These detection limits are critically positioned within the reported therapeutic concentration ranges for lithium in these biofluids: 1.0–4.8 mM for sweat and 1.6–2.5 mM for saliva [171,172]. This alignment confirms that the developed (Au&Ag)NPs/GSPE-based sensor possesses the necessary sensitivity and robustness for the direct, quantitative detection of lithium in peripheral biofluids, highlighting its strong potential for translation into a practical point-of care tool for managing bipolar disorders.

3.3.11 Conclusion

This chapter successfully demonstrates that the strategic fusion of nanomaterial and electroanalytical chemistry can yield practical solutions for pressing clinical monitoring needs. By leveraging the versatility of screen-printing and enhancing graphite electrodes with a tailored bimetallic nanostructure of gold and silver, a solid-contact platform that overcomes key stability challenges in potentiometry has been presented. The resulting sensor is not merely a functional prototype; it is a convincing proof-of-concept that answers the call for decentralised lithium monitoring. Indeed, its analytical performances, characterised by a wide linear range, a low micromolar detection limit, and, crucially, a robust selective profile, translates effectively from controlled buffer solutions to the complex, saline environment of synthetic sweat or saliva. The progression from fundamental material modification to validated operation in complex matrices established a strong foundation for the future development of this sensing strategy into wearable or

portable formats, with the potential to support more personalised management of bipolar disorders.

3.4 ACKNOWLEDGMENT

This work was developed in collaboration with Dr. Giulia Selvolini and Prof. Giovanna Marrazza, whose support is gratefully acknowledged.

Note on Publications: The research detailed in this chapter has led to the following peer-reviewed publications, in which the author of this thesis is a contributing co-author:

1. Vitale, I.A.; Selvolini, G.; Marrazza, G. Smart Sensor for Lithium Detection: An Environmental Application. *Chemosensors* **2023**, *11*, 77. https://doi.org/10.3390/chemosensors11020077
2. Vitale, I.A., Selvolini, G., Marrazza, G. (2025). Lithium Detection in Peripheral Biofluids Using a Smart Electrochemical Sensor. In: Conoci, S., Di Natale, C., Prodi, L., Valenti, G. (eds) Sensors and Microsystems. AISEM 2024. Lecture Notes in Electrical Engineering, vol 1334. Springer, Cham. https://doi.org/10.1007/978-3-031-82076-2_4

Financial support was provided by the European Union—Next Generation EU, in the context of The National Recovery and Resilience Plan, Investment 1.5 Ecosystems of Innovation, Project Tuscany Health Ecosystem (THE), CUP: B83C22003920001 and by Regione Toscana (grant number 3553.04032020.158000224) within the project RI.B.AT (Riciclo Integrato Batterie AutoTrazione) in the framework of POR FESR 2014/2020.

4. TOWARD WEARABLE NEUROLOGICAL HEALTH MONITORING: A SWEAT-BASED SENSOR FOR DOPAMINE

4.1 Neurological Disorders and the Diagnostic Challenge

The term *Neurological Disorders* encompasses conditions affecting the nervous system due to structural, biochemical, or electrical abnormalities in the brain, spinal cord, or nerves, leading to a wide spectrum of symptoms. As defined by the Global Burden of Disease Study, this category includes Alzheimer's disease and other dementias, Parkinson's disease, multiple sclerosis, epilepsy, and headache disorders such as migraine [67,173].

The onset of these disease carries severe consequence, including motor impairments (e.g. bradykinesia, tremor, hypokinesia in Parkinson's disease), cognitive decline, dementia, depression, speech alterations (as in Alzheimer's disease), and, in severe cases, premature mortality [174]

Despite their profound impact on individuals and societies, the epidemiology of neurological disorder, including geographical and temporal variations in frequency and associated risk factors- remains poorly understood. Furthermore, patients often require significant long-term social and economic support due to disability, yet healthcare resources and services for these conditions are disproportionately scarce [175,176].

A critical unmet need in this field is the lack of methods for early detection, ideally before the onset of overt symptoms. Early diagnosis is crucial, as pharmacological interventions are typically more effective in the initial stage of disease, potentially slowing progression and enabling timely management with targeted therapies. Currently, definitive diagnosis often relies on the analysis of cerebrospinal fluid (CSF), an invasive and hospital-based procedure that carries inherent risk for the patient [177]. In fact, CSF is a rich source of protein and genetic biomarkers, such as Tau Total protein, Amyloid β peptide, Vesicle Integral membrane protein 1, α-synuclein [178–195] which are central to the pathology of various neurodegenerative diseases. The invasive nature of CSF collection fundamentally limits its utility for widespread screening or continuous monitoring, creating a pressing demand for alternative, accessible diagnostic strategies.

4.2 The Potential Role of Sweat In the Early Diagnosis of Neurological Disorders

The pursuit of non-invasive diagnostic pathways has led to a re-evaluation of peripheral biofluids as mirrors of central nervous system activity. Among these, eccrine sweat presents a uniquely accessible source of physiological relevant information, due to its intrinsic connection to the autonomic nervous system and its rich, if underutilised, molecular composition.

Eccrine sweat glands are densely innervated by sympathetic cholinergic and adrenergic fibres, placing their secretion under direct neural control [196,197] This neuro-glandular links is not merely anatomical; it is functionally evident. The modulation of sweating through pharmacological agents targeting these pathways demonstrates a synergistic dialogue between the central nervous system and integumentary system [198,199]. Consequently, the molecular profile of secreted sweat is not a simple ultrafiltrate, but a dynamic output influenced by central and autonomic nervous system states.

From a diagnostic perspective, sweat offers a complex matrix. Beyond its primary electrolytes, it contains a spectrum of endogenous small molecules, including lactate, urea, ammonia, amino acids, steroids, and hormones, whose levels can Au reflect systemic metabolic and endocrine status [200,201]. Critically for neurodegenerative and psychiatric research, advanced proteomic and metabolomic studies have identified the presence in sweat of proteins and metabolites with established links to cerebral function and dysfunction, offering a potential, non-invasive window into central nervous system pathology [202].

These attributes position to sweat as a highly promising medium for “next-generation” digital biomarkers, capable of enabling painless, continuous health monitoring [203]. However, a significant translation gap persists. While sweat tests are clinically established for disorders like cystic fibrosis, their application to neurological disorders remains virtually non-commercialised [204]. This disparity stems from acknowledged challenges, including the low absolute abundance of many protein biomarkers in sweat and the ongoing validation of neurological disorders-specific molecular signatures. This gap, however, defines the research opportunity. Rather than competing with blood on protein concentration, sweat-based neurological monitoring may find its niche in tracking other classes of molecules, such as key neurotransmitters or their metabolites, that are reflective of neurochemical activity and accessible through this conduit. Among these,

dopamine represents an ideal target analyte. Indeed, its central role in motor function and reward processing, together with its well-established dysregulation in Parkinson's disease, makes it a critical biomarker. Successfully monitoring its dynamics in sweat would provide an unprecedented, patient-friendly window into dopaminergic neurotransmission.

4.3 Sweat Dopamine Monitoring Using Amino Acid-Based Electrochemical Sensors

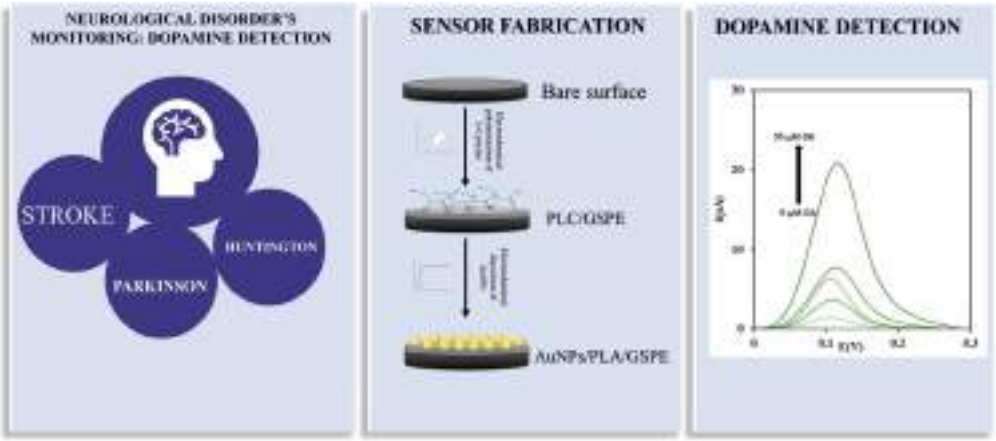

4.3.1 Figure 4.3-1. Graphical Abstract of dopamine sensing platform for neurological disorder monitoring. The infrastructure integrates a biocompatible interface designed through a two-step electro-fabrication process: (i) electropolymerization of L-Cysteine and (ii) electrodeposition of gold nanoparticles (AuNPs). The resulting nanostructured sensor enables sensitive dopamine detection via Differential Pulse Voltammetry (DPV), providing a robust tool for personalized management of conditions such as Parkinson's and Huntington's disease. **State of Art**

The imperative for non-invasive monitoring of neurological health directs research toward the detection of key neurochemicals in accessible biofluids. As established in the previous section, sweat represents a promising conduit for such analysis, with dopamine (DA) emerging as a critical target analyte due to its central role in neurodegenerative disorders onset. The World Health Organization (WHO) has accordingly designated DA as a priority analyte for neurological disorder management, underscoring the need for precise, frequent quantification to optimize therapeutics [205].

In this context, electrochemical sensors are ideally suited to meet this demand to afford a continuous, PoC monitoring, offering high sensitivity, miniaturisation potential, and cost-

effectiveness [206]. The growing field of wearable electrochemical (bio)sensors (WEBs) leverages these advantages, aiming to translate laboratory-grade analysis into user-friendly devices for longitudinal tracking [207]. However, a significant translation hurdle for WEBs intended for prolonged skin contact is biocompatibility. Indeed, conventional sensor materials, including many conductive polymers, derived from toxic monomers, posing potential risks that are unacceptable for wearable applications [208].

This challenge has catalysed the exploration of sustainable, biocompatible alternatives. Amino acid-based conductive polymers have recently emerged as a promising next-generation material class, offering enhanced biosafety without compromising electrochemical functionality [135,209].

. Among these, poly-L-cysteine (PLC) is particularly attractive. Furthermore, the performance of such polymeric films can be synergically enhanced by integration with nanostructured materials. Gold nanoparticles (AuNPs), renowned for their excellent electrocatalytic properties and biocompatibility, are ideal candidates [210]. Their *in-situ* electrodeposition allows for precise control over morphology and distribution, tailoring the interface for specific analytical challenges.

Therefore, the integration of biocompatible polymers with a nanostructured electrocatalyst like AuNPs presents a compelling strategy to construct a sensing platform that satisfies the dual requirements of high performance and wearable safety. This section details the development and characterisation of such a platform, specifically designed for the detection of dopamine in sweat.

The sensing platform is fabricated on graphite screen-printed electrodes (GSPEs) through a sequential functionalization process: first the electropolymerization of a PLC or poly-L-Aspartic acid (PLA) layer, followed by the electrodeposition of AuNPs. The optimised platforms are systematically characterised to evaluate their interfacial properties, stability, and selectivity. Their analytical performances for dopamine detection are rigorously validated first in buffer solutions and, critically, in undiluted artificial sweat, confirming its viability for non-invasive monitoring applications. This work demonstrates a valuable pathway toward a new generation of biocompatible, wearable sensors for personalised neurological health management.

4.3.2 Chemicals

All chemicals, including dopamine hydrochloride ($C_8H_{11}NO_2 \cdot 2H_2O$), L-Ascorbic acid ($C_6H_8O_6$), L-Cysteine ($C_3H_7NO_2S$), L-Aspartic acid ($C_4H_7NO_4$), disodium hydrogen

phosphate (Na_2HPO_4), potassium dihydrogen phosphate (KH_2PO_4), sodium chloride (NaCl), potassium chloride (KCl), potassium ferrocyanide ($K_4[Fe(CN)_6]$), potassium ferricyanide ($K_3[Fe(CN)_6$ tetrachloroauric acid ($HAuCl_4$), sulfuric acid (H_2SO_4) were procured from Merck (Milan, Italy). All solutions were prepared using Milli-Q water. Phosphate-buffer saline (PBS, pH 5.5) has been formulated with 137 mM NaCl, 2.7 mM KCl, 10 mM Na_2HPO_4, 1.8 mM KH_2PO_4 in Milli-Q water. Following an adapted literature composition[168], synthetic sweat has been prepared at pH 5.3 containing 6 mM KCl, 5 mM NH_4Cl, 0.08 mM $MgCl_2$, 2.6 mM $NaHCO_3$, 0.04 mM Na_2HPO_4. Synthetic saliva was also prepared at pH 5.3 with a composition of 2.2 mM NaCl, 12.9 mM KCl, 1.9 mM KSCN, 4.8 mM KH_2PO_4, 3.3 mM urea, 2.4 mM Na_2SO_4, 3.3 mM NH_4Cl, 1.5 mM $CaCl_2$, 7.5 mM $NaHCO_3$.

4.3.3 Apparatus

The experimental setup has been based on commercially available screen-printed electrochemical cells (SPCs, EcoBioServices srl, Sesto Fiorentino, Italy). Their three-electrodes configuration consisted of a graphite working electrode, a graphite counter electrode, and a silver pseudo-reference electrode. All measurements were performed at room temperature using portable potentiostat/galvanostat Sensit Smart electrochemical analyser (PalmSens BV, Houten, The Netherlands) connected to an Android© smartphone equipped with PSTouch software for data acquisition and elaboration. All experiments were conducted at room temperature.

4.3.4 Electrochemical Sensors Modifications

Graphite screen-printed electrodes (GSPEs) were modified with poly-L-Cysteine (PLC) film and electrodeposited gold nanoparticles (AuNPs) to obtain a nanostructured sensing platform (AuNPs/PLC/GSPEs). The L-Cysteine electropolymerization has been performed by depositing 50 µL of a 10 mM L-cysteine solution in PBS (pH 7.4) onto the electrode surface. Cyclic voltammetry (CV) was then applied for 10 cycles within a potential window of -1.0 V to 1.2 V (vs Ag/AgCl reference) at a scan rate of 0.1 Vs^{-1}. A thorough rinsing step with Milli-Q water has been performed on the PLC-functionalised electrode, followed by a drying phase at room temperature.

For comparison, a separate set of electrodes has been functionalized with poly-L-Aspartic acid (PLA). This involved depositing 50 µL of a 10 mM L-aspartic acid solution in PBS

onto GSPE and subjecting it to 10 CV cycles from -0.8 V and +1.2 V at a scan rate of 0.1 Vs^{-1}.

Following polymer formation, gold nanoparticles were electrodeposited onto both the PLC and PLA surfaces via chronoamperometry. A 50 µL of 2 mM $HauCl_4$ in 0.5 M H_2SO_4 was applied to the modified electrode, and a constant potential of −0.2 V was applied for 150 seconds. The final step involved washing the newly fabricated AuNPs/PLC/GSPE and AuNPs/PLA/GSPE platforms with Milli-Q water. These platforms were then left to dry under room conditions for 24 hours before any electrochemical use. A schematic representation of the electrochemical sensor fabrication process for DA detection is reported in **Figure 4.3-1**

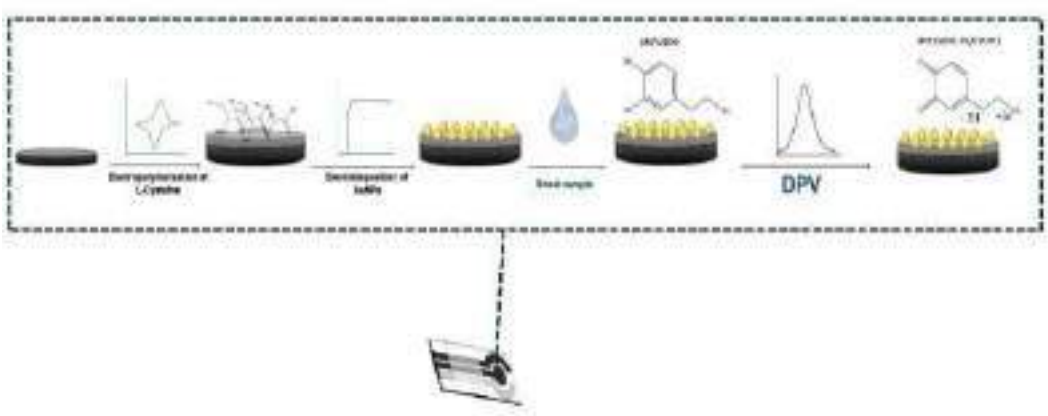

Figure 4.3-1 Schematic illustration of the stepwise functionalization of graphite screen-printed electrodes (GSPE) and its application for the electrochemical sensing of dopamine (DA).

4.3.5 Electrochemical Characterisation

To evaluate the performance of the nanostructured platform surfaces, electrochemical investigations have been conducted. Specifically, Cyclic Voltammetry (CV) and Electrochemical Impedance Spectroscopy (EIS) measurements have been employed to assess each modification step by monitoring changes in the electrochemical behaviour of the $[Fe(CN)_6]^{3-/4-}$ redox marker. This probe was selected because its response is primarily sensitive to alterations in surface structurization rather than changes in its electronic density of states (DOS) (https://doi.org/10.1021/ac070474h).

In order to calculate the electroactive area of the resulted platforms, CV has been performed using 50 µL of 5 mM redox marker $[Fe(CN)_6]^{3-/4-}$ in 0.1 M KCl. Initially, the potential has been cycled between -1.0 and 1.0 V at a fixed scan rate to obtain the

characteristic oxidation and reduction peak currents (I_p). Subsequently, the scan rate has been varied from 0.025 Vs^{-1} up to 0.150 Vs^{-1}, which resulted in a gradual increase in I_P. The electroactive area has been then calculated using the Randles-Ševčik equation was applied to determine the electroactive area:

$$I_p = 2.686 \cdot 10^5 \cdot z^{3/2} A D^{1/2} C v^{1/2}$$

In this equation, n represents the number of electrons exchanged, A denotes the electrode area (cm^2), D is the analyte's diffusion coefficient (cm^2s^{-1}) and C is the probe concentration (mol/cm^3).

EIS measurements were also performed for each modification step at different concentrations (0.1, 0.2, 0.5, 1, 2, 5 mM) of $[Fe(CN)_6]^{-4/-3}$ redox probe (equimolar solution prepared in 0.1 M KCl). The obtained R_{ct} values were plotted against the inverse of the concentration ($1/C$) and the resulting curves were fitted with the following equation

$$R_{Ct} = \frac{RT}{n^2 F^2 A k^0} \cdot 1 / C$$

where R (8.3145 J/(mol·K)) is the gas constant, T (K) is the temperature, n is the number of electrons transferred in the redox event, F (96500 C/mol) is the Faraday constant, A (m^2) is the electroactive surface area and k^0 (cm/s) is the electron transfer rate constant.

The tested SPEs were discarded after each CV or EIS measurement.

4.3.6 Dopamine Detection with Cyclic Voltammetry (CV) and Differential Pulsed Voltammetry (DPV) in Standard solutions

The evaluation of DA oxidation peak position has been evaluated by the meaning of cyclic voltammetry (CV), switching the potential between -0.4 V and 0.8 V as a potential window, using 0.1 Vs^{-1} as scan rate, using the different modified platforms. Onto the modified surfaces were dropped 50 µL of 1 mM Dopamine and obtained peak height was chosen as the analytical signal.

After the assessing of DA oxidation behaviour in positive potentials, DA calibration curves were obtained using the differential pulse voltammetry (DPV) by scanning the potential from 0 V to 0.5 V, at 0.004 Vs^{-1} (0.002 V step potential, 0.05 V pulse potential, 0.05 s pulse time). To minimize sample consumption, all measurements have been conducted in a drop-analysis setup. In this configuration, the modified platform has been incubated with 50 µL droplets of PBS containing dopamine at varying concentrations (1-

100 of μM). The faradic current peaks (i_p) provided the electrochemical readout, with concentration dependence established through DA calibration curves.

4.3.7 Sensor Validation in Artificial Sweat

The analytical performance of the proposed sensors has been initially verified in a complex, synthetic matrix, to demonstrate its potential for real-world use. The artificial sweat has been spiked with increasing concentrations of Dopamine ranging from 0 up to 100 μM to simulate a real range on human body, underlining the feasibility of a further application as on body continuous detection.

4.3.8 Results and Discussion

4.3.8.1 Modification of GSPEs with Poly-L-Cysteine (PLC), Poly-L-Aspartic Acid (PLA) and Gold Nanoparticles

The development of a high-performance sensing interface began with the optimisation of the polymeric underlayer and the subsequent nanostructuring with gold. The first step investigated during this process is the poly-L-aspartic (PLA) deposition as a model biocompatible polymer. Indeed, PLA can be readily electropolymerized onto the carbon surfaces via cyclic voltammetry (CV), where the electrooxidation of the monomer generates surface-bound radicals that form a stable, negatively charged polymeric film, useful for subsequent functionalisation

The properties of the electrodeposited film can be easily tuned by varying its thickness, which can be realized by controlling the amount of charge passing during the polymerization event; therefore, the optimization of the Voltammetric parameters results to be of outstanding importance.

For this purpose, the polymerisation of PLA has been systematically optimized by varying the concentration of the L-Aspartic monomer (0.5-5 mM) and the number of CV cycles (10-30). The resulting PLA/GSPEs were characterized by CV and EIS using mM $[Fe(CN)_6]^{-4/-3}$ redox probe (**Figure 4.3-2).**

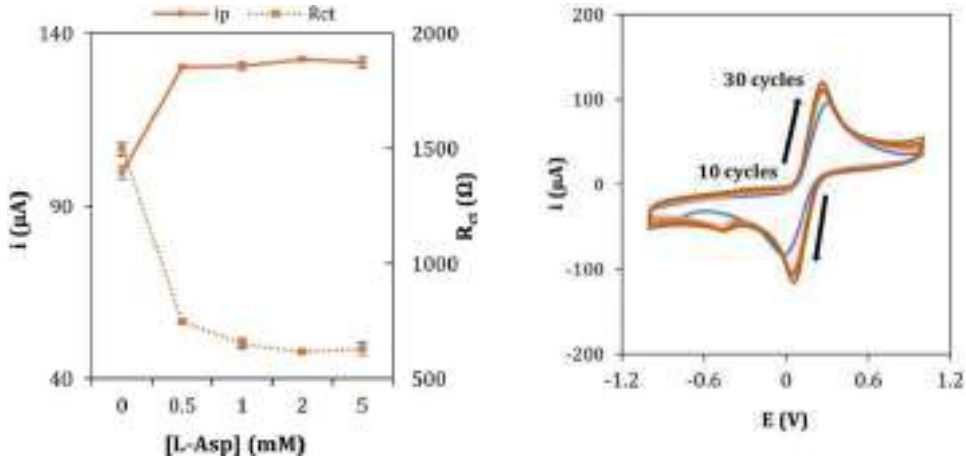

Figure 4.3-2 a) Peak current and R_{ct} values of poly(l-aspartic acid)-modified GSPEs in 5 mM $[Fe(CN)_6]^{-4/-3}$ (equimolar solution prepared in 0.1 M KCl) at different L-Asp concentrations (polymerization cycles: 20). **b)** CV and **c**) EIS characterization of • bare and • poly(L-aspartic acid)-modified GSPEs in 5 mM $[Fe(CN)_6]^{-4/-3}$ (equimolar solution prepared in 0.1 M KCl) at different polymerization cycles ([L-Asp]=2 mM).

The peak current and charge transfer resistance (R_{ct}) exhibited complementary behaviours. A monomer concentration of 2 mM yielded the maximum current and minimum R_{ct}, indicating optimal film permeability and conductivity, and was thus selected for all further experiments.

Similarly, the number of polymerisation cycles significantly influenced the interface. The peak current increased with cycle number up to 30, while R_{ct} decreased, suggesting the formation of a thicker yet sufficiently conductive polymer network. However, when these optimised PLA films (20 and 30 cycles) have been further modified with electrodeposited AuNPs, their subsequent electrochemical profiles became virtually identical (**Figure**

4.3-3). Therefore, 20 cycles have been chosen as the optima balance between fabrication time and performance.

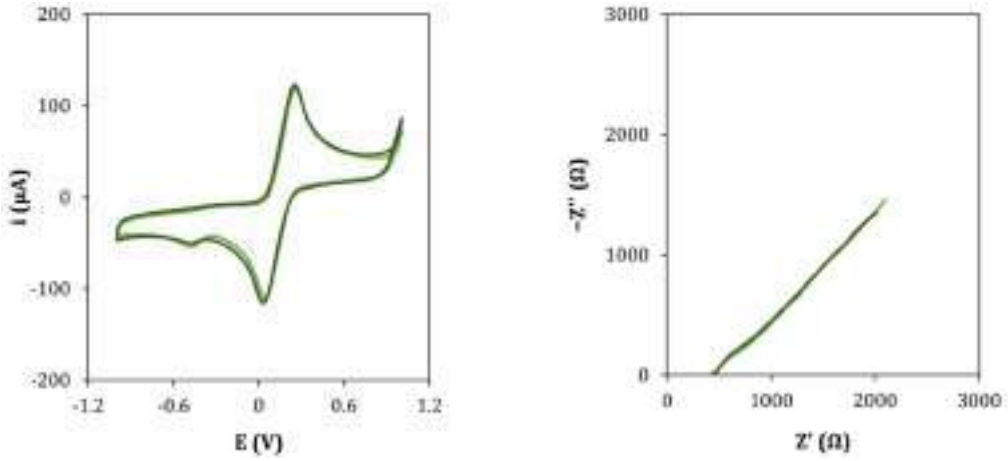

a) **b)**

Figure 4.3-3 a) CV and **b)** EIS characterization of AuNPs/p(L-Asp)/GSPEs in 5 mM $[Fe(CN)_6]^{-4/-3}$ (equimolar solution prepared in 0.1 M KCl) with ● 20 and ● 30 polymerization cycles (gold deposition time: 130 s).

The AuNPs deposition step itself was then fine-tuned. The concentration of the $HAuCl_4$ precursor has been varied (0.05-0.5 mM) and the electrodeposition time (70-190 s) via chronoamperometry has been investigated. As shown in

Figure 4.3-4, the highest precursor concentration (0.5 mM) yielded the greatest enhancement in electron transfer. While longer deposition times increased conductivity, the gains diminished after 130 s. Consequently, 0.5 mM $HAuCl_4$ and 130 s deposition time have been established as the standard conditions for creating the AuNPs/PLA/GSPE platform.

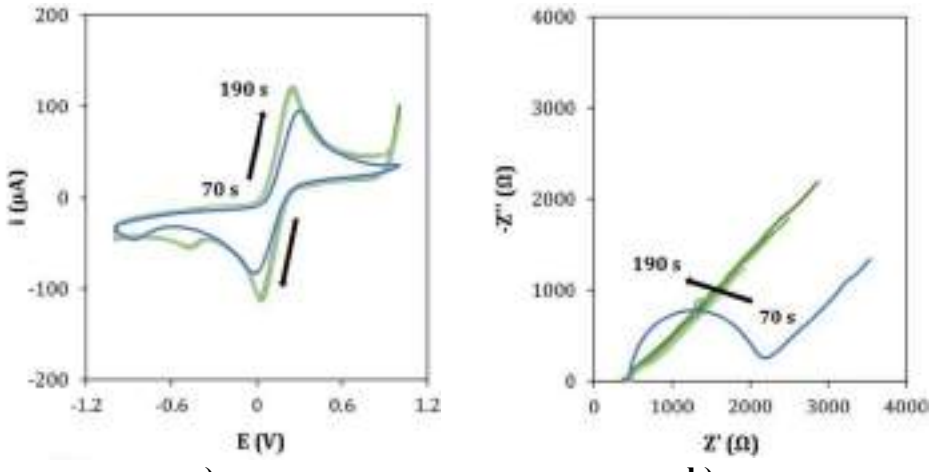

a) **b)**

Figure 4.3-4 a) CV and **b)** EIS characterization of • bare and • AuNPs/p(l-Asp)/GSPEs in 5 mM $[Fe(CN)_6]^{-4/-3}$ (equimolar solution prepared in 0.1 M KCl) at different gold deposition times ($[HAuCl_4]$=0.5 mM).

The optimised platform was characterised in 0.1 M KCl (**Figure 4.3-5**). The distinct redox peak observed only for electrodes modified with AuNPs (both on bare and PLA-coated GSPE) confirmed the successful deposition of electroactive gold.

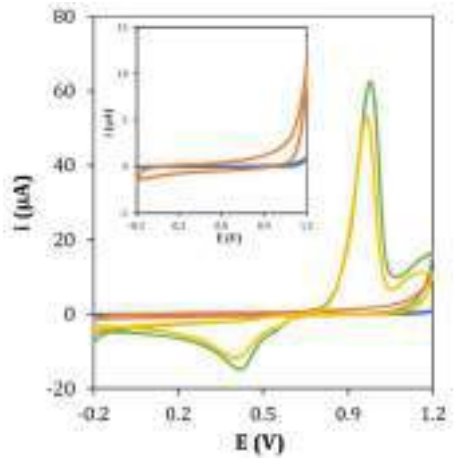

Figure 4.3-5 CV characterization of ● bare, ● p(L-Asp)/GSPEs, ● AuNPs/GSPEs and ● AuNPs/p(LAsp)/GSPEs in 0.1 M KCl. Inset: enlarged CV scans of ● bare and ● p(L-Asp)/GSPEs in 0.1 M KCl

Furthermore, SEM and EDX spectroscopy provided direct morphological and elemental confirmation, showing randomly distributed AuNPs on the electrode surface and a clear gold signal at ~2.2 keV. (**Figure 4.3-6**)

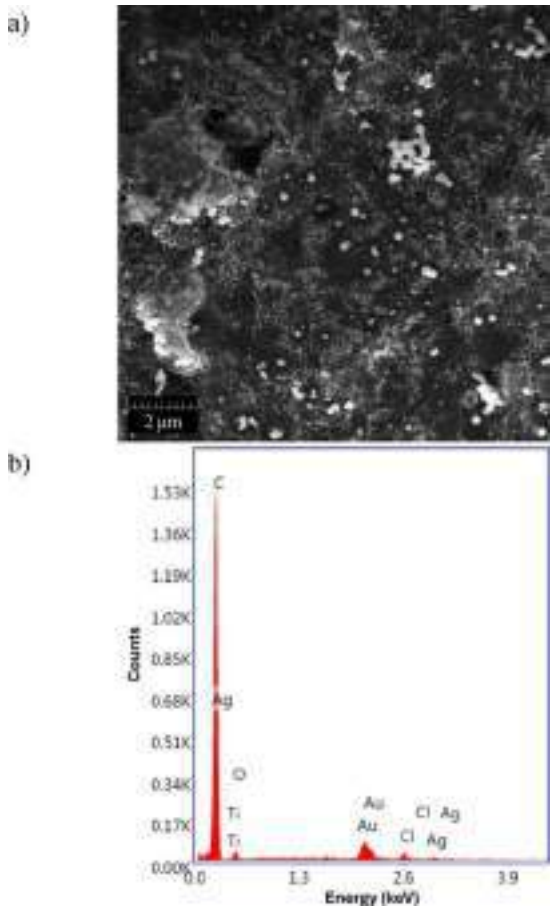

Figure 4.3-6 Microscopic characterization of the nanostructured platform. **a)** SEM morphology of AuNPs/p(l-Asp)/GSPEs and **b)** EDX spectrum of AuNPs/p(L-Asp)/GSPEs.

Parallel to the PLA study, poly-L-cysteine (PLC) has been explored as an alternative amino acid-based polymer. A similar optimisation protocol was followed (**Table 4.3.8-I**). Electropolymerization of L-cysteine from a 10 mM solution for 10 cycles provided the most reproducible film (RSD < 10%). Subsequent AuNPs deposition from a 2 mM $HAuCl_4$ solution for 150 s at -0.2 V produced the AuNPs/PLC/GSPE platform with optimal electron transfer characteristics and acceptable reproducibility (RSD < 12%).

Table 4.3.8-I Optimization L-Cysteine concentrations for electropolymerization in PBS (0.1 M pH 5.5), number of cycles optimization and AuNPs concentrations. Peak currents from $[Fe(CN)_6]^{3-/4-}$ probe in 0.1 M KCl. CV performed in the potential range of -1 V to 1 V at 0.1 V/s.

Modification	Concentration (mM)	Number of Cycles	Anodic Peak Height (µA)	Cathodic Peak Height (µA)	SD (µA)
PLC/GSPE	**1**	10	102	98	±34
	2	10	94	95	±21

	5	10	91	93	±35
	10	10	90	92	±10
PLC/GSPE	10	**5**	99	94	±24
	10	**10**	117	115	±15
	10	**15**	137	135	±40
	10	**20**	102	101	±21
AuNPs/PLC /GSPE	**0.25**	-	120	98	±37
	0.5	-	130	93	±21
	1	-	151	102	±31
	2	-	154	81	±15

Two distinct, optimised nanocomposite platform have been successfully fabricated: AuNPs/PLA/GSPE and AuNPs/PLC/GSPE. The following section details their comparative analytical characterisation for dopamine detection, including interfacial behaviour, sensitivity, selectivity, and performance in synthetic sweat, in order to identify the most suitable platform for wearable neurological monitoring applications.

4.3.8.2 Electrochemical Characterisation of Modified GSPEs

Having established the optimised fabrication protocols, a detailed electrochemical characterisation has been undertaken to evaluate how each modification step altered the interfacial properties of the electrode. This analysis served not merely to confirm successful modifications, but to provide a quantitative comparison of the electron transfer efficiency between the two poly-amino acid platforms, which is fundamental for their subsequent performance as sensors.

The investigation began with CV using $[Fe(CN)_6]^{-4/-3}$ redox probe across a range of scan rates. As illustrated in **Figure 4.3-7**, each modification step- first the polymer deposition and then the AuNPs electrodeposition- included a pronounced change in the Voltammetric profile.

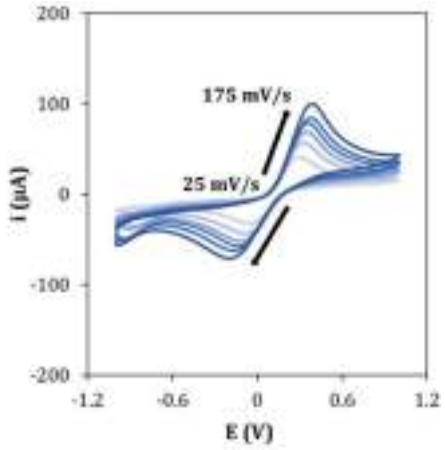
175 mV/s
25 mV/s
i (µA)
E (V)

a)

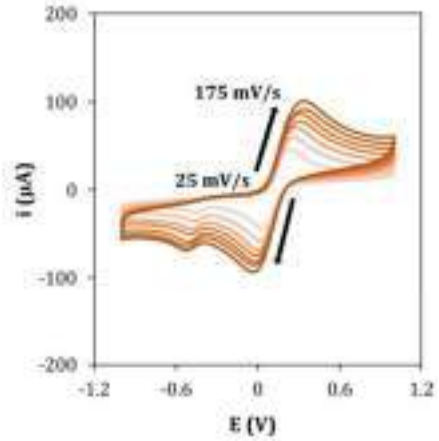
175 mV/s
25 mV/s
i (µA)
E (V)

b)

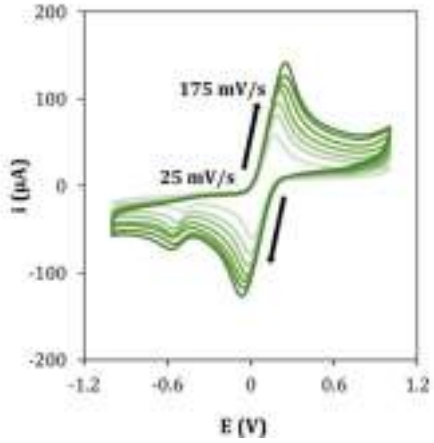
175 mV/s
25 mV/s
i (µA)
E (V)

c)

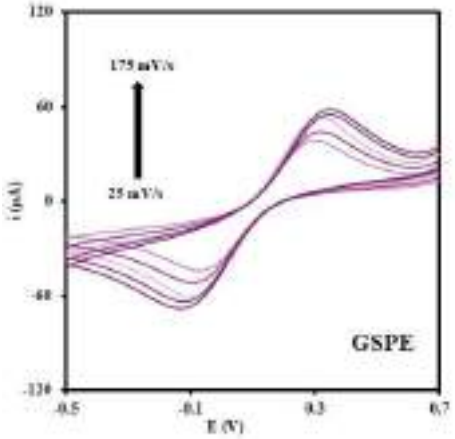
175 mV/s
25 mV/s
GSPE

d)

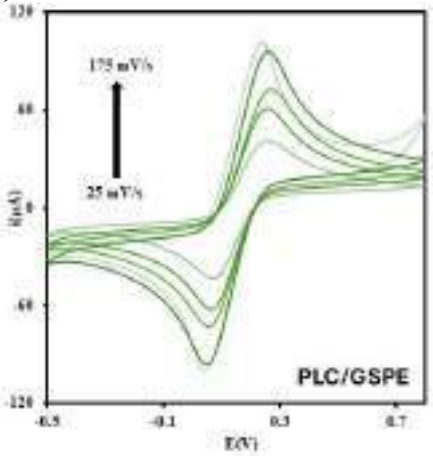
175 mV/s
25 mV/s
PLC/GSPE

e)

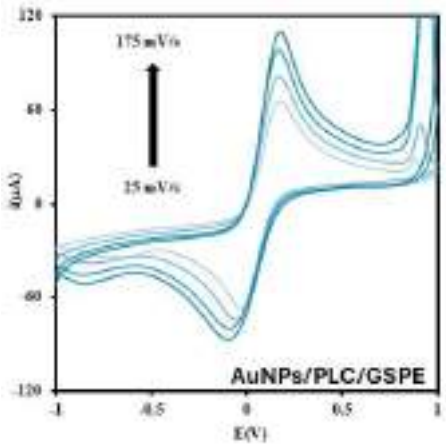

f)

Figure 4.3-7 CV characterization of unmodified GSPEs and nanocomposite-modified GSPEs in 5 mM $[Fe(CN)_6]^{-4/-3}$ (equimolar solution prepared in 0.1 M KCl) at different scan rates**. a)** GSPEs; **b)** PLA/GSPEs; c) AuNPs/PLA/GSPEs. **d)** GSPE**; e**) PLC/GSPE **f)** AuNPs/PLC/GSPE

For both PLA and PLC pathways, the peak currents increased significantly compared to the bare electrode, signalling an enhancement in electron transfer kinetics. The linear relationship between peak current the square root of the scan rate for all platforms confirmed that the process remained diffusion-controlled, validating the use of the Randles-Sevcik equation for calculating the electroactive surface area (**Figure 4.3-8).**

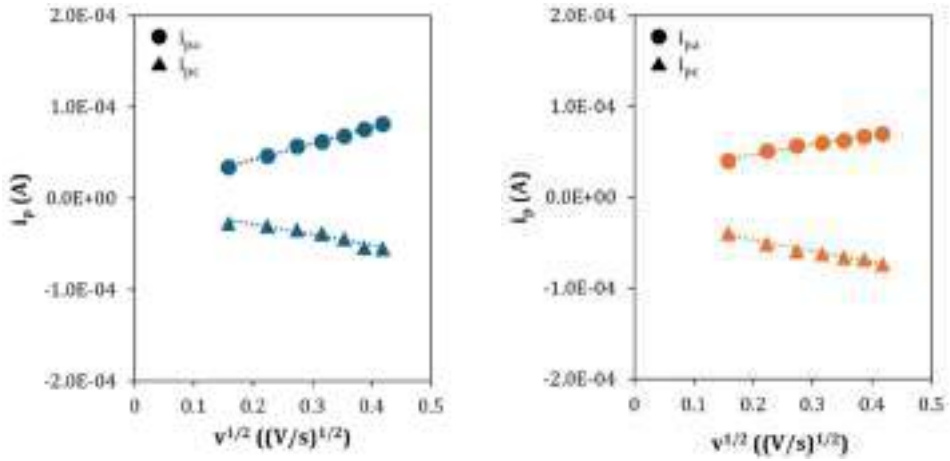

a) **b)**

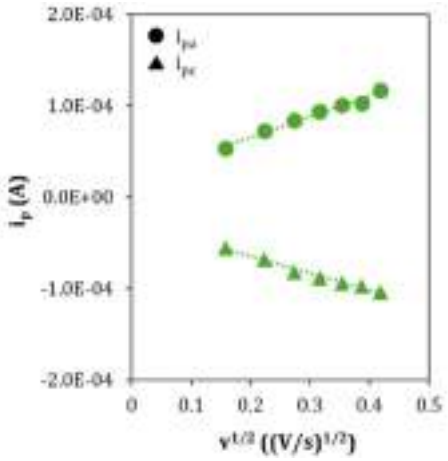

c)

Figure 4.3-8 Linear regressions obtained by plotting the anodic (*ipa*) and cathodic (*ipc*) current peak heights *vs.* the square root of the scan rate ($v^{1/2}$) for **a)** bare GSPE, **b)** PLA/GSPE and c) AuNPs/PLA/GSPE.

The calculated areas, consolidated in **Table 4.3.8-II**, revealed a fundamental difference between the two polymeric underlays. The PLC film substantially increased the electroactive are to 8.3±0.1 mm^2, suggesting the formation of a rough, porous, and highly accessible interface. In stark contrast, the PLA film reduced the apparent area to 3.1±0.1 mm^2. This suppression is attributed to electrostatic repulsion between the anodic redox probe and the negatively charged carboxylate groups of the PLA backbone, which hinders the probe's access to the electrode surface. The subsequent deposition of AuNPs mitigated these effects differently: the AuNPs/PLC platform maintained a large, conductive area of 7.6±0.4 mm^2, while the AuNPs/PLA platform showed a partial recovery to 5.5±0.3 mm^2, as the metallic nanostructures provided new, unhinderevavand electron transfer pathways.

Table 4.3.8-II Electroactive-area values of poly-amino acid based structures and gold nanoparticles (GSPEs, PLC/GSPE, PLA/GSPE, AuNPs/PLC/GSPE, AuNPs/PLA/GSPE), resulting from the cyclic voltammograms performed in $[Fe(CN)_6]^{3-/4-}$ redox marker.

Platform	A_{anodic} (mm^2)	$A_{cathodic}$ (mm^2)	$\bar{A}$ (mm^2)	RSD%
GSPE	4.4	3.8	4.1	9.8
PLC/GSPE	8.3	8.4	8.3	0.9
PLA/GSPE	2.9	3.3	3.1	2.7
AuNPs/PLC/GSPE	7.9	7.3	7.6	5.5
AuNPs/PLA/GSPE	6.2	4.9	5.5	4.5

To move beyond a surface area assessment and prove the intrinsic kinetic facility of each interface, EIS has been employed. By measuring the charge transfer resistance (R_{ct}) across a range of $[Fe(CN)_6]^{3-/4-}$ concentrations, the apparent standard electron transfer rate constant ($k°$) could be derived. The trends in $k°$ were illuminating.

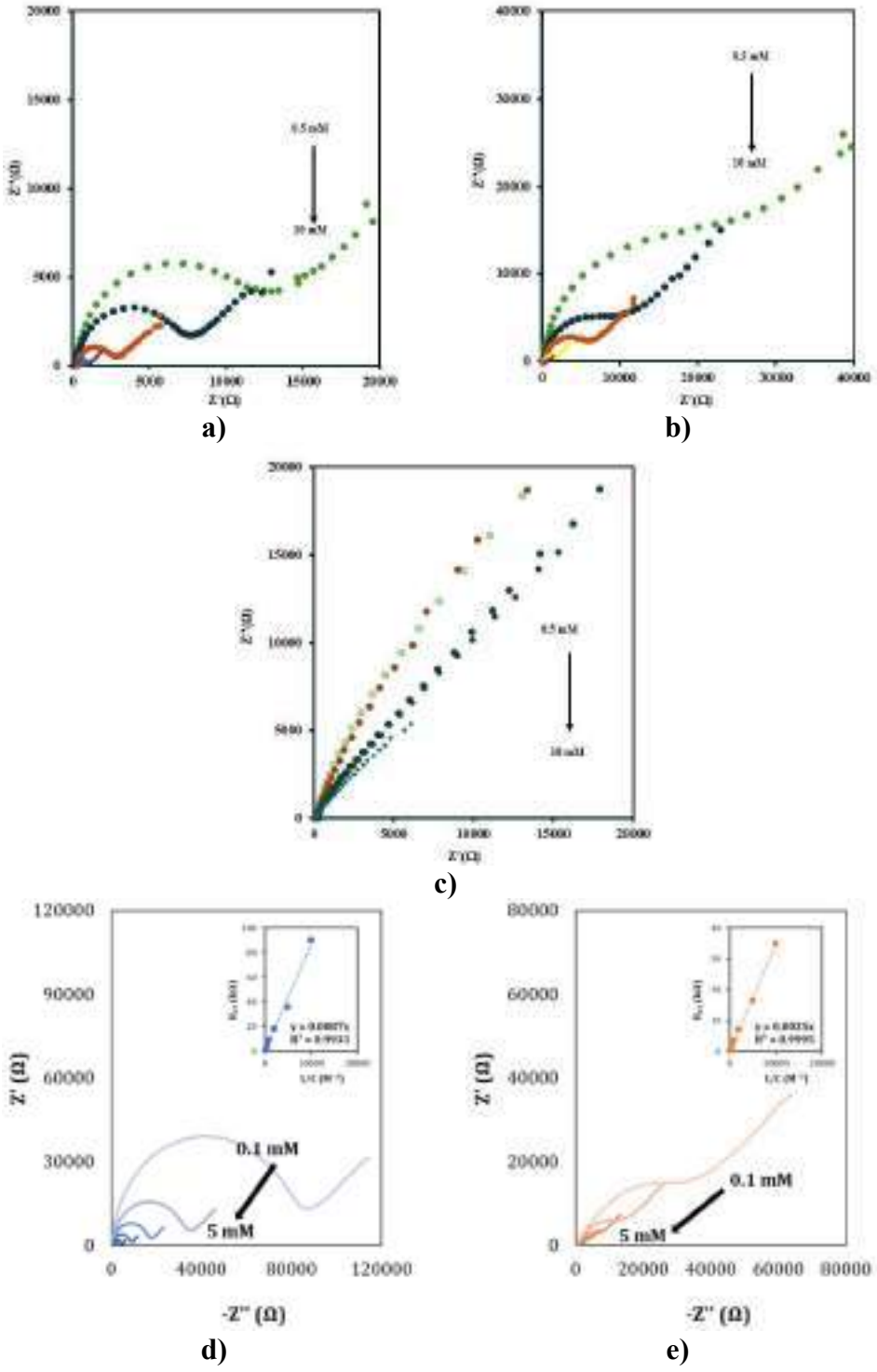

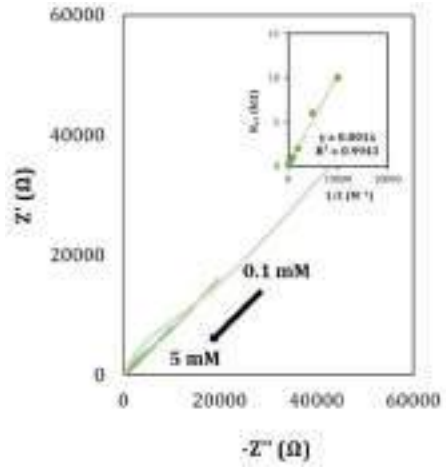

f)

Figure 4.3-9 Nyquist plots obtained in the frequency range of 10^{-5}-0.1 Hz using $[Fe(CN)_6]^{3-/4-}$ redox marker concentrations from 0.5 mM to 10 mM on **a)** GSPE, **b)** PLC/GSPE, **c)** AuNPs/PLC/GSPE, **d)** GSPE, **e)** PLA/GSPE **f)** AuNPs/PLA/GSPE.

For PLA series, k^0 increased stepwise form the bare electrode ($6.72 \cdot 10^{-4}$ cm/s) to the polymer-modified ($2.44 \cdot 10^{-3}$ cm/s) and finally the nanocomposite ($4.13 \cdot 10^{-3}$ cm/s), confirming a progressive improvement in charge transfer. The PLC series followed a similar trajectory, with a significant increase form the bare GSPE to PLC/GSPE. The most compelling evidence, however, came from the fully assembled AuNPs/PLC/GSPE platform. Indeed, its Nyquist plots exhibited a dramatically diminished semicircular region, indicating a near-negligible charge transfer resistance. In fact, the electron transfer was so facile that it approached reversible behaviour, precluding the accurate quantification of $k°$ by this method- a finding that itself underscores the exceptional conductivity of this specific nanocomposite. This contrasts with the AuNPs/PLA/GSPE, which, while improved, still presented a measurable kinetic barrier.

In summary, this electrochemical profiling paints a clear picture. Both platforms enhance conductivity, but they do so through different mechanisms. The AuNPs/PLC/GSPE platform creates a highly accessible and kinetically superior interface, characterised by a large electroactive area and exceptionally fast electron transfer. The AuNPs/PLC/GSPE platform, though effective, must first overcome the inhibitory effect of its own polymeric layer, resulting in a less efficient overall architecture. This fundamental divergence in interfacial properties directly informs their subsequent suitability as sensing matrices, guiding the evaluation of their analytical performance for dopamine detection that follows.

4.3.8.3 DOPAMINE DETECTION IN BUFFER SOLUTIONS

Following the electrochemical profiling, the analytical performance of both nanocomposite platforms was evaluated for the detection of dopamine (DA) under optimised conditions. Using differential pulse voltammetry (DPV) in a drop configuration, both the AuNPs/PLA/GSPE and AuNPs/PLC/GSPE sensors exhibited a concentration-dependent response across the physiologically relevant range of 0-50 µM DA, as shown in **Figure 4.3-10.**

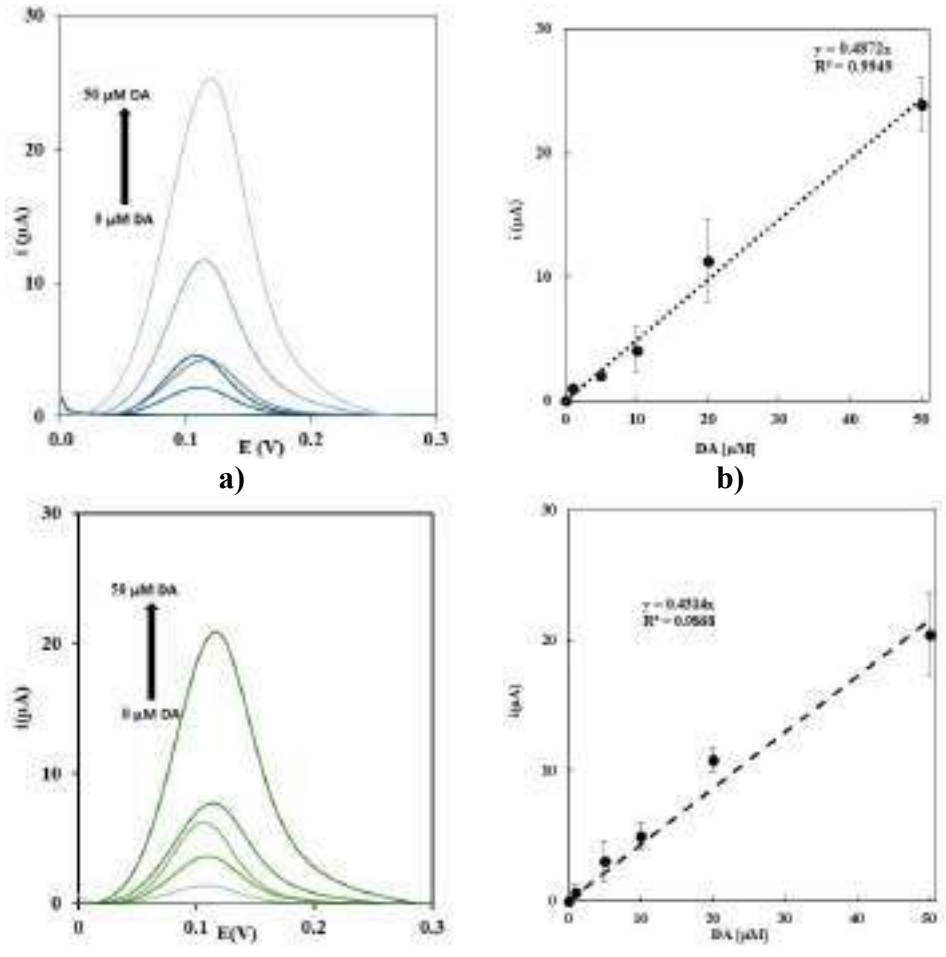

Figure 4.3-10 DPV detection of dopamine (0-50 µM) in PBS (pH 5.5) on **a)** AuNPs/PLA/GSPE and **c)** AuNPs/PLC/GSPE performed with differential pulsed voltammetry (DPV) in the dynamic range of 0-50 µM in PBS buffer solution at pH 5.5. Experimental parameters: potential range from +0.005 V to 0.6 V; scan rate of 0.004 Vs^{-1}; step potential 0.002 V, pulse potential 0.05 V, pulse time 0.05 s. **b)** and **d)** resulting calibrations curves obtained repeating the tests at least 5 times.

A direct comparison of the calibration data, however, revealed a decisive difference in sensitivity. The AuNPs/PLC/GSPE platform demonstrated superior performance, achieving a limit of detection (LOD) of 0.063 µM. In contrast, the AuNPs/PLA/GSPE

showed an LOD of 0.31 μM. This nearly five-fold enhancement in sensitivity for the PLC-based sensor is attributed to the conjunction of several favourable factors previously identified: its significantly larger electroactive area, its exceptionally fast electron transfer kinetics, and the distinct chemical nature of the PLC film. The thiol group in the PLC backbone may promote a more homogenous and stable integration with the gold nanoparticles, potentially creating a more organised and catalytically efficient interface for dopamine oxidation.

Based on this marked advantage in analytical sensitivity, AuNPs/PLC/GSPE platform has been selected as the superior candidate for all subsequent studies.

4.3.8.4 SELECTIVITY ASSESSMENT

The practical application of a sensor in complex biofluids necessitates a rigorous evaluation of its selectivity. Therefore, the response of the AuNPs/PLC/GSPE platform to dopamine (DA) has been investigated in the presence of common physiological interferents found in sweat: lactic acid (LA), glucose (GLU), uric acid (UA), and ascorbic acid (AA). These species can undergo oxidation within a similar potential window to DA, posing a risk of signal overlap and inaccurate quantification in real samples.

To access this critically, the DA oxidation signal (50 μM) was measured in the presence of each interferent at a concentration three times higher (150 μM). The resulting peak current ratios (I/I_0) are reported in **Table 4.3.8-III**

Table 4.3.8-III Selectivity of the AuNPs/PLC/GSPE sensor. Dopamine signal (I) in the presence of interferents relative to the signal for DA alone (I_0).

Interfering species	Relative Dopamine Peak (I/I_0 %)
Uric Acid	77± 25
Ascorbic Acid	120 ± 5
Lactic Acid	104 ± 10
Glucose	98 ± 12

Importantly, the sensor's response to DA remained largely stable, with most interferents causing a signal perturbation of less than 10%. The more pronounced effects observed for AA (signal enhancement of 20%) and UA (signal suppression of 23%) are attributed

to specific interaction that modify the dopamine oxidation signal, and visualised in the voltammograms of **Figure 4.3-11.** These interactions likely involve competitive adsorption or co-oxidation processes at the electrode interface.

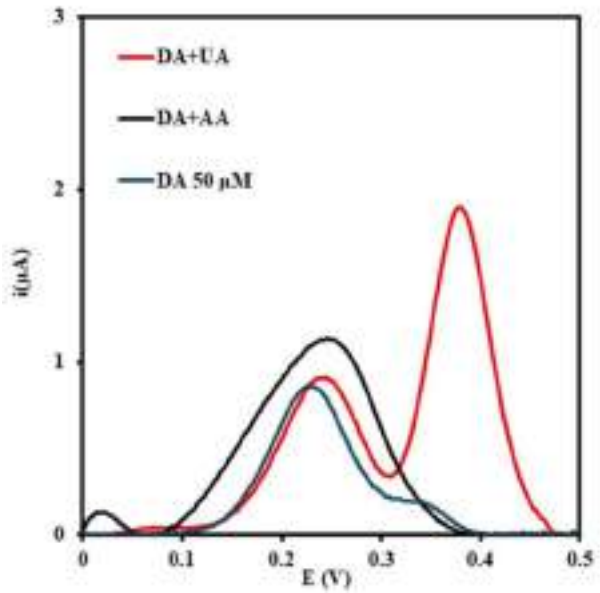

Figure 4.3-11 DPV response for 50 µM dopamine in PBS (pH 5.5) at the AuNPs/PLC/GSPE sensor, demonstrating selectivity against 150 µM uric acid (UA, red) and 150 µM ascorbic acid (AA, black). Parameters: potential range comprised between +0.005 V and 0.5 V; scan rate of 0.004 Vs^{-1}; step potential 0.002 V, pulse potential 0.05 V, pulse time 0.05 s.

Despite these specific interactions with AA and UA, the sensor's core functionality is preserved. The dopamine oxidation peak remains well-defined and readily quantifiable, and the observed signal modifications are predictable and well within manageable limits. This performance profile, demonstrating robust discrimination against key physiological interferents, confirms the significant potential of the AuNPs/PLC/GSPE platform for reliable dopamine sensing in complex media such as sweat.

4.3.8.5 Real Sample Analysis: Artificial Sweat Sample

To validate the practical applicability of the optimised AuNPs/PLC/GSPE platform, its performance has been evaluated in the target matrix: undiluted artificial sweat. Dopamine was spiked into the synthetic sweat at concentrations ranging from 0 to 50 µM and analysed using DPV under the same parameters established for the buffer studies.

As shown in **Figure 4.3-12**, the platform maintained a well-defined concentration-dependent response in this complex and challenging medium. A linear calibration has been obtained (y= 0.112x; R^2 = 0.98), with a calculated LOD of 0.5 µM.

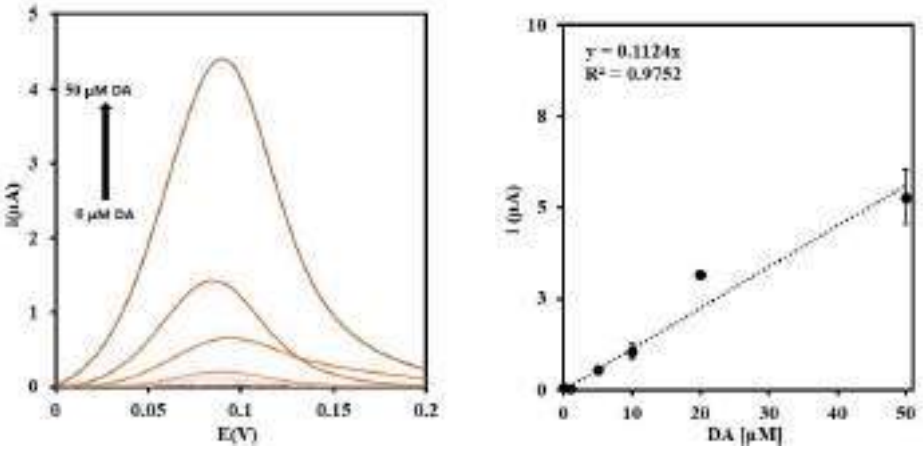

a) **b)**

Figure 4.3-12 DPV detection of dopamine (0-50 µM) in undiluted artificial sweat (pH 5.5) on AuNPs/PLA/GSPE. a) Representative DPV curves. b) the resulting calibration curves (n≥5).

While this LOD is approximately eight times higher than that achieved in pristine buffer (0.063 µM), this is an expected and common effect when transitioning from simple standards to a saline, multicomponent matrix-like sweat. This increase in the LOD (from 0.063 µM to 0.5 µM) ca be interpretated as a result of the 'matrix effect' inherent to complex biofluids. The high ionic strength of undiluted artificial sweat, primarily due to chloride and bicarbonate ions, can partially screen the surface chage of the AuNPs, slightly reducing the effective collision frequency between dopamine and the catalytic sites. Furthermore, the non-specific adsorption of urea or other organic components present in synthetic matrix onto the PLC layer may occupy a fraction of the available active sites, leading to the observed decrease in sensitivity. Nevertheless, the preservation of a linear response with a high correlation coefficient (R^2=0.98) confirms that the PLC/AuNPs interference is remarkably resilient to fouling. Crucially, this sensitivity remains fully sufficient to monitor the physiologically relevant concentrations ranges of dopamine targeted for neurological disorder management. This successful demonstration in a clinically relevant biofluid represents a critical and mandatory step toward the sensor's ultimate application in non-invasive, continuous monitoring.

4.3.9 Conclusions

This chapter has detailed the development and comprehensive characterisation of biocompatible electrochemical sensor for dopamine, designed specifically for the integration into wearable neurological health monitors. The platform was constructed by functionalising graphite screen-printed electrodes (GSPEs) with a poly-L-Cysteine (PLC) film and electrodeposited gold nanoparticles.

Electrochemical and morphological characterisation confirmed that the AuNPs/PLC/GSPE nanocomposite provided a superior interface, combining a large electroactive surface area with exceptionally fast electron transfer kinetics. This translated into excellent analytical performance for dopamine detection in buffer, with a wide linear range (0-50 μM) and a low detection limit of 0.063 μM. The platform also demonstrated robust selectivity against key physiological interferents found in sweat.

Most significantly, the sensor retained its core functionality when validated in undiluted artificial sweat, achieving a clinically relevant detection limit of 0.5 μM within the same dynamic range. This confirms the practical viability of the sensing strategy in a complex realistic matrix.

In summary, this work establishes a persuasive paradigm for fabricating high-performance wearable sensors by replacing conventional, potentially hazardous materials with sustainable, amino acids-based alternatives. The AuNPs/PLC/GSPE platform effectively balances the critical requirements of biocompatibility, sensitivity, and real-world functionality. The strategic use of L-Cysteine proved to be the turning point of this architecture; the amino acid does not simply act as a biocompatible ‘glue’ for gold nanoparticles but actively participates in the sensing mechanism by creating a favourable microenviroment for dopamine oxidation. This demonstrates that the integration of molecular biology-inspired materials with traditional electrochemistry can effectively bypass the trade-off between sensor safety and analytical power.

Future work will focus on integrating this sensing element with a passive sweat sampling system to advance the technology toward a fully operational, user-friendly wearable device for personalised management of Parkinson’s disease and related neurological conditions.

4.4 ACKNOWLEDGMENT

This work was developed in collaboration with Dr. Neri Fuochi, Dr Daniele Martella, Prof. Camilla Parmeggiani, Prof. Ilaria Palchetti, Dr Giulia Selvolini, Dr Sara Failli, Prof. Cristina Truzzi and Prof. Giovanna Marrazza, whose support is gratefully acknowledged.

Note on Publications: The research detailed in this chapter has led to the following peer-reviewed publications, in which the author of this thesis is a contributing co-author:

1. I. A. Vitale, N. Fuochi, D. Martella, C. Parmeggiani, G. Marrazza, and I. Palchetti, "Skin-contact wearable electrochemical biosensing tools: A perspective for the wellbeing of neurological patients," TrAC Trends in Analytical Chemistry, vol. 180, p. 117965, Nov. 2024, doi:10.1016/j.trac.2024.117965.
2. I. A. Vitale, G. Selvolini, S. Failli, C. Truzzi, G. Marrazza, Mercury Detection in Novel Foods by a Smart Pocket Sensor, Electroanalysis 2024, 36, e202400192. https://doi.org/10.1002/elan.202400192
3. I. A. Vitale, I. Palchetti, G. Marrazza, Amino Acid-Based Electrochemical Sensor for Monitoring Dopamine in Sweat, Brazilian Journal of Chemistry, 2025, electrochemicalActa

This publication was produced with the co-funding of the European Union - Next Generation EU, in the context of The National Recovery and Resilience Plan, Investment 1.5 Ecosystems of Innovation, Project Tuscany Health Ecosystem (THE), ECS00000017, Spoke 3, CUP: B83C22003920001. The authors acknowledge MIUR for "Progetto Dipartimenti di Eccellenza 2023–2027" allocated to the Department of Chemistry "Ugo Schiff" of the University of Florence.

5. Wearable Therapeutic Drug Monitoring: A Sweat-Based Sensor for Levodopa in Parkison's Disease Management

5.1 Therapeutic Drug Monitoring in Neurological Disorders

The paradigm for personalized medicine seeks to optimize therapeutic outcomes by tailoring treatment regimens to the individual patient, a principle often summarized as administrating "the right drug at the right dose" [211]. This approach is particularly critical in the management of neurological disorders, where pharmacotherapy is a cornerstone of care and the precise evaluation of a drug's efficacy and safety profile is paramount [212].

Levodopa (L-DOPA) serves as a prime example of this clinical challenge. As a cornerstone treatment for Parkinson's diseases (PD) since the 1960s, it is highly effective in alleviating motor symptoms. However, its administration is complicated by a narrow therapeutic window, with excessive intake leading to significant side effects, including gastrointestinal and cardiovascular complications as well as dyskinetic movements [213–215]. This precarious balance makes the continuous monitoring of drug pharmacokinetics a crucial aspect of patient management [216].

The search for a viable monitoring strategy has turned toward non-invasive biofluids. Indeed, foundational work by Tsunoda et al. [217] demonstrated a strong correlation between levodopa concentrations in blood and sweat using HPLC analysis of human samples, thereby establishing the rationale for sweat-based monitoring. Building on this premise, several studies have since explored the development of electrochemical sensors for levodopa detection in various matrices, including serum, plasma, and sweat, charting a clear technological path toward wearable therapeutic drug monitoring [218,219].

This body of work collectively underscores the significant potential of sweat as a diagnostic medium for pharmacokinetic monitoring. However, to translate this potential into a practical tool for personalised drug intake in the context of neurological disorders, there remains a critical need to develop robust, wearable sensing platforms that can perform accurate, on-body quantification of levodopa in undiluted sweat. This chapter

address that needs by presenting an integrated sensing system that combines an electrochemical sensor for levodopa coupled with a PDMS-based microfluidic module enabling of sampling sweat and handling it. This work moves beyond foundational correlation studies toward the realisation of a functional, integrated device for continuous therapeutic drug monitoring.

5.2 Plasma-Treated Carbon Sensor coupled to PDMS-based Microfluidic platform for the Determination of Levodopa in Sweat

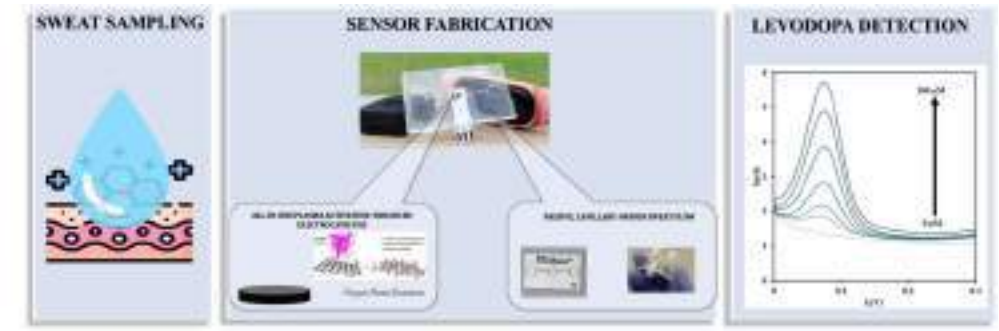

Figure 5.2-1. Graphical abstract. Integrated microfluidic-electrochemical platform for Levodopa monitoring. The sensing infrastructure utilizes a synergistic oxygen plasma treatment (all-in-one approach) to simultaneously activate the electrode surface for enhanced electroanalysis and render the PDMS microchannels hydrophilic. This allows for autonomous, passive sweat sampling and real-time therapeutic drug monitoring of Levodopa.

5.2.1 State of Art

The optimisation of therapeutic outcomes in neurological disorders fundamentally depends on the accurate monitoring of drug levels. This is particularly evident in the management of Parkinson's disease (PD), where levodopa (L-DA) serves as the cornerstone pharmacological intervention. The pursuit of long-term therapeutic success in the context hinges on the precise evaluation of a drug's pharmacokinetics, efficacy, and safety profile. Levodopa exemplifies this principle, having been the gold-standard treatment since its introduction in the 1960s [212]. As a precursor to dopamine, the neurotransmitter critically depleted in PD, L-DA administration effectively mitigates motor symptoms and supports normative motor function. However, its clinically utility is constrained by a characteristically short half-life and a therapeutic window that narrows progressively with long-term use, presenting a formidable clinical challenge. These pharmacokinetic limitations often precipitate motor and non-motor fluctuations, creating

a complex management landscape where current clinical protocols predominantly rely on subjective patient reporting, underscore a pressing need for objective, real-time, and non-invasive monitoring tools [220].

This gap between clinical need and available monitoring methods has galvanised the development of electrochemical sensing strategies, primarily through enzymatic and nanomaterial-based approaches. The work presented herein introduces a novel contribution to this evolving landscape: the first microfluidic platform integrated with a plasma-activated carbon sensor designed for the detection of L-DA in sweat. This integrated device represents a substantive step toward a practical PoC for personalised therapeutic drug monitoring in PD, moving beyond the limitations of current paradigms toward objective, real-time, and non-invasive monitoring.

Significant progress has been made in biosensing technologies aimed at PoC drug monitoring, with a dual focus on creating accurate, user-friendly devices and validating the use of peripheral biofluids for pharmacokinetic analysis. The foundational demonstration of a strong correlation between L-DA concentrations in blood and sweat established the physiological rational for sweat-based monitoring [217]. This finding catalysed research into electrochemical sensors for L-DA detection in biological matrices such as sweat, serum and plasma. Subsequent innovations include an enzyme-modified fingertip sensor for continuous monitoring using screen-printed electrodes [221], and a composite sensor employing tyrosinase-ZIF-8 on graphene oxide, which achieved a limit of detection of 0.45 μM [222]. Time-resolved studies further confirmed the feasibility of this approach, showing detectable electrochemical changes in sweat as early as 45 minutes post L-DA ingestion. Another notable advancement has been reported by. Glasco et al. [223], where in their study a smartphone-integrated, 3D-printed electrochemical sensor fabricated from polylactic acid films and conductive inks has been employed, which demonstrated direct, non-enzymatic detection of L-DA and uric acid with a limit of detection of 30 nM and excellent recovery in real sample validation.

While the electrochemical detection of L-DA in peripheral biofluids remains an active research frontier [219,220], the predominant sensor architectures rely on metallic nanoclusters or modified carbon-based materials to facilitate the oxidation of L-DA. Despite their analytical performance, such modifications may be less suitable for continuous, skin-contact wearable devices due to concerns regarding potential

cytotoxicity and the high costs associated with nanomaterial synthesis and integration [224,225]. Beyond the sensing element itself, a critical design challenge for any wearable sweat analyser is the efficient and consistent acquisition of the biofluid directly from the skin surface, guiding it to the sensing interface without the need for external collection or manual handling. In this domain, a multitude of patches fabricated from biocompatible materials have been proposed [226]. Among these, polydimethylsiloxane (PDMS) has emerged as a particularly optimal substrate for constructing flexible microfluidic patches, owing to its exceptional biocompatibility, resistance to biodegradation, and high chemical stability, properties essential for durable, skin-contact healthcare device. [227,228].

However, the intrinsic and extreme hydrophobicity of PDMS presents a significant obstacle, as it can impede the flow of hydrophilic analytes like sweat or promote the adsorption of hydrophobic compounds, thereby skewing analytical results or preventing measurements entirely. To overcome this inherent limitation, the surface chemistry of PDMS microfluidic channels must be modified to achieve the necessary hydrophilicity. This can be accomplished through either chemical or physical surface treatments [229,230]. Among these methods, oxygen plasma treatment stands out as a gold-standard, single-step process [230]. It works by introducing silanol groups (SiOH) onto the polymer surface, thereby permanently converting it to a hydrophilic state without the requirement for chemical reagents or multi-step procedures, which simplifies fabrication and enhances device reliability.

Integrating these considerations, the need for a non-toxic, cost-effective sensing interface and a robust, hydrophilic microfluidic sample handling system, this chapter describes the development and characterisation of a fully integrated platform. It combines a PDMS-based microfluidic patch, rendered hydrophilic via oxygen plasma treatment, with an electrochemical sensor fabricated from plasma-activated carbon materials. To the best of our knowledge, this represents the first report of a microfluidic-integrated carbon sensor, activated solely by plasma treatment without nanomaterials or bioreceptors, for the determination of levodopa in sweat.

5.2.2 Chemicals

Dopamine hydrochloride ($C_8H_{11}NO_2 \cdot 2H_2O$), 3,4-Dihydroxy-L-phenylalanine (Levodopa- $(HO)_2C_6H_3CH_2CH(NH_2)CO_2H$) disodium hydrogen phosphate (Na_2HPO_4),

potassium dihydrogen phosphate (KH_2PO_4), sodium chloride (NaCl), potassium chloride (KCl), potassium ferrocyanide ($K_4[Fe(CN)_6]$), potassium ferricyanide ($K_3[Fe(CN)_6]$]), sodium sulphate (Na_2SO_2), sodium fluoride (NaF), cadmium chloride ($CdCl_2$), Copper (II) chloride dihydrate ($CuCl_2 \cdot 2H_2O$), iron sulphate heptahydrate ($FeSO_4 \cdot 7H_2O$), lead (Pb) reference solution 1000 ppm, Nickel (Ni) reference solution 1000 ppm, sodium bicarbonate ($NaHCO_3$), Zinc (Zn) reference solution 1000 ppm, Magnesium chloride hexahydrate ($MgCl_2 \cdot 6H_2O$), sodium phosphate anhydrous monobasic (NaH_2PO_4); lactic acid ($CH_3CH(OH)COOH$), acetic acid ($C_2H_4O_2$); D(+)-glucose ($C_6H_{12}O_6$), L-alanine ($C_3H_7NO_2$), L-aspartic acid ($C_4H_7NO_4$), L-glutamic acid ($C_5H_9NO_4$), L-leucine ($C_6H_{13}NO_2$), L-lysine monohydrochloride ($C_3H_7NO_2$), L-tryptophan ($C_{11}H_{12}N_2O_2$), L-tyrosine ($C_9H_{12}NO_3$); ammonium hydroxide 28-30% solution (NH_4OH), uric acid ($C_5H_4N_4O_3$), urea (CH_4N_2O), creatinine ($C_6H_7N_3O$), creatine monohydrate ($C_4H_9N_3O_2 \cdot H_2O$), L-ascorbic acid ($C_6H_8O_6$), polyvinyl alcohol (PVA) (Mw 89.000) were purchased from Merck (Milan, Italy).

Milli-Q water was always used. The phosphate-buffer saline (PBS) composition was 137 mM NaCl, 2.7 mM KCl, 10 mM Na_2HPO_4, 1.8 mM KH_2PO_4 dissolved in Milli-Q water and the pH adjusted to 5.5. The negative moulds were realized by photopolymerization of an UV-curable photopolymer, grey Tough Resin 2.0 (Anycubic, China). The PDMS layers were prepared by using Sylgard TM 184 Silicone Elastomer Kit, with a 10:1 w/w ratio between the PDMS liquid precursor and its curing agent, was bought from Cecchi s.r.l and used as received.

5.2.3 Apparatus

The measurements were performed with carbon screen-printed electrochemical Sensors (CSPES) composed of a carbon working electrode (3 mm diameter), a silver pseudo-reference electrode and a carbon counter electrode. The CSPES were purchased from EcoBioServices (Florence, Italy). All the potentials are referred to the silver pseudo-reference electrode, and all the measurements have been performed at room temperature. The PalmSens Electrochemical Analyser and the Sensit potentiostat (PalmSens, the Netherlands) were used for the electrochemical optimization experiments and for the microfluidic measurements, respectively; the results were analysed by PSTrace 5.6 software.

5.2.4 Microfluidic Network Preparation and Characterisation

The fabrication of the integrated sensing platform began with the preparation of its core structural components: two distinct PDMS layers designed to host the microfluidic network and the electrode, respectively. To achieve this, custom polymeric negative moulds were first fabricated via 3D printing, based on the designed illustrated in **Figure 5.2-3.** The moulds for the microfluidic layer were engineered to produce a network featuring a single inlet and outlet, each with a radius of 2.5 mm. These ports are connected to a central accumulating chamber (8 mm ×5 mm × 1 mm) via microfluidic channels measuring 0.5 mm in width and 10 mm in length. A key design feature is the sloping channel height, which transitions from 1 mm to 0.5 mm; this gradient was intentionally incorporated to facilitate passive fluid flow both from the inlet to the accumulating chamber and from the chamber toward the outlet. The inclusion of the accumulating chamber itself serves a dual purpose: it ensures controlled fluid collection and distribution within the device and promotes the analyte concentration at the sensing interface, thereby enhancing signal response. The second mould, designed as a support for the screen-printed carbon electrode (CSPE), was a simple parallelepiped with dimensions of 20 mm × 5.5 mm × 0.250 mm.

The 3D model was sliced using Anycubic Photon Workshop software with a layer thickness set to 100 μm and subsequently printed using an Anycubic Mono M5s Pro 3D printer with a grey Tough Resin 2.0 as the UV-curable photopolymer. Post-printing, the moulds underwent a critical cleaning and curing protocol. Residual resin was removed using diisopropanol, followed by a 10-minute cure under a 385 nm LED lamp. To ensure complete polymerization and remove any residual plasticizers or unreacted monomers that could inhibit the subsequent curing of PDMS, the moulds then underwent an annealing procedure at 60°C for 48 hours (**Figure 5.2-3b**).

With the moulds prepared, the PDMS precursor and its curing agent were mixed in a 10:1 weight ratio. The mixture was degassed under vacuum to eliminate air bubbles, carefully poured into the moulds, and degassed a final time to ensure a defect-free replica. Curing was carried out at 60°C for 3 hours. Once cooled to room temperature, the solid PDMS replicas were delicately peeled from the moulds. The obtained layers were then mechanically modified: holes were pierced at the designated inlet and outlet positions, and the layers were trimmed to better accommodate the electrode wires, as depicted in **Figure 5.2-3c**.

A pivotal step for enabling passive capillary-driven flow was the surface modification of both the PDMS layers and the electrode. Prior to final device assembly, all components were subjected to a plasma treatment to render their surfaces hydrophilic. The final assembly involved aligning the two activated PDMS layers, first inserting the electrode into its dedicated hosting area in the support layer. The activated surfaces were then brought into conformal contact, where the formation of irreversible siloxane bonds at the interface ensured a robust and leak-free seal, completing the integrated microfluidic sensing platform.

5.2.5 Plasma Treatment of the Carbon Sensor and Electrochemical and Morphological Characterization

Following its investigation into the microfluidic architecture, the carbon working electrode of the CSPE underwent a dedicated plasma treatment to modify its surface properties. The impact of this treatment on the electrochemical performance was rigorously evaluated through a combination of electrochemical and morphological techniques. Cyclic Voltammetry (CV) and Electrochemical Impedance Spectroscopy (EIS) were employed using the inner-sphere redox probe ferri/ferrocyanide, $[Fe(CN)_6]^{3-/4-}$. The electrochemical behaviour of this probe is highly sensitive to the surface chemistry, particularly the presence of oxygen, containing functional groups, and the structure of the electrode material, rather than merely its electronic density states, making it an ideal diagnostic tool for assessing surface modifications induced by plasma [231,232].

For CV analysis, a 50 µL droplet of 5.0 mM equimolar solution of $[Fe(CN)_6]^{3-/4-}$ in 0.1 M KCl was deposited to the planar CSPE. Measurements were conducted at various scan rates (0.025 to 0.150 V/s), with the potential cycled between -1.0 and +1.0 V. The recorded cathodic and anodic peak currents (I_p) served as the primary electrochemical signals. These data were subsequently fitted using the Randles-Ševčík equation to extract key parameters related to the electrode's active area and the kinetics of the electron transfer process.:

$$I_p = 2.686 \cdot 10^5 \cdot z^{3/2} A D^{1/2} C v^{1/2}$$

where z stands for the number of electrons transferred in the redox events, A (cm^2) is the electrode surface area, D (cm^2/s) is the diffusion coefficient of the oxidized analyte and C (mol/cm^3) is the $[Fe(CN)_6]^{3-/4-}$ concentration.

Complementary EIS experiments were performed by applying a sinusoidal voltage perturbation of 10 mV amplitude across a frequency range of 30 kHz to 10 mHz, superimposed on a DC bias potential set at the open-circuit potential (OCP) measured immediately prior to each experiment. The resulting spectra, presented as Nyquist plots, were modelled using appropriate equivalent circuits via dedicated software. The Randles equivalent circuit proved suitable for fitting the acquired data, allowing for the extraction of the charge transfer resistance (R_{ct}) as a direct analytical signal reflecting the ease of electron transfer at the electrode-electrolyte interface [233,234].

To correlate the observed electrochemical changes with physical alterations on the surface, morphological analysis was conducted using a Hitachi FlexSEM 1000 II Scanning Electron Microscope (SEM). Imaging was performed in Backscattered Electron (BSE) mode with a BSE-TOPO configuration to enhance topographical contrast, operated at an accelerating voltage of 10.0 kV, a magnification of 93×, and a working distance of 6.6 mm.

5.2.6 Dopamine and Levodopa Electrochemical Detection

The efficacy of the plasma-treated CSPE for its intended application was evaluated by investigating its electrochemical response towards the target analytes, dopamine (DA) and levodopa (L-DA), in standard solutions. Differential Pulse Voltammetry (DPV) was selected for this purpose due to its high sensitivity and superior resolution for detecting faradaic currents against the capacitive background. The potential was scanned from 0 to 0.5 V using optimized parameters: a scan rate of 0.004 V/s, a step potential of 0.002 V, a pulse potential of 0.05 V, and a pulse time of 0.05 s. The height of the oxidation peak current recorded for each analyte was used as the analytical signal and plotted against the corresponding DA and L-DA concentrations to establish calibration curves and assess sensor performance.

5.2.7 Real Sample Analysis in Microfluidic Chamber

To validate the sensor's performance under conditions mimicking its final application, the analysis of L-DA was conducted within the assembled microfluidic chamber. A comprehensive analytical characterization—encompassing repeatability, stability, and the linear dynamic range—was first established using buffered standard solutions under microfluidic flow conditions. This foundational step ensured the device's reliability before confronting the complexity of a real biological matrix.

For real-sample testing, synthetic human sweat was employed. The sweat formulation was meticulously prepared according to an established recipe, designed to accurately replicate the ionic strength, pH, and chemical composition of human eccrine sweat, including the presence of potentially interfering electroactive species. The complete chemical formulation is detailed in **Table 5.2.7-I** , with the final pH adjusted to 5.2 to reflect typical sweat conditions. This formulation has been adapted by Harvey at al. [235]

Table 5.2.7-I Adapted artificial sweat formulation from **[235]** taking into consideration the presence of electroactive species

Constituent	Mass (g/L)
Sodium sulphate (Na_2SO_4)	5.83×10^{-2}
Sodium fluoride (NaF)	4.62×10^{-4}
Cadmium chloride anhydrous ($CdCl_2$)	3.30×10^{-6}
Copper (II) chloride diidrate ($CuCl_2 \cdot 2H_2O$)	1.60×10^{-4}
Iron solfate heptahydrate ($FeSO_4 \cdot 7H_2O$)	2.72×10^{-3}
Lead (Pb) – reference solution 1000 ppm	2.49×10^{-5}
Zinc (Zn) – reference solution 1000 ppm	8.50×10^{-4}
Nickel (Ni) – reference solution 1000 ppm	2.46×10^{-5}
Sodium bicarbonate ($NaHCO_3$)	2.52×10^{-1}
Potassium chloride (KCl)	4.55×10^{-1}
Magnesium chloride hexahydrate ($MgCl_2 \cdot 6H_2O$)	1.67×10^{-2}
Sodium phosphate anhydrous monobasic (NaH_2PO_4)	4.84×10^{-2}
Sodium chloride (NaCl)	1.55×10^{0}
Lactic acid ($CH_3CH(OH)COOH$)	1.26×10^{0}
Acetic acid ($C_2H_4O_2$)	7.81×10^{-3}
D(+)-Glucose ($C_6H_{12}O_6$)	3.06×10^{-2}
DL-Alanine ($C_3H_7NO_2$)	5.11×10^{-2}
L-(+)-Glutamic acid ($C_5H_9NO_4$)	5.44×10^{-2}
L-(+)-Aspartic acid ($C_4H_7NO_4$)	4.53×10^{-2}
Glycine ($C_2H_5NO_2$)	2.93×10^{-2}
L-Histidine ($C_6H_9N_3O_2$)	8.07×10^{-2}

L-Leucine ($C_6H_{13}NO_2$)	2.75×10^{-2}
L-(+)-Lysine Monohydrochloride ($C_6H_{14}N_2O_2 \cdot HCl$)	2.74×10^{-2}
L-Tyrosine ($C_9H_{11}NO_3$)	3.08×10^{-2}
L-(–)-Tryptophan ($C_{11}H_{12}N_2O_2$)	1.12×10^{-2}
L-Phenylalanine ($C_9H_{11}NO_2$)	2.13×10^{-2}
Uric acid ($C_5H_4N_4O_3$)	9.92×10^{-3}
Urea (CH_4N_2O)	6.01×10^{-1}
Creatinine ($C_4H_7N_3O$)	9.50×10^{-3}
L-(+)-Ascorbic acid ($C_6H_8O_6$)	1.76×10^{-3}
Creatine monohydrate ($C_4H_9N_3O_2 \cdot H_2O$)	2.24×10^{-3}

This complex matrix was then spiked with known concentrations of L-DA and analysed within the PDMS-based microfluidic chamber to evaluate the sensor's selectivity, accuracy, and robustness in a physiologically relevant environment.

5.2.8 Computational Fluid Dynamics (CFD) Simulation

To theoretically model and optimize the fluidic behaviour within the designed PDMS channels, Computational Fluid Dynamics (CFD) simulations were performed using Autodesk software. The simulations applied the fundamental continuity equation and boundary layer theory. Water was defined as the working fluid to simulate sweat, and a constant mass flow rate of 0.05 g/s was imposed between the inlet and outlet to model passive flow conditions. The simulations were conducted under ambient pressure conditions, with PDMS specified as the channel wall material to account for its surface properties in the fluid dynamic model.

5.2.9 Results and Discussion

5.2.9.1 Principle and Design of the PDMS-based Microfluidic Device

The overarching principle guiding the design of the microfluidic system was to achieve simple, passive, and precise handling of sweat samples, thereby eliminating the reliance on external pumps or active components that would compromise the device's wearability and ease of use. To translate this principle into a functional architecture, the essential structural elements of the fluidic network were conceived to ensure straightforward and reproducible fabrication. The initial layout was rigorously optimized through iterative

Computational Fluid Dynamics (CFD) simulations, with particular attention paid to the geometry of the channels connecting the inlet, the accumulation chamber, and the outlet, as these features directly govern flow uniformity and transport efficiency (**Figure 5.2-2**).

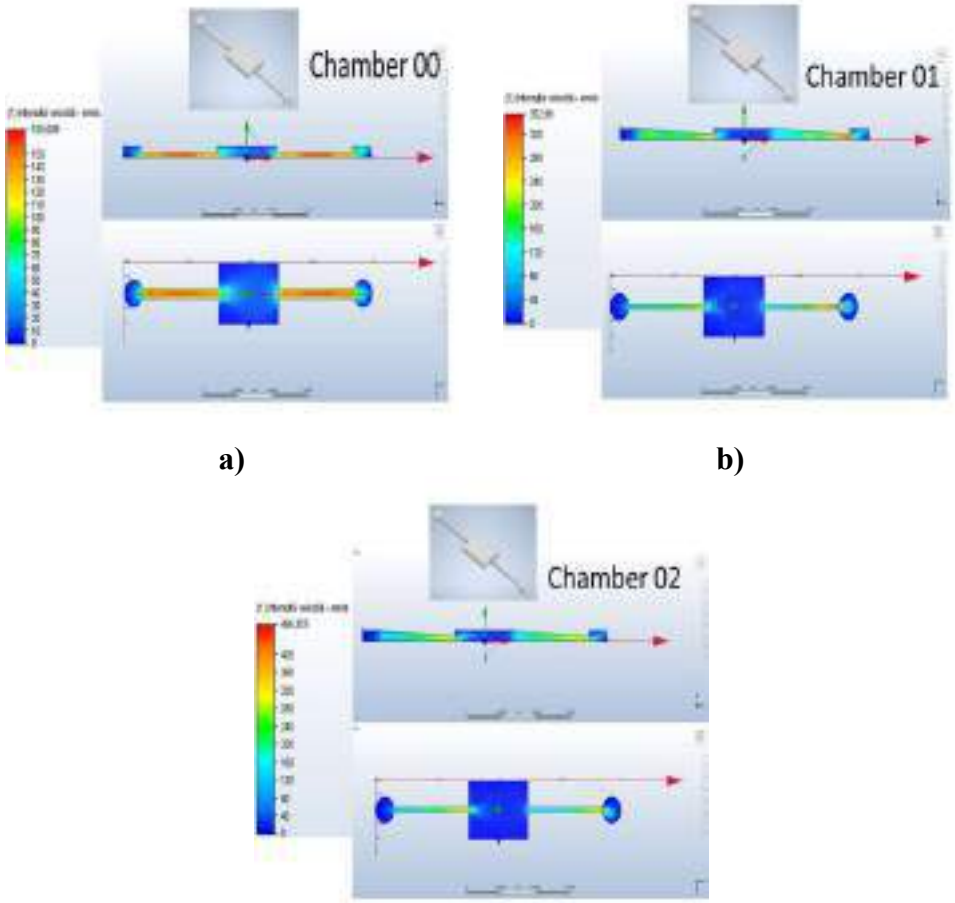

a) **b)**

c)

Figure 5.2-2 Computational Fluid Dynamics (CFD) simulations interface**. a)** chamber 00 (straight, square channels) flow simulations, showing a turbulent flow reaching a maximum speed of 170 mm/s; **b)** chamber 01 (sloping, square channels) flow simulations, showing a uniform flow reaching a maximum speed of 352 mm/s; **c)** chamber 02 (sloping, rounded channels) flow simulations, showing a uniform flow reaching a maximum speed of 466 mm/s.

CFD analysis served as a critical tool for this design evolution. The simulation of the initial design, featuring straight, square channels (chamber 00), revealed a slow and turbulent flow with a maximum speed of170 mm/s . To improve transport efficiency and flow profile, the channel geometry was progressively refined. A second iteration introduced sloped walls (chamber 01), which resulted in a more uniform flow with a significantly higher maximum speed of 352 mm/s. The final optimized configuration incorporated both sloping and rounded channel boundaries (chamber 02). This design

yielded the most favourable hydrodynamic profile, characterized by a uniform, laminar flow reaching a maximum speed of 466 mm/s, thereby ensuring rapid and consistent analyte transport to the sensing zone. The fidelity between this optimized 3D digital design and the physically fabricated microfluidic network was paramount. Verification was achieved through comparative optical imaging and subsequent quantitative analysis using ImageJ software. The fabrication workflow, illustrated in **Figure 5.2-3**, began with the creation of negative molds via 3D printing, based on the digital projects for both the microfluidic network and the electrode hosting area.

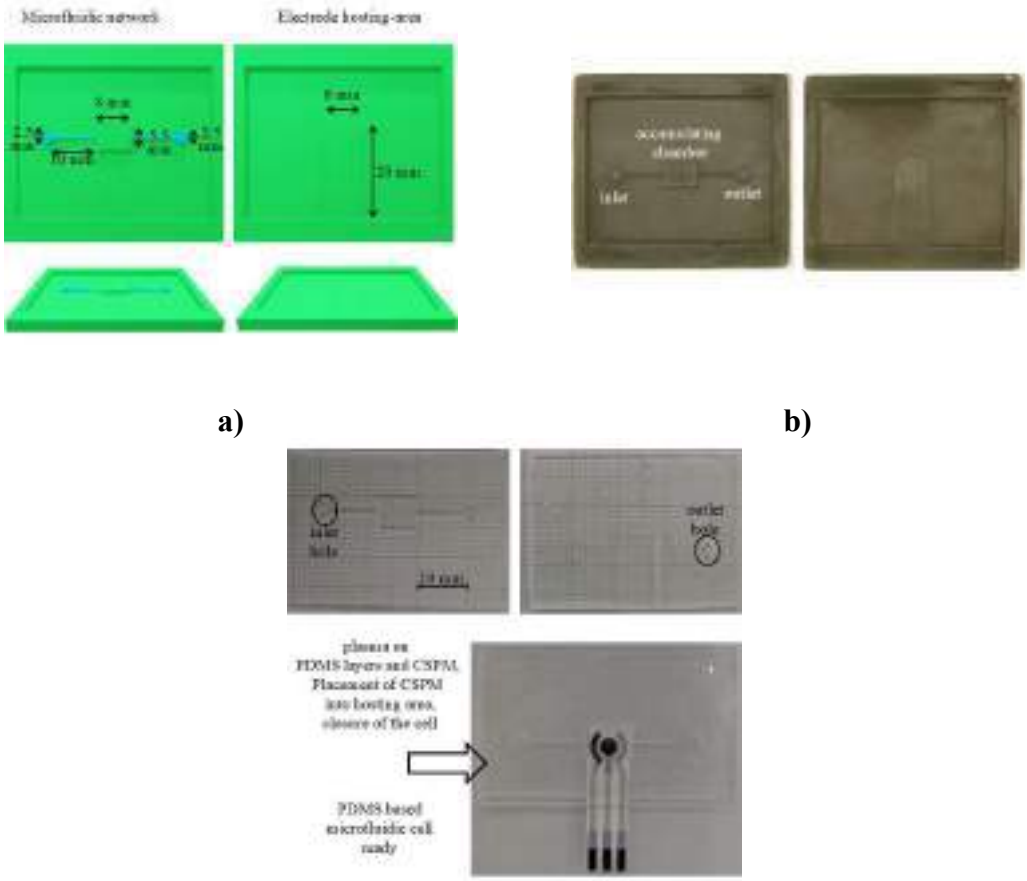

Figure 5.2-3 Production of the microfluidic cell**. a)** Front and side view of the 3D project for the negative mould of the microfluidic network (left) and electrode hosting-area (right); **b)** optical image of the negative moulds after printing; **c)** PDMS layers obtained after the polymerization of the PDMS inside the negative moulds, and final cell obtained after processing the layers and the CSPR with plasma.

After printing and post-processing, PDMS was polymerized within these molds. The resulting PDMS layers were then subjected to oxygen plasma treatment — a step applied concurrently to the carbon sensor surface — to render them hydrophilic. This treatment

was essential to overcome the inherent hydrophobicity of PDMS and to enable spontaneous capillary-driven flow, a cornerstone of the device's passive operation.

The transition from a hydrophobic to a hydrophilic state in PDMS during oxygen plasma treatment is due to the high-energy collision of plasma species with the polymer surface, which breaks the Si-CH_3 bonds and introduces silanol groups (-SiOH). This chemical modification dramatically increases the surface free energy, allowing sweat to overcome the capillary resistive forces. In our optimized *Chamber 02* geometry, the synergy between this increased hydrophilicity and the rounded channel boundaries minimizes the dead zones and ensures that the sample reaches the electrode surface with a uniform velocity profile, as predicted by the CFD simulations.

The structural integrity and connectivity of the microfluidic pathways were further scrutinized at a microscopic level using Scanning Electron Microscopy (SEM). As shown in **Figure 5.2-4**, SEM imaging confirmed the continuous and well-defined nature of the channels, from the inlet opening through the connecting pathway, ensuring no physical barriers to fluid transport existed.

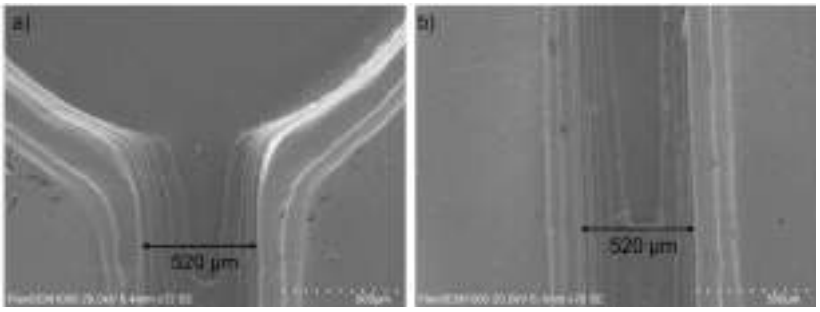

Figure 5.2-4 PDMS channels SEM images. **a)** inlet opening to the connecting channel; **b)** middle-part of the connecting channel.

Prior to final assembly, the PDMS layers were mechanically processed: inlet and outlet ports were pierced, and the layers were trimmed to neatly accommodate the wires of the screen-printed carbon electrode (CSPE). Assembly involved inserting the CSPE into its dedicated cavity and aligning the two activated PDMS layers. Conformal contact under gentle pressure allowed spontaneous bonding via siloxane bond formation, creating a sealed, leak-proof device. The operational principle of passive capillary flow was then conclusively demonstrated by introducing 50 µL of a 15 µM methylene blue solution at the inlet. The solution immediately and autonomously wicked through the entire network, filling the accumulating chamber and progressing to the outlet without any external actuation (**Figure 5.2-5).**



Figure 5.2-5 demonstration of passive flow into the microfluidic cell. When 50 µL of a methylene blue water solution are added to the inlet channel, they immediately flow to the accumulating chamber (left panel). The methylene blue solution passively reaches the outlet channel and flows out from it.

This experiment visually validated the successful integration of the hydrophilic surface modification and the optimized channel geometry. The resulting PDMS devices exhibited robust structural integrity and were thus primed for subsequent integration with the sensor and evaluation with sweat samples.

5.2.9.2 Electrochemical Characterisation of Plasma-Treated CSPE

As the screen-printed carbon electrode (CSPE) is subjected to oxygen plasma activation during the assembly of the microfluidic device — a step primarily intended to hydrophilize the PDMS — a critical investigation was undertaken to understand the concomitant effects of this treatment on the electrochemical properties of the carbon surface itself. Preliminary experiments were therefore devoted to characterizing these effects, employing cyclic voltammetry (CV) with the inner-sphere redox probe ferri/ferrocyanide, $([Fe(CN)_6])^{3-/4-}$.The voltametric behaviour of this probe is acutely sensitive to the surface chemistry and microstructure of the electrode, providing a diagnostic tool for assessing changes in electron transfer kinetics and electroactive area. The enhancement conferred by plasma treatment is immediately evident in the cyclic voltammograms. As shown in **Figure 5.2-6 ,** the plasma-treated CSPE exhibits a pronounced reduction in the peak-to-peak potential separation (ΔEp) to 0.175 V, which is 71% lower than the ΔEp of 0.246 V observed for the bare electrode. This narrowing is a classic indicator of significantly improved electron transfer kinetics.

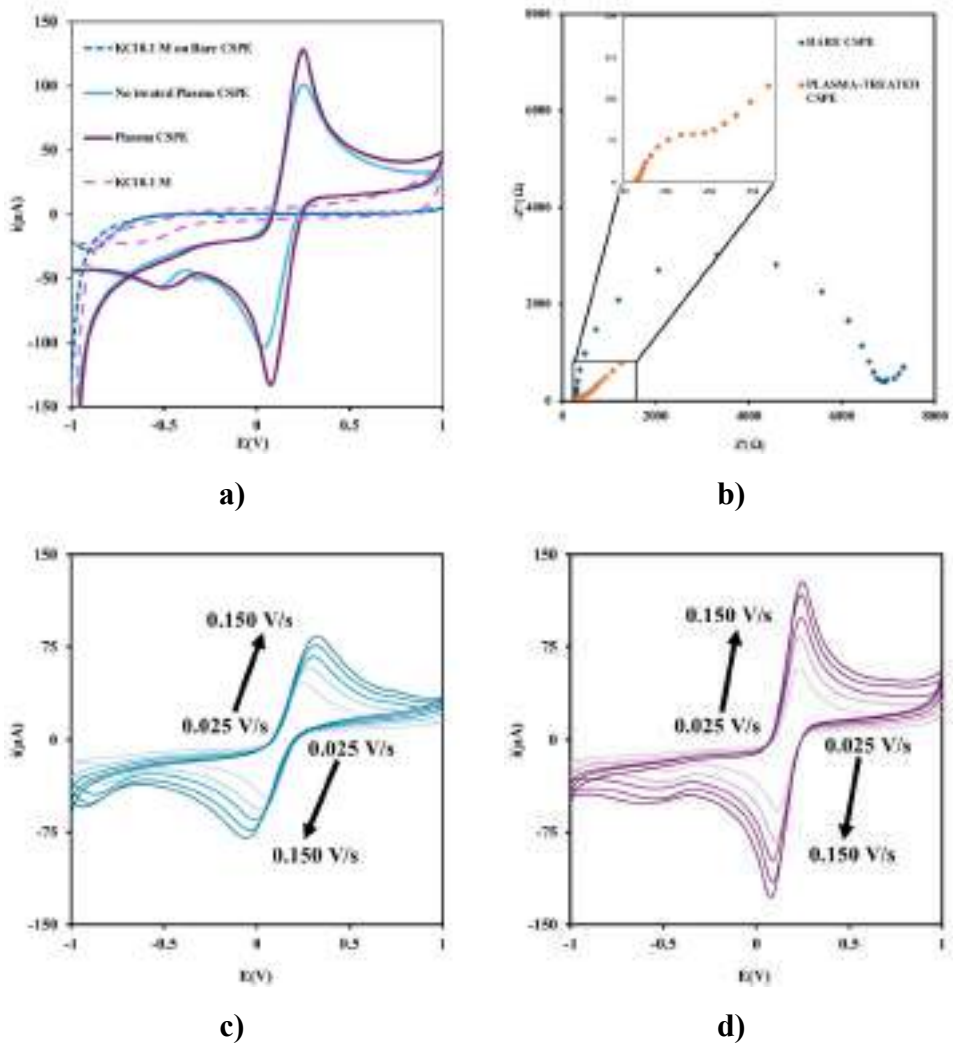

Figure 5.2-6 a) Cyclic voltammograms of bare CSPE and plasma-treated CSPE in 5 mM $[Fe(CN)_6]^{3-/4-}$ in 0.1 M KCl. Experimental parameters: potential range from -1.0 V to 1.0 V; 0.1 V/s**; b)** Nyquist plot of bare and plasma-treated CSPE in presence of 5 mM $[Fe(CN)_6]^{3-/4-}$ in 0.1 M KCl; Cyclic voltammograms of Bare and oxygen plasma-treated CSPEs in 5 mM $[Fe(CN)_6]^{3-/4-}$ with 0.1 M KCl. **c)** CSPE; **d)** oxygen-plasma treated CSPE. Experimental parameters: potential range from -1.0 V to 1.0 V; scan rates: 0.025, 0.050, 0.075, 0.100, 0.125, 0.150 V/s

The enhancement was further quantified through a detailed scan rate study (0.025 to 0.150 V/s). For both the bare and treated electrodes, the anodic and cathodic peak currents scaled linearly with the square root of the scan rate, confirming a diffusion-controlled process. By applying the Randles-Ševčík equation to the slopes of these plots, the effective electroactive area was calculated (**Table 5.2.9-I)**.

Table 5.2.9-I Electroactive areas of the Plasma-treated and untreated CSPE (in mm^2), calculated from the CV scans performed in $[Fe(CN)_6]^{3-/4-}$.

	CSPE	Plasma-Treated CSPE
A_{anodic}	5.3	10.0
$A_{cathodic}$	4.1	10.1
$\bar{A}$	4.6	10.1
%RSD	18.3	0.57
E_{anodic} **(V)**	0.55	0.44
$E_{cathodic}$ **(V)**	0.18	0.25
ΔE (V)	0.38	0.19
i_{anodic} **(μA)**	100	142
$i_{cathodic}$ **(μA)**	62	120

The results are striking: the plasma treatment approximately doubled the electroactive surface area, from an average of 4.6 mm² for the bare CSPE to 10.1 mm². Moreover, the treatment dramatically improved the reproducibility of the electrode surface, as reflected in the reduction of the relative standard deviation (RSD) for the area calculation from 18.3% down to 0.57%.

Complementary Electrochemical Impedance Spectroscopy (EIS) measurements provided additional, orthogonal evidence for this enhancement. The Nyquist plot for the plasma-treated CSPE (**Figure 5.2-6 b**) displayed a substantially smaller semicircular diameter compared to the bare electrode, directly corresponding to a lower charge transfer resistance (R_{ct}). This decrease in R_{ct} corroborates the CV findings, confirming that the plasma treatment creates a more facile pathway for electron exchange at the electrode-electrolyte interface. The collective data from CV and EIS strongly support the conclusion that the oxygen plasma treatment, beyond its role in device assembly, actively engineers the carbon surface to boost its intrinsic electrocatalytic performance.

Given this fundamental improvement, the interaction of the modified electrode with the target biomolecules was investigated. Initial CV studies with 5 mM dopamine (DA) in PBS (pH 5.5) revealed a parallel enhancement (**Figure 5.2-6).** The ΔEp for DA oxidation/reduction decreased by 57% on the plasma-treated surface (0.210 V vs. 0.370 V), while the anodic and cathodic peak currents increased by 139% and 197%, respectively. To assess practical utility and address known challenges of DA adsorption and surface fouling, the stability of the treated electrode was tested. Differential Pulse Voltammetry (DPV) measurements of a 50 μM DA solution were repeated eight times on the same plasma-treated CSPE. As illustrated in **Figure 5.2.9.6b**, the peak current remained remarkably stable across all repetitions, demonstrating that the treated surface resists fouling and enables reliable reuse—a vital attribute for a practical sensor.

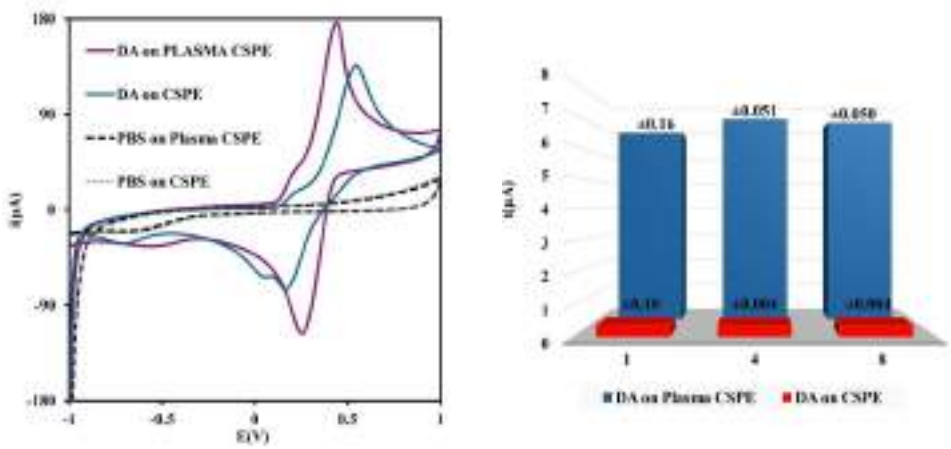

a) **b)**

Figure 5.2-7 a) Cyclic voltammograms of: Bare and oxygen plasma-treated CSPEs in 5 mM Dopamine (DA) in PBS solution at pH 5.5. CSPE and oxygen-plasma treated CSPE. Experimental parameters: potential range from -1.0 V to 1.0 V; 0.100 V/s. Each measurement was repeated at least seven times, with oxygen plasma treatment applied to the same platform after each scan**. b)** Peak current i(µA) obtained for 50 µM of DA in PBS pH 5.5 using DPV on CSPE and plasma-treated CSPE repeating the measurements 8 times using the same electrode. Experimental parameters: potential range from 0.0 V to 0.5 V, scan rate of 0.004 V/s, step potential of 0.002 V, pulse potential of 0.05 V, and pulse time of 0.05 s.

Figure 5.2-7 shows the peak current obtained for the first scan, the fourth, and the eighth, suggesting that the same platform can be reused at least eight times, maintaining consistent behaviour without significant DA adsorption on the surface.

The analytical performance for DA detection was rigorously quantified through calibration experiments. DPV responses were recorded for DA concentrations ranging from 0 to 100 µM. The sensitivity of the plasma-treated CSPE was profoundly greater than that of the untreated electrode, as clearly shown in the superimposed calibration curves (**Figure 5.2-8)**.

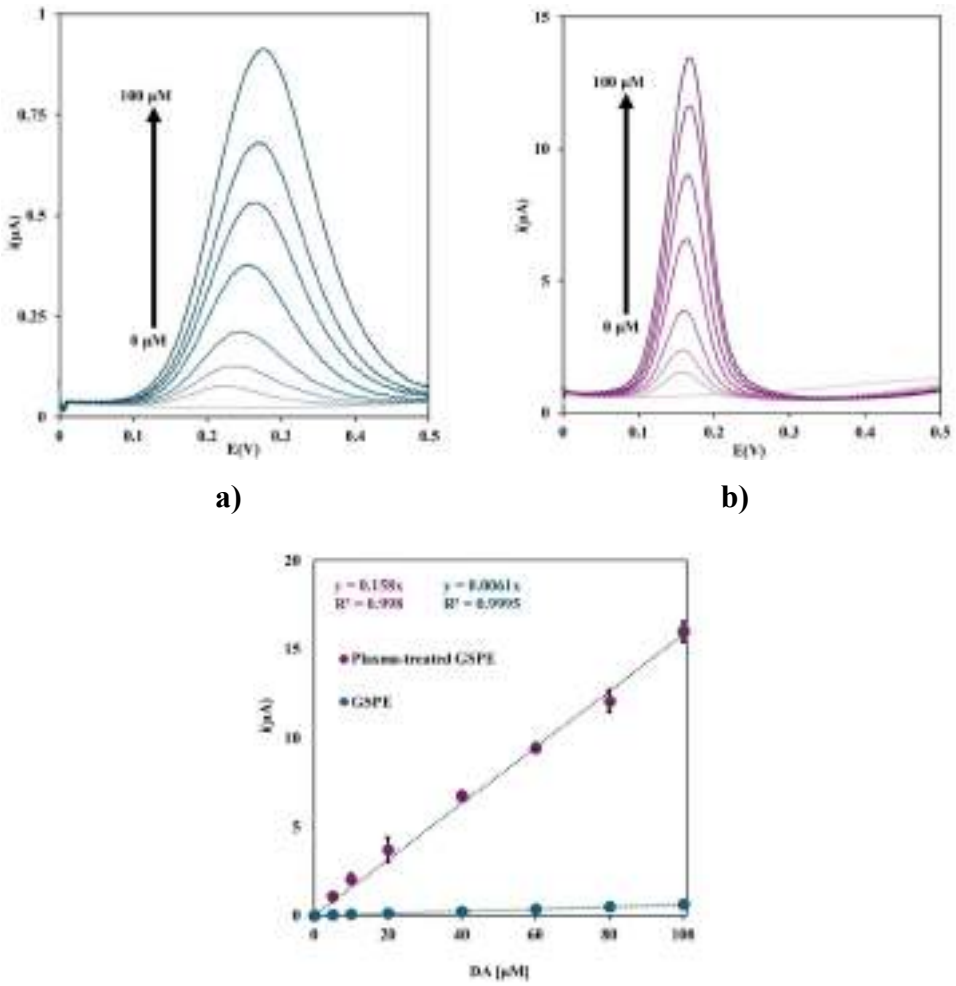

Figure 5.2-8 Differential pulse voltammograms performed with different DA concentrations (0-100 µM) in PBS (pH=5.5). Experimental parameters: potential range 0-0.6 V; scan rate 0.004 V/s; step potential 0.002 V; pulse potential 0.05 V; pulse time 0.05s on **a)** untreated CSPE; **b)** plasma-treated CSPE. **c)** Calibration curves for DA with untreated CSPE (blue) and on plasma-treated CSPE (violet). Each curve represents the average of at least four independent experiments conducted using different sensors.

The limit of detection (LOD) improved from 4 µM on the bare electrode to 0.65 µM on the treated surface, representing an order-of-magnitude gain in sensitivity. This stark difference underscores the efficiency of the plasma treatment in activating the carbon surface for DA electroanalysis.

Selectivity is a paramount concern for operation in complex biofluids like sweat. Molecules within the same oxidation potential window, such as Uric Acid and Ascorbic acid, have been employed on treated CSPE in order to investigate a possible overlap with the target molecule. Thus, uric acid (UA) and ascorbic acid (AA), common metabolites present in human peripheral biofluids were tested in presence of DA, at the physiological

concentrations of these two substances (approximately 10 μM) [236,237]. Therefore, the response of the plasma-treated CSPE was evaluated in the presence of common endogenous interferents: uric acid (UA) and ascorbic acid (AA), each at a physiologically relevant concentration of approximately 10 μM. The DPV responses demonstrated that the oxidation peaks for DA, UA, and AA were sufficiently resolved at the treated electrode, indicating a reduced risk of signal overlap and confirming the platform's potential for selective detection in real matrices. **Figure 5.2-9**

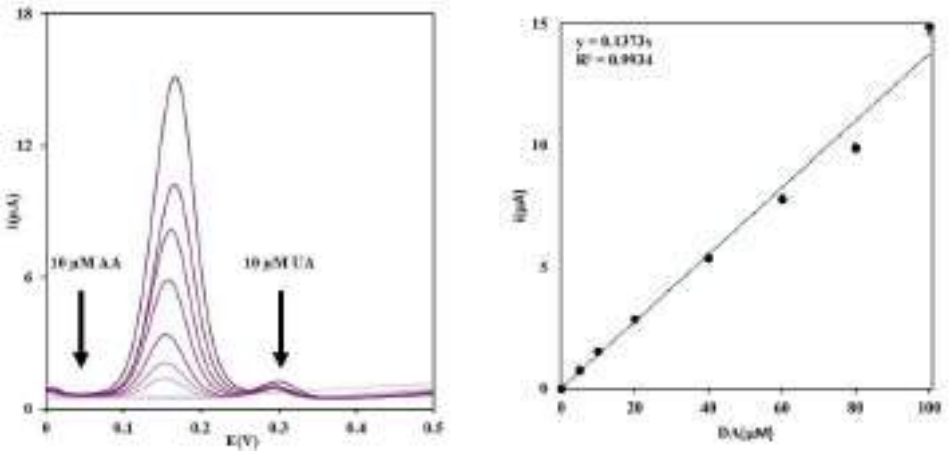

a) **b)**

Figure 5.2-9 Differential pulse voltammograms performed with different DA concentrations (0-100 μM) in PBS (pH=5.5). Experimental parameters: potential range 0-0.6 V; scan rate 0.004 V/s; step potential 0.002 V; pulse potential 0.05 V; pulse time 0.05s on **a)** plasma-treated CSPE. **b)** Calibration curves for DA on plasma-treated CSPE. Each curve represents the average of at least four independent experiments conducted using different sensors.

Finally, the investigation culminated in the analysis of the target therapeutic agent, levodopa (L-DA). The calibration curve for L-DA (0–100 μM) obtained via DPV on the plasma-treated CSPE is presented in **Figure 5.2-10.**

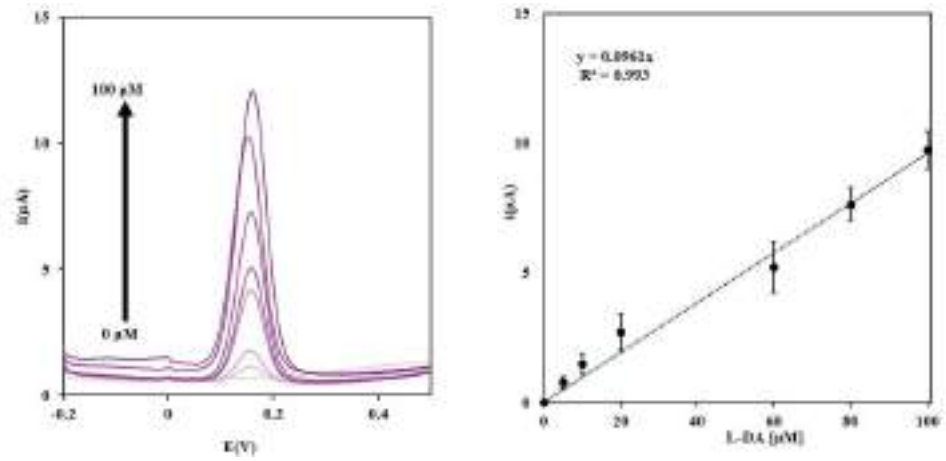

a) **b)**

Figure 5.2-10 Calibration curve of different concentrations of L-DA (0-100 µM) in PBS (pH=5.5) on plasma-treated CSPE **a)** Differential pulse voltammograms performed with different DA concentrations (0-100 µM) in PBS (pH=5.5). Experimental parameters: potential range 0-0.6 V; scan rate 0.004 V/s; step potential 0.002 V; pulse potential 0.05 V; pulse time 0.05s on. **b)** Calibration curves for DA on plasma-treated CSPE. Each curve represents the average of at least four independent experiments conducted using different sensors.

The calculated LOD and LOQ were 0.32 µM and 1.1 µM, respectively, with a reproducibility of circa 5% across five independently fabricated electrodes. These results confirm that the electrocatalytic enhancement induced by the oxygen plasma treatment extends beyond model redox probes and the neurotransmitter DA to directly benefit the sensitive and reproducible detection of the drug L-DA. In conclusion, the plasma treatment serves a dual, synergistic purpose: it is indispensable for creating a hydrophilic, sealed microfluidic system, and it simultaneously activates the integrated carbon electrode, elevating its analytical performance for the detection of both the biomarker and the drug without the need for additional chemical modifications or nanomaterials.

The dramatic improvement in electron transfer kinetics after plasma treatment can be attributed to two main factors: the removal of organic binders used in the commercial carbon ink, which often acts as a resistive barrier, and the introduction of oxygen-coating functional groups (such as a carboxyl, hydroxyl, and carbonyl groups) on the carbon edges. These groups act as coordination sites for Dopamine and Levodopa, which are known to be sensitive to the surface oxygen contet of carbon electrodes. By increasing the density of the active sites and the effective surface are simultaneously, the plasma

treatment lowers the activation energy for the $2e^-/2H^+$ oxidation process, explaining the 22-fold signal increase observes in DPV.

5.2.9.3 SWEAT ANALYSIS IN MICROFLUIDIC CHAMBER

The ultimate objective of this work is to translate the enhanced electrochemical performance of the plasma-treated sensor into a functional wearable device. This requires validating the complete, integrated system, where the sensor operates within the microfluidic network under conditions mimicking actual use. To this end, a series of experiments were conducted to evaluate the platform's performance for the direct analysis of levodopa in a dynamic, flow-through configuration.

Initial tests focused on characterizing the system's behaviour in a controlled environment. A calibration curve for L-DA was constructed using buffered solutions (PBS, pH 5.5) flowing through the assembled PDMS microfluidic device. As reported **Figure 5.2-11**, the differential pulse voltammetry (DPV) responses showed a well-defined concentration dependence.

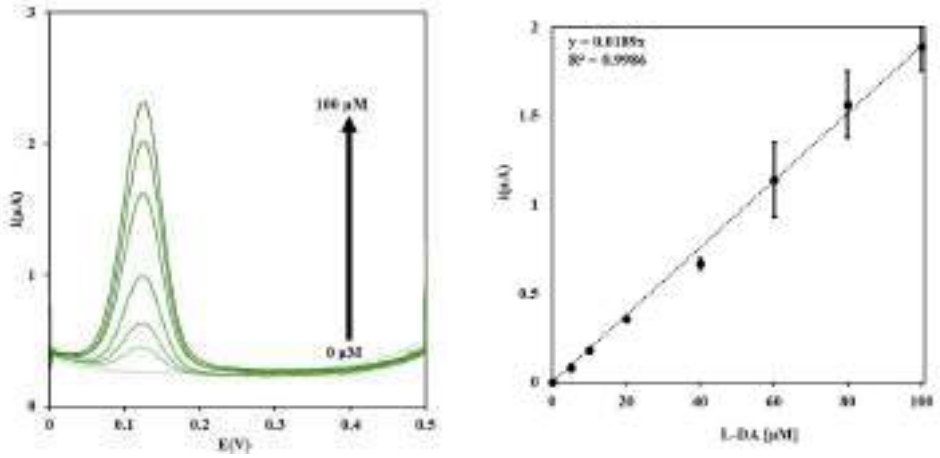

a) **b)**

Figure 5.2-11 Calibration curves of different concentrations of Levodopa (0-100 µM) in PBS (pH=5.5) on plasma-treated CSPE incorporated into a microfluidic PDMS-based device **a)** voltammogram of different concentrations of L-DA in microfluidic channel and **b)** resulting calibration curve obtained by plotting peak height intensity against L-DA concentrations. Experimental parameters: potential range 0-0.6 V; scan rate 0.004 V/s; step potential 0.002 V; pulse potential 0.05 V; pulse time 0.05s. LOD 1 µM and LOQ 4 µM.

The resulting calibration curve demonstrated that the sensor's high performance was fully retained within the closed microfluidic architecture, yielding a limit of detection (LOD) of 1 µM and a limit of quantification (LOQ) of 4 µM. This successful transfer from a simple droplet configuration to a microfluidic format confirms that the integration process, encompassing plasma treatment, sensor embedding, and channel sealing, does not compromise the electrocatalytic activity or the reliability of the measurement

Having established the system's functionality in a buffer matrix, the next critical step was to assess its operability in a physiologically relevant medium. The performance of the proposed sensor was therefore evaluated using artificial human sweat, a complex matrix designed to replicate the ionic strength, pH, and chemical composition of real eccrine sweat, including numerous potential interferents. A calibration curve for L-DA was recorded directly in this artificial sweat without any sample pre-treatment, thereby testing the system under the most challenging and application-relevant conditions. The DPV measurements, performed using the same parameters optimized for buffer solutions, produced the voltammograms and corresponding calibration curve shown in **Figure 5.2-12**

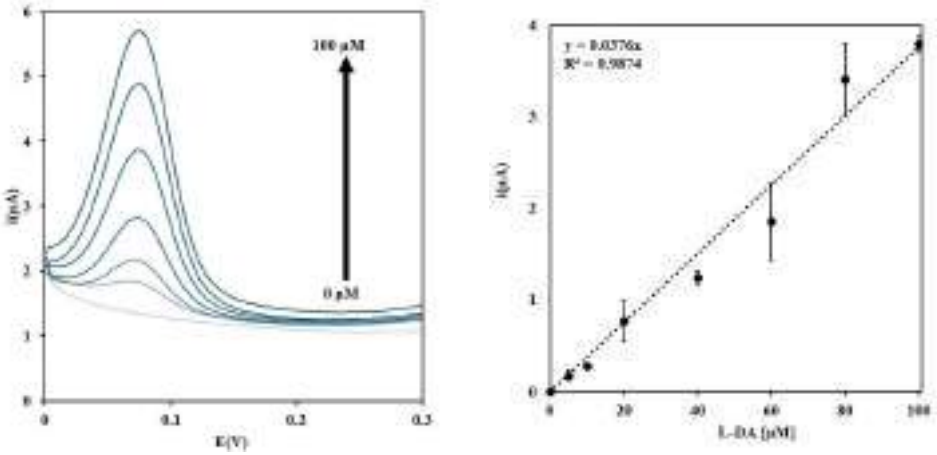

a) **b)**

Figure 5.2-12 Calibration curves of different concentrations of levodopa (0-100 µM) and artificial human sweat (pH=5.5) on plasma-treated CSPE. **a)** Differential pulse voltammetry obtained with the following experimental parameters: potential range 0-0.6 V; scan rate 0.004 V/s; step potential 0.002 V; pulse potential 0.05 V; pulse time 0.05s and **b)** resulting calibration curve.

Analysis in this complex matrix yielded a LOD of 4 µM and an LOQ of 12 µM for L-DA. While these values represent a predictable increase compared to the ideal buffer medium, a common consequence of matrix effects in electroanalysis, they remain highly significant for the intended application. The obtained sensitivity comfortably covers the

clinically relevant concentration range for levodopa in sweat, which is anticipated based on established blood-sweat correlations. This result robustly demonstrates that the integrated microfluidic sensor platform maintains high analytical performance even when confronted with the multifaceted composition of sweat. It thereby guarantees the feasibility of determining L-DA levels directly on a patient's skin in a continuous, non-invasive manner, fulfilling a core requirement for personalized therapeutic drug monitoring in Parkinson's disease management. It is noteworthy that the LOD in artificial sweat (4 μM) remains well within the therapeutic monitoring window for Levodopa. The slight loss in sensitivity compared to the *in-drop* configuration is compensated by the microfluidic protection; the PDMS ceiling prevents sample evaporation, a major issue in wearable sensing that causes concentration drifts and ensures a constant volume of electrolyte over the electrode. This structural stability is crucial for long-term monitoring on the skin, where the sensor must provide reliable data despite patient movement and varying perspiration rates.

5.2.10 Conclusion

This chapter successfully demonstrates the development of an integrated, robust, and highly sensitive electrochemical platform for the non-invasive monitoring of levodopa (L-DA) in sweat.

The central innovation resides in the strategic use of a single oxygen plasma treatment, which serves a dual and synergistic purpose. Firstly, it acts as a pivotal one-step surface modification for the carbon screen-printed electrodes (CSPEs), drastically enhancing their electrocatalytic properties. This enhancement was comprehensively quantified through fundamental characterization: the plasma treatment doubled the electroactive surface area, reduced the peak separation for the $[Fe(CN)_6]^{3-/4-}$ redox probe by 71%, and significantly improved charge transfer kinetics. When applied to L-DA detection the plasma treatment yielded a 22-fold signal increase in DPV and excellent operation stability, allowing for multiple reuses and achieving a low detection limit of 0.32 μM in buffered solution.

Secondly, and critically for device integration, the very same plasma treatment facilitates the permanent and hydrophilic bonding of the PDMS layers, enabling the fabrication of a sealed microfluidic chamber in a streamlined "all-in-one" process. This seamless integration ensures that the enhanced sensor performance is effectively translated into a functional wearable form factor. The validation of the complete system within this

microfluidic environment confirmed its practical utility. The platform maintained high analytical performance when challenged with the complex matrix of artificial human sweat, achieving a clinically relevant detection limit of 4 μM for L-DA without any sample pre-treatment.

Therefore, we present a complete and compelling solution: that bridges material science, electrochemistry, and microfluidic engineering. The developed platform, centred on a plasma-treated CSPE that is simultaneously activated for sensing and primed for integration, establishes a promising, cost-effective foundation. It paves the way for the future realization of non-invasive, wearable devices capable of the real-time therapeutic drug monitoring of L-DA, ultimately supporting personalized dose management for Parkinson's disease patients.

5.3 ACKNOWLEDGMENT

This work was developed in collaboration with Dr. Neri Fuochi, Dr Daniele Martella, Dr Ruggero Rossi, Dr Marco Catarzi, Prof. Camilla Parmeggiani, Prof. Ilaria Palchetti and Prof. Giovanna Marrazza, whose support is gratefully acknowledged.

Note on Publications: The research detailed in this chapter has led to the following peer-reviewed publications, in which the author of this thesis is a contributing co-author:

1. I. A. Vitale, N. Fuochi, D. Martella, C. Parmeggiani, G. Marrazza, and I. Palchetti, "Skin-contact wearable electrochemical biosensing tools: A perspective for the wellbeing of neurological patients," TrAC Trends in Analytical Chemistry, vol. 180, p. 117965, Nov. 2024, doi:10.1016/j.trac.2024.117965.
2. I. A. Vitale, N. Fuochi, R. Rossi, M. Catarzi, D. Martella, C. Parmeggiani, G. Marrazza, and I. Palchetti, "Plasma-Treated Carbon Sensor coupled to PDMS-based Microfluidic platform for the determination of Levodopa in Sweat" Electrochemical Acta **under review**

This work was supported by the European Union - Next Generation EU, in the context of The National Recovery and Resilience Plan, Investment 1.5 Ecosystems of Innovation, Project Tuscany Health Ecosystem (THE), CUP:B83C22003920001. The LENS Mechanical workshop and Dr. Ahmed Hajeb are acknowledged for the help with the microfluidic system design.

6. Rethinking Affinity Sensing: How Synthetic Receptors and Laser-Induced Graphene Electrodes Are Redefining Wearable Electrochemical Analytics

6.1 Affinity Sensing in Clinical Trials

The detection of molecular biomarkers in bodily fluids is a cornerstone of clinical diagnostics, given their direct correlation with disease onset, progression, and therapeutic response. Conventional quantification methods, such as enzyme-linked immunosorbent assay (ELISA), Western blot, and polymerase chain reaction (PCR), have long served as analytical gold standards. While these techniques offer exceptional sensitivity and specificity, their inherent complexity renders them fundamentally incompatible with the core requirements of PoC diagnostic devices, as highlighted in recent literature [238]. This incompatibility stems from their time-consuming protocols, dependence on highly trained personnel, and reliance on specialised laboratory equipment.

Nevertheless, the diagnostic success of these established methods relies on a fundamental biochemical event: specific molecular recognition through affinity interactions. Traditional affinity-based assays, such as ELISA, typically translate this binding event into a measurable signal through optical means, employing labelled antibodies that, after the addition of an enzyme, can generate colorimetric, fluorescent, or chemiluminescent readouts [239]. While effective, this optical transduction paradigm often involves multi-step procedures and complex reagent system that hinder miniaturisation and simplification.

In order to overcome these issues, electrochemical biosensors present a compelling alternative for transforming the same affinity recognition event into a directly readable electrical signal [240]. Indeed, by leveraging the principle of electrochemistry, these platforms can convert the binding of a target biomarker at the sensor surface into changes in current, potential, or impedance.

6.2 Electrochemical Affinity Sensing Paradigm

The evolution of biosensing technology, beginning in the 1960s with foundational work on enzyme electrodes and biocatalytic membranes, established a powerful principle: the integration of biological recognition with physiochemical transduction [241]. This paradigm was brilliantly exemplified by the development of the glucose sensor, which progressed from measuring oxygen consumption to employing mediated electron transfer with ferrocene derivatives, ultimately culminating in the disposable, pen-sized devices widely used today [242]. This trajectory underscores a central theme in diagnostic development: the relentless drive toward miniaturisation, ease of use, and PoC applicability.

Modern biosensors are broadly classified by their recognition mechanism into two categories: catalytic and affinity based. Catalytic biosensors utilise biological elements like enzymes, whole cells, or tissues to catalyse the conversion of a target substrate, generating a measurable product. In contrast, affinity biosensors rely on molecular recognition events where a bioreceptor selectively binds to a target analyte without altering it chemically. This category encompasses receptors such antibodies, nucleic acids, aptamers, and synthetic receptors mimics like molecularly imprinted polymers (MIPs). It is this affinity-based paradigm, particularly when coupled with electrochemical transduction, that holds exceptional promise for wearable clinical diagnosis [34].

Electrochemical affinity biosensors function by converting a specific binding event at the electrode surface into a quantifiable electrical signal, a shift in current, potential, or impedance. This direct electronic transduction offers inherent advantages for wearable applications: compatibility with miniaturised electronics, low power consumption, and the ability to function with a small sample volume, such as microliters of bodily fluids.

Within this framework, the choice of bioreceptors is of paramount importance. Indeed, for the detection of protein-based biomarkers, antibodies have long been the gold standard. Their high specificity enables the development of sensitive immunosensors, often adapting the robust principles of ELISA to an electrochemical format [243,244]. Their success has fuelled significant advances in real-time, multiplexed detection [245]. Similarly, engineered peptides and aptamers, synthetic oligonucleotides selected for high-affinity binding, offer valuable alternatives, providing potentially greater stability and design flexibility than traditional antibodies [246–249].

However, the translation of these biological recognition elements from laboratory settings to robust, wearable, and continuous monitoring platforms presents distinct challenges. For example, their inherent biological nature, sensitivity to denaturisation, limited shelf-life, batch-to-batch variability, and often complex immobilisation requirements, can conflict with the demands of a low-cost, durable and user-friendly device [250,251].

This tension between excellent *in vitro* performances and practical *in vivo* employability highlight a critical bottleneck in the field of wearable electrochemical analytics. It is precisely this limitation that motivates the exploration of fully synthetic affinity receptors, which promise to retain the critical function of specific molecular recognition while bestowing the robustness, reproducibility, and stability required for the next generation of personal health monitors.

6.3 Bio-Inspired Receptors on Laser-Induced Graphene electrodes for Chronic Disease Monitoring

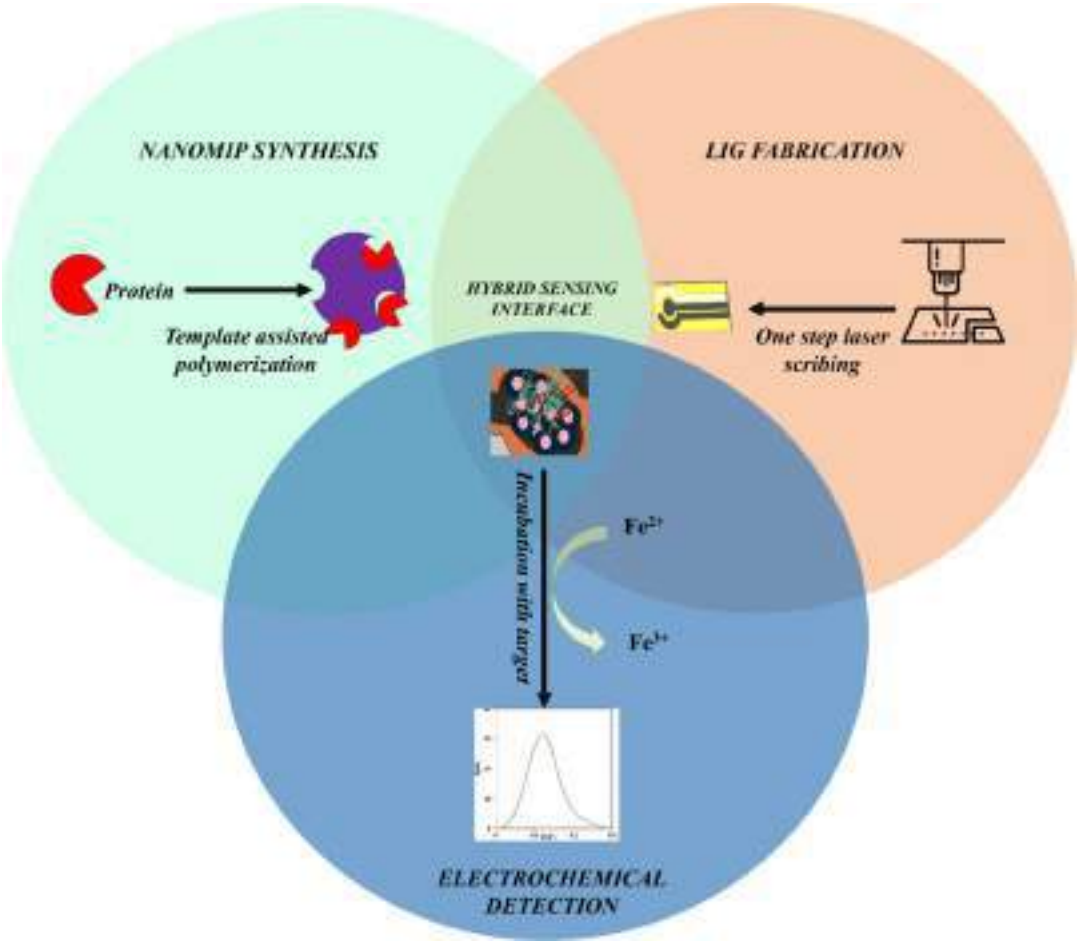

Figure 6.3-1. Graphical abstract of the hybrid sensing platform for protein biomarker detection. The diagram illustrates the convergence of three core technological pillars: (i) the synthesis of nanostructured molecularly imprinted polymers (NanoMIPs) via

template-assisted polymerization, (ii) the high-throughput fabrication of Laser-Induced Graphene (LIG) electrodes, and (iii) the electrochemical transduction mechanism. The hybrid interface enables specific protein capture, quantified through Square Wave Voltammetry (SWV) by monitoring the binding-induced hindrance of $[Fe(CN)_6]^{3-/4-}$ redox probe.

6.3.1 State of Art

The pursuit of affordable, durable and mass-producible biosensing platforms has catalysed significant innovation in two parallel domains: synthetic molecular recognition elements [252] and flexible electronics [253]. On one front, synthetic receptor, particularly in their nanostructured forms, such as nanoMIPs, have emerged as a compelling alternative to biological recognition elements. Indeed, they provide a unique combination of customisable binding affinity, excellent operational stability, and high synthetic reproducibility [254–256] making them inherently suitable for devices that must function reliably outside controlled laboratory settings.

Concurrently, the field of flexible electronics has seen the rise of Laser-Induced graphene (LIG) electrodes as a premier substrate for wearable sensors [257]. Fabricated through the direct laser conversion of polymeric precursor, LIG provides a highly conductive, porous, and mechanically compliant electrode material that can be seamlessly integrated into on-body platforms [93].

The convergence of these two advancements creates a powerful synergy. The robust, synthetic nature of nanoMIPs addresses the durability and cost limitations of bioreceptors, while the versatility and manufacturable architecture of LIG offers an ideal electrochemical transducer for wearable integration.

This chapter explores the deliberate coupling of these technologies to establish a new paradigm for robust affinity sensing. The fundamental scientific challenge involves the effective functionalisation of LIG's complex three-dimensional surface with synthetic nanoMIP, ensuring that the immobilisation strategy preserves both the electrochemical properties of the electrode and the binding affinity of the receptors. Furthermore, the resulting hybrid platform must demonstrate selectivity towards the selected protein, that serves as analyte. Therefore, the performance of nanoMIPs onto the LIG electrodes surfaces was evaluated in parallel on a conventional benchmark platform (SPGE). This comparative approach serves as a key diagnostic function: it allows to decouple the intrinsic performance of the synthetic receptor from the influence of the new substrate, thereby demonstrating unequivocally that the nanoMIPs maintain their core functionality when transferred to the flexible, laser-induced graphene surface.

6.3.2 Chemicals

Given the proprietary nature of the core recognition elements under development, this section provides a functional description of the materials while protecting specific compositional details covered by ongoing intellectual property protocols. All reagents for buffer preparation, including phosphate buffer saline tabs (PBS), sodium chloride (NaCl), potassium chloride (KCl), iron (III) chloride ($FeCl_3$), polyvinyl butyral (PVB), silver paste, bovine serum albumin (BSA), ethanolamine, and standard electrochemical probes such as potassium ferricyanide ($[Fe(CN)_6]^{3-/4-}$), methanol, ultrapure MilliQ water were of analytical grade and obtained from Sigma-Aldrich.

6.3.3 Apparatus

Flexible laser-induced graphene electrodes (LIGs) were fabricated in-house via the direct laser scribing on a 75 μm thick polyimide (PI) film(Kapton® HN, DuPont). The process was performed using a Gravotech LW2 laser scribing machine equipped with a DPSS 532 nm green laser system configured with optimised parameters of 1% power, 40% speed, 47 Hz frequency and 1,000 points per inch (PPI). In order to form the reference electrode, silver paste has been applied to the designed area and left to dry. The dried silver layer has been subsequently chlorinated by adding 0.1 M $FeCl_3$ solution for 30 second to generate Ag/AgCl.

For allowing the stabilisation of the reference potential, 30 μL of a PVB reference cocktail, prepared by dissolving 79 mg of PVB and 50 mg of NaCl in 10 mL of methanol, was drop-cast onto the Ag/AgCl surface and allowed to dry overnight, resulting in a robust and stable solid-state reference electrode suitable for flexible electrochemical sensor integration.

6.3.4 Synthetic Receptor Functionalisation

The working electrodes, including conventional SPGE and LIG platform, were functionalised with nanostructured molecularly imprinted polymers (nanoMIPs) designed for specific recognition of target proteins, such as CD22 and β-2- microglobulin (β2M). The synthesis and precise molecular design of these nanoMIPs are part of a proprietary development process. For immobilisation, a physical adsorption strategy has been employed to anchor the nanoMIPs onto both gold and carbon-based surfaces, followed

by a blocking a step with BSA and ethanolamine in order to minimise non-specific binding. While the exact peptide or protein template used during nanoMIP synthesis cannot be disclosed here, it belongs to a class of clinically relevant biomarkers, thereby underscoring the translational potential of this sensing platform.

6.3.5 Rebinding Assay

The rebinding assay to demonstrate the retained affinity of the immobilised nanoMIPs followed a consistent protocol for both platforms. After a stabilization of 15 minutes in buffer, electrodes were incubated in solutions containing an increasing concentration of the target peptide. Following incubation and a rinsing step, the specific binding event was quantified using Square Wave Voltammetry (SWV) with the auxiliary of the external redox probe $Fe(CN_6)^{3-/4-}$. The SWV parameters were carefully optimized for this interface, with an equilibration time of 1 s, a potential window from -0.3 V to +0.6 V, a step potential of 5 mV, an amplitude of 50 mV, and a frequency of 10 Hz. This technique was selected for its high sensitivity and its proven ability to detect subtle, binding-induced changes at the electrochemical interface. The resulting voltametric signal was analysed by plotting the change in the oxidation peak current against the target peptide concentration or protein concentration to generate a sensitive binding curve. All measurements were performed in a controlled, buffered environment to ensure a direct and valid comparison between the SPGE and LIG platforms.

6.3.6 Results and Discussion

6.3.6.1 Surface Characterization: Direct Visualization of NanoMIPs Immobilization on LIG

The successful functionalization of the LIG electrode surface with the synthetic receptors is a critical first step. To provide direct, visual evidence of this integration, fluorescence microscopy was employed. The nanoMIPs used in this study were synthesized to incorporate a fluorescent tag, allowing for their specific detection.

Figure 6.3-2 presents florescence micrographs of the LIG surface before and after the physical absorption procedure.

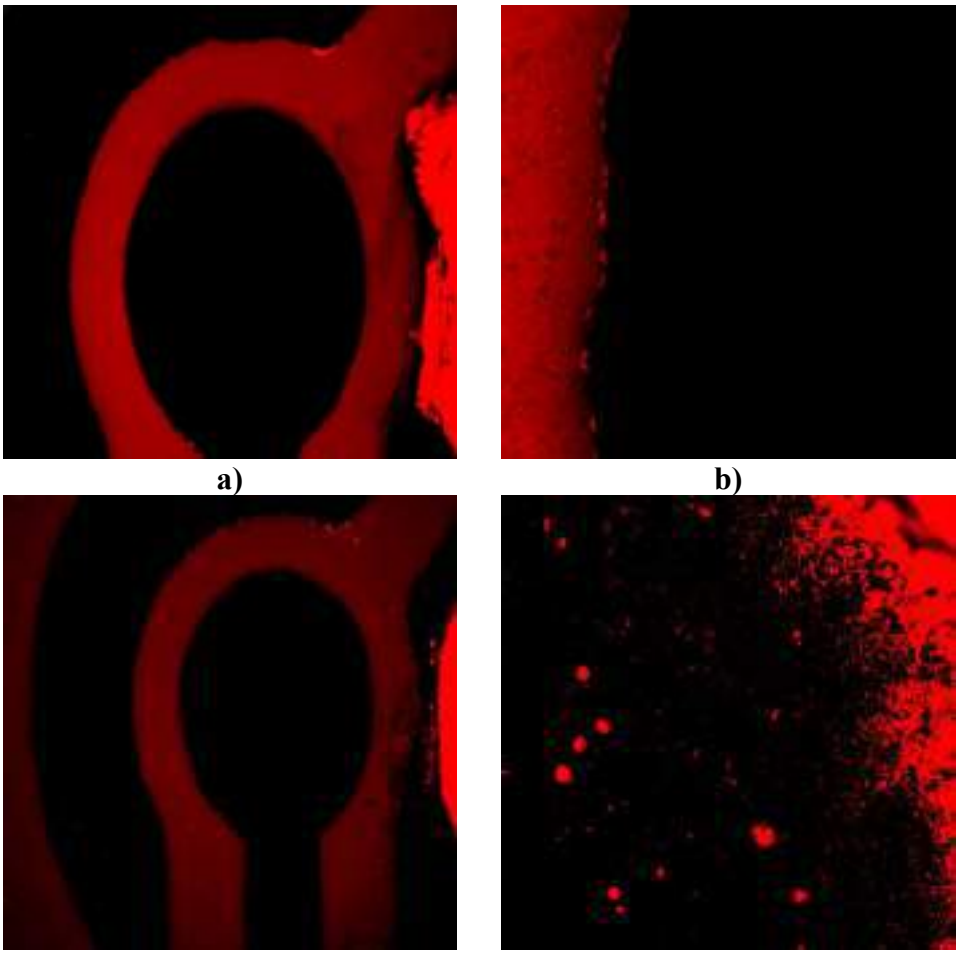

Figure 6.3-2 Florescence microscopy characterisation of nanoMIP immobilisation on LIG electrodes. nanoMIPs have been labelled with a fluorescent probe to enable direct visualisation of surface coverage. Low- magnification (2x) view of **a)** bare LIG surface morphology and **c)** modified surfaces after nanoMIPs functionalisation. High-magnification (10x) details of **b)** bare surface morphology and **d)** modified surfaces.

The higher-magnification images (**Figure 6.3-2b and d)** provide a detailed comparison: while the bare surface (**Figure 6.3-2b)** shows no specific fluorescence, the functionalised surface (**Figure 6.3-2d)** clearly displays a diffuse and particulate fluorescent signal distributed across the imaged area. This indicates that the nanoMIPs are physically adsorbed and dispersed over the LIG scaffold. While some heterogeneity in local intensity is apparent, an expected consequence of physically adsorbing nanoparticles onto a surface, the nanoMIPs are sufficiently distributed to create a functional layer of synthetic receptors.

6.3.6.2 Functional Validation: Comparative Rebinding Performance on SPGE and LIG Electrodes

Following the physical confirmation of nanoMIPs integration via microscopy, we evaluated their core functional property: specific molecular recognition. A direct comparative assessment was performed between the conventional SPGE and the novel LIG platform.

The binding event has been monitored electrochemically using Square Wave Voltammetry (SWV). This method quantifies the hindrance to the electron transfer of the redox probe $[Fe(CN_6)]^{3-/4-}$ caused by target peptide capture within the nanoMIP layer. **Figure 6.3-3** presents the resulting rebinding isotherms for both platform, plotting the normalised change in SWV peak current ($\Delta I/I_0$) against the logarithm of the peptide concentration for two distinct nanoMIPs system: one specific for CD22 (**Figure 6.3-3a c)** and another for the β2M (**Figure 6.3-3b d)**.

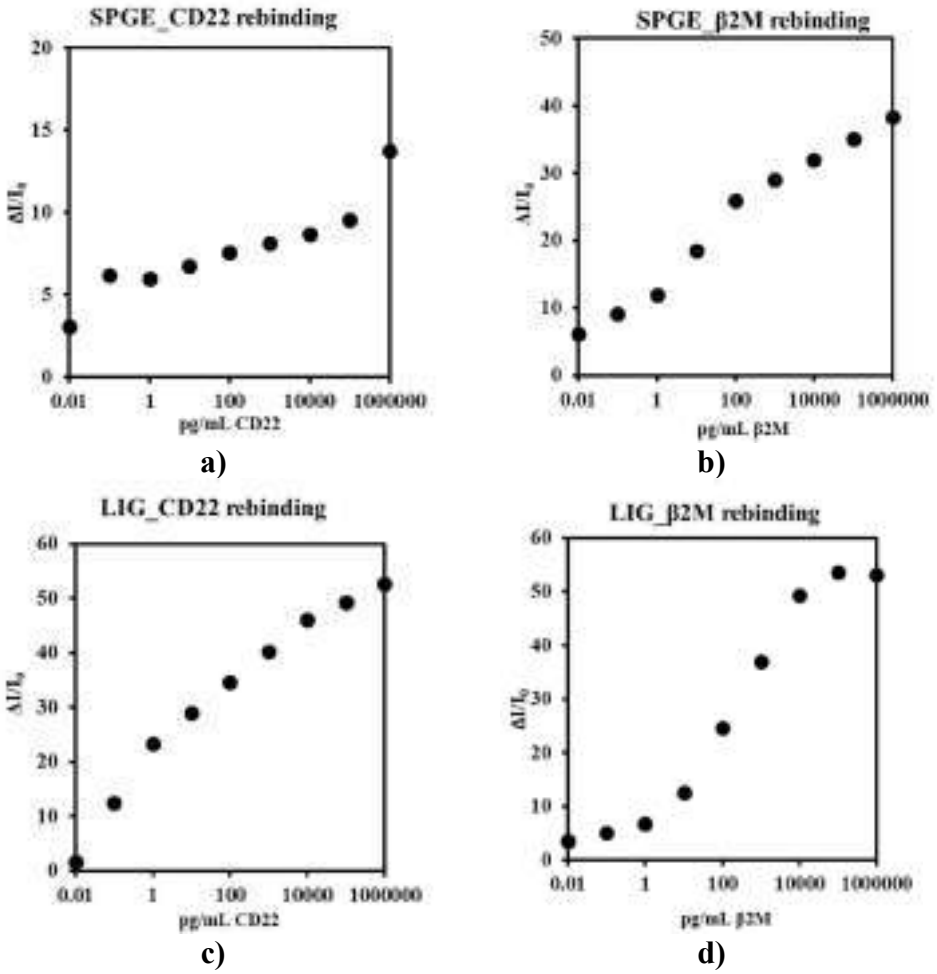

Figure 6.3-3. Comparative rebinding assays plots of nanoMIP functionalised SPGE (**a and b)** and LIG electrodes (**c and d)** with CD22 specific nanoMIP (**a, c)** and β2M nanoMIP (**b,d)** respectively.

A critical analysis of the data reveals two fundamental outcomes. First, the binding profiles for SPGE and LIG are highly congruent for both nanoMIP types. The half-saturation points and the overall sigmoidal shape of the curves, key indicators of apparent affinity, are virtually identical. This demonstrates conclusively that the specific recognition function of the nanoMIPs is fully preserved upon transfer from a flat, metallic surface to the rough, three-dimensional architecture of LIG.

The second, and most striking, observation is the difference in signal magnitude. The absolute decrease in peak current (ΔI) is consistently and significantly greater on the LIG platform for both targets. This enhanced signal suppression is a direct functional correlate of the fluorescence microscopy data. It can be attributed to the higher effective surface area and superior loading capacity of the porous LIG scaffold, which supports a greater density of accessible synthetic receptors. Consequently, a larger number of binding events occur, amplifying the overall electrochemical response. This result underscores a key advantage of the LIG substrate: it not only maintains the intrinsic affinity of the nanoMIPs but, due to its favourable morphology, also enhances the transduced signal, leading to improved sensor sensitivity.

This signal transduction mechanism in this nanoMIP-LIG platform is based on the 'gate-closing' effect. The nanoMIPs are non-conductie polymeric particles; when the target protein (CD22 o β2M) fills the specific imprinted cavities, it creates a steric and electrostatic barrier that further hinders the diffusion of the $[Fe(CN)_6]^{3-/4-}$ redox probe toward the graphene surface. The superior signal magnitude observed on LIG (ΔI) is not only due to the higher surface area but also to the hierarchical porosity of the graphene flakes. The laser-induced process creates a network of macro- and meso-pores that acts as reservois for the nanoMIPs, ensuring that binding event occurs throughout the 3D volume of the electrode rather than just on a 2D plane, thus multiplying the total impedance charge for every binding event.

6.3.6.3 Specificity Assessment

The binding specificity of the β2M-targeting nanoMIPs was evaluated using cross-reactivity assay, the rebinding experiment was conducted not only with its cognate target (β2M protein) but also with a non-target protein (CD22) under identical conditions. The resulting binding profiles are presented in **Figure 6.3-4.**

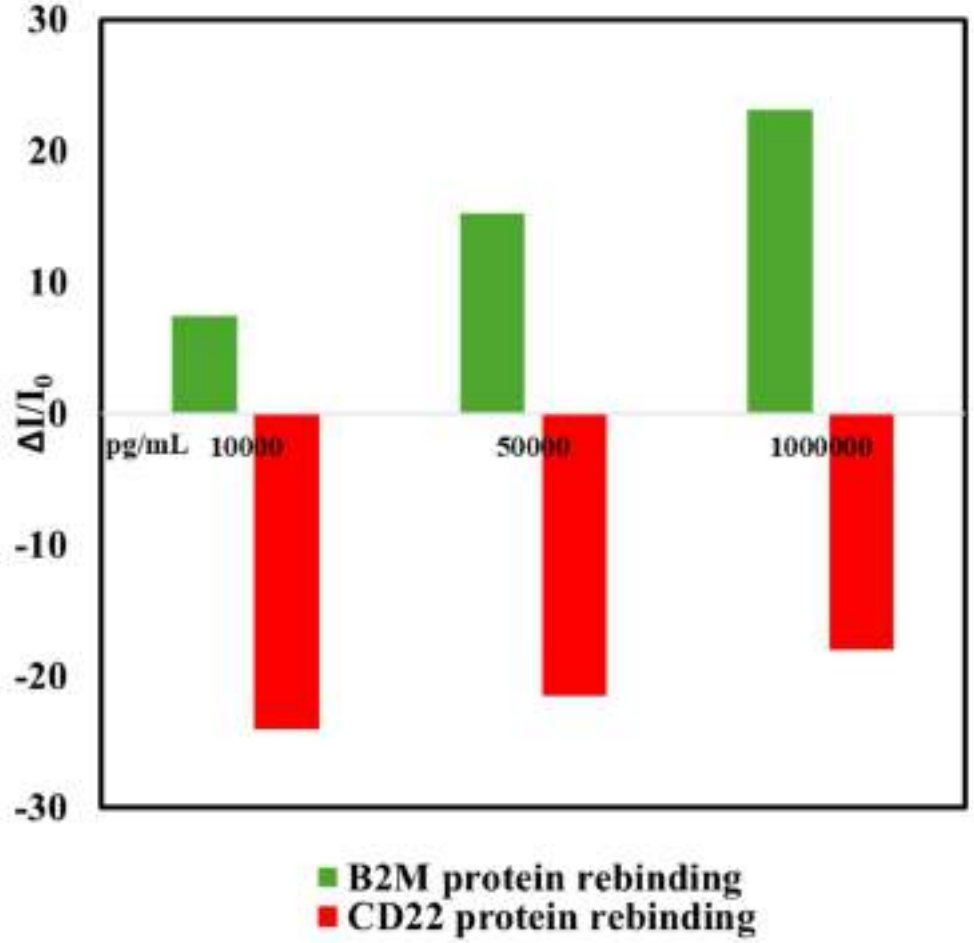

Figure 6.3-4 Cross-reactivity of **β2M** nanoMIP with **β2M** protein (green) and CD22 protein (red) rebinding concentration

A clear, concentration-dependent response has been observed only for the β2M protein (green bars), characteristic of specific affinity binding. In contrast, incubating with the CD22 protein (red bars) produce a negligible change in signal across the same concentration range, demonstrating a lack of non-specific interaction.

This result confirms the high specificity engineered into the synthetic respect. The nanoMIP selectively recognises its imprinted target (β2M) while effectively discriminating against a non-cognate protein of similar size and origin. Importantly, this selective behaviour is maintained on the complex, three-dimensional architecture of the LIG electrode. This successful demonstration of specific molecular recognition of a flexible, porous carbon substrate paves the way for the application of such nanoMIP-LIG platforms as robust sensing interfaces for the detection of specific biomarkers in complex biofluids.

This high specificity, even in the presence of structurally similar interferents, is a hallmark of the lock-and-key mechanism programmed into the nanoMIPs during template-assisted synthesis. Unlike antibodies, which can suffer from conformational changes when adsorbed onto carbon substrates, the rigid cross-linked structure of the nanoMIPs protect the binding sites. This structural integrity is particularly beneficial for LIG electrodes, where the high local surface energy of the graphene edges might otherwise denature fragile biological receptors. The nanoMIP-LIG synergy thus provides a chemically hardened interface suitable for the fluctuating pH and salinity conditions of human biofluids.

6.3.7 Conclusion

In this chapter a paradigm shifts in the design of wearable affinity sensors, moving from reliance on biological recognition elements toward a fully synthetic and integrated architecture has been presented. By strategically combining the molecular selectivity of peptide-imprinted nanoMIPs with the versatile, scalable fabrication of laser-induced graphene (LIG) electrodes, we have established a robust platform that directly addresses the critical limitations of stability, reproducibility, and cost associated with conventional biosensors for continuous monitoring.

The investigation proceeded through a logical sequence of validation. First, fluorescence microscopy provided direct visual evidence of the successful physical integration, confirming that the nanoMIPs were effectively immobilized across the porous, three-dimensional LIG scaffold. The core functional validation followed, with a comparative electrochemical rebinding study revealing two pivotal outcomes: the apparent affinity of the nanoMIPs was fully preserved when transferred from conventional gold electrodes to the LIG surface, and the signal transduction was significantly amplified on LIG due to its higher effective surface area and superior receptor loading capacity. Finally, the specificity assessment confirmed that the synthetic receptors retain their ability to discriminate between target and non-target proteins, even on the complex LIG substrate. Collectively, these results validate the "nanoMIP-on-LIG" concept as a promising and practical foundation for next-generation wearable diagnostics. This work demonstrates that the key attributes of an ideal wearable sensor (sensitivity, specificity, robustness, and manufacturability) can be synergistically achieved through the rational combination of advanced materials and synthetic chemistry, rather than through incremental improvements to fragile biological systems.

Looking forward, this platform opens several compelling avenues for research. The immediate next steps involve testing the sensor's performance in authentic, complex biofluids such as sweat or interstitial fluid to evaluate matrix effects and fouling . Furthermore, the mechanical robustness of the flexible LIG-nanoMIPs composite should be rigorously quantified under repeated bending and stretching to simulate on-body wear. In conclusion, this chapter successfully rethinks the affinity sensing paradigm for wearables. It provides a compelling blueprint for moving beyond the limitations of biology, leveraging synthetic recognition and advanced material fabrication to create durable, sensitive, and specific tools that can meet the demanding requirements of personalized, decentralized healthcare. Ultimately, the transition to synthetic receptors on LIG substrates marks a fundamental step toward the commercialization of wearable affinity sensors. By eliminating the 'cold-chain' requirement and the fragility of biological antibodies, we have demonstrated a platform that remains functional in ambient conditions. This research proves that the future of neurological and chronic disease monitoring lies in the convergence of laser-patterned carbon materials and biomimetic chemistry, offering a scalable path toward daily-wear diagnostics that are as robust as the electronics that power them

6.4 ACKNOWLEDGMENT

This work was developed in collaboration with Dr. Giulia Selvolini, Prof. Giovanna Marrazza who belong to University of Florence (Italy) and Dr. Md Sharifuzzaman, Dr. Nastasia Sanda Mouldovean-Cioroianu, Prof. Dr. Zeynep Altintas who belong to Bioinspired Materials and Biosensors Technologies, Christian-Albrechts-Universität zu Kiel (Germany), whose support is gratefully acknowledged.

Note on Publications: The research detailed in the introduction of this chapter has led to the following peer-reviewed publication, in which the author of this thesis is a contributing co-author:

Giovanna Marrazza, Murugan Ramalingam, Abinaya Jaisankar, Lijia Cheng, Giulia Selvolini, Ilaria Antonia Vitale, Advancements and emerging technologies in biosensors for rapid and accurate virus detection, TrAC Trends in Analytical Chemistry, Volume 172, 2024, 117609, ISSN 0165-9936, https://doi.org/10.1016/j.trac.2024.117609.I.

This work was primarily conducted during a research visit at Kiel University. The research was supported in part by funding from the Aventis Foundation (Project number: 80304368), Joachim Herz Foundation (Project number: 803043), and the European Union - Next Generation EU, in the context of The National Recovery and Resilience Plan, Investment 1.5 Ecosystems of Innovation, Project Tuscany Health Ecosystem (THE), CUP:B83C22003920001.

7. Remarkable Conclusions

The paradigm of healthcare is undergoing a profound transformation, shifting from episodic, reactive interventions toward a model of continuous, personalised monitoring. This evolution, essential for managing chronic disease and tailoring effective therapies, is critically dependent on technological innovation. As delineated in this work, a journey from centralised laboratory analysis to Point-of-Care (PoC) devices represented a first revolution, drastically reducing the time-to-result. However, the inherent limitation of providing mere snapshots of a patient's physiological state highlighted an unresolved need: the capacity for seamless, continuous data acquisition. It is within this gap that wearable electrochemical sensors emerge not merely as an incremental improvement, but as a foundational enabler for the Healthcare 4.0 paradigm. Their unique convergence of miniaturisation, digital compatibility, and analytical robustness positions them as the key technological vector to translate the principles of precision and personalised medicine from concept to daily practice. This dissertation is anchored in this vision, proceeding from the assertion that the development of such sensors must be guided by a holistic framework, exemplified by the REASSURED criteria, which prioritised not only analytical performance but also affordability, connectivity, and user-centric design to ensure real-world impact.

In this context, the infrastructure of wearable health is not merely a collection of devises, but a multi-layered ecosystem where the sensor acts as the critical hardware-software interference. By adhering to the REASSURED criteria, this thesis contributes to the 'edge-sensing' layer of this infrastructure, ensuring that high-quality biomedical data ca be generated at the source, e.g. the patient's skin, thereby reducing the computation and analytical burden on centralized healthcare systems.

Translating this vision into a functional device necessitates a meticulous convergence of material science and fabrication engineering. The sensor is not an abstract concept but a physical interface that must coexist harmoniously with the human body. Therefore, the foundational step involves the strategic selection of biocompatible and flexible substrates, such as PDMS, polyimide, or advanced textiles, that ensure patient safety, wearing comfort and mechanical resilience. Simultaneously, the choice of fabrication technique, whether it be screen-printing, 3D printing, or laser-induced graphene, dictates the feasibility of creating precise, reproducible, and cost-effective conductive architectures. This material and manufacturing toolkit is further refined through the deliberate

modification of the electrode surface. The integration of nanomaterials, conductive polymers, or synthetic receptors like Molecularly Imprinted Polymers (MIPs) is paramount to transcend mere signal detection and achieve the necessary specificity, sensitivity, and stability for reliable operation in complex biological fluids. Thus, the development of a wearable sensor is inherently a multi-disciplinary compromise, balancing electrochemical excellence with the imperative of seamless integration into the user's life.

The efficacy of this integrated approach is powerfully demonstrated by the development of a potentiometric sensor for monitoring lithium in bipolar disorders. This work directly addresses a critical clinical dilemma: managing a life-saving drug with an exceptionally narrow therapeutic window through invasive, infrequent blood tests. In response, the research translated the foundational principles into a practical solution. A graphite screen-printed electrode was functionalised via the electrodeposition of a bimetallic nanostructure of silver and gold, creating a high-surface-area solid contact that ensures stable potentiometric transduction. This functionalised substrate was then tailored for specificity by drop-casting a lithium-selective membrane. The resulting sensor achieved a near-Nernstian response across a physiologically relevant range with a detection limit of 1.6 10^{-6} M. Crucially, it maintained robust performance in the complex ionic fluid of synthetic sweat and saliva, demonstrating sufficient selectivity against common interfering cations. This successful translation from a material cointerventionncept to a validated analytical tool underscores the potential of such platforms to decentralised therapeutic drug monitoring, providing a clear proof-of-concept for non-invasive, frequent lithium assessment and enhancing personalised management for individuals with bipolar disorder.

Building upon this foundation, this research then advanced to address a more complex challenge: the non-invasive monitoring of neurological health through the detection of endogenous dopamine in sweat. This endeavour required a paradigm shift toward fully biocompatible materials to meet the safety demands of prolonged wear. The developed strategy centred on the electropolymerization of poly-L-cysteine (PLC), a sustainable, non-toxic-amino acid, based polymer, followed by the in-situ electrodeposition o1 mM gold nanoparticles (AuNPs). This AuNPs/PLC nanocomposite was further functionalised to create an interface that excels not only in biocompatibility but also in electrochemical performance. Characterisation revealed a platform with a large electroactive area and exceptionally fast electron transfer kinetics, a combination that translated into outstanding

analytical sensitivity for dopamine. The sensor demonstrated a wide linear range and a low detection limit in buffer, along with robust selectivity. Most importantly, it retained its core functionality in undiluted artificial sweat, achieving a clinically relevant detection limit. This work validates a crucial step beyond mere detection; it establishes a biocompatible sensing paradigm that prioritises safe integration with the body while maintaining high analytical performance, thereby laying a credible material foundation for future truly wearable, long-term neurological health monitors.

The logical culmination of this research trajectory is the integration of sensing and sample handling into a functional, self-contained prototype. This was achieved through the development of a microfluidic-electrochemical platform for the therapeutic monitoring of levodopa in Parkinson's disease. Here, a single, elegantly efficient oxygen plasma treatment served a dual and synergistic purpose. It simultaneously and permanently activated the carbon electrode surface — enhancing its electrocatalytic properties, doubling its electroactive area, and yielding a dramatic signal increase for levodopa, while rendering the PDMS microfluidic network hydrophilic to enable passive, capillary-driven sweat flow. This "all-in-one" fabrication process resulted in a sealed, robust device where the sensor operates within its intended microfluidic environment. The integrated platform successfully quantified levodopa in artificial sweat with a clinically applicable detection limit, without any sample pre-treatment. This final advancement bridges the gap between a high-performance sensing element and a practical wearable format, demonstrating a viable path toward autonomous, on-body therapeutic drug monitoring systems that require no external actuation or manual intervention.

The all-in-one plasma-driven fabrication process detailed in this work represents a significant contribution to the manufacturing infrastructure of wearable. By simplifying the assembly to the manufacturing infrastructure of wearables. By simplifying the assembly of microfluidic and electrochemical components into a single step, this approach addresses the scalability bottleneck. It demonstrates that the transition from laboratory prototypes to mass-producible, integrated ‘lab-on-a-skin’ systems is feasible through streamlined engineering, which is essential for the widespread deployment of therapeutic drug monitoring tools.

However, having established functional platforms for monitoring key analytes brought to light a more fundamental and intrinsic limitation to the entire field of wearable sensing: the reliance on biological recognition elements, such as antibodies, which are notoriously fragile, costly, and variable. The research therefore undertook a conceptual paradigm

shift, exploring the integration of synthetic receptors based on nanostructured molecularly imprinted polymers (nanoMIPs) with innovative laser-induced graphene (LIG) electrodes. This "nanoMIP-on-LIG" approach aims to replace biology with synthetic chemistry, ensuring robustness, reproducibility, and scalable fabrication. Comparative functional validation revealed that the intrinsic recognition affinity of the nanoMIPs is fully preserved when transferred from the flat surface of a conventional electrode to the three-dimensional, porous architecture of LIG. Indeed, the electrochemical signal transduction is amplified on the LIG platform, thanks to its greater effective surface area which allows for a higher loading of synthetic receptors. Furthermore, the nanoMIPs immobilized on LIG maintained high specificity, effectively discriminating between the target protein and unrelated proteins. This work, therefore, outlines a new paradigm for wearable affinity sensing, where molecular selectivity, durability, and adaptability to flexible substrates are achieved through materials engineering and synthetic chemistry, offering a robust alternative to fragile bio-inspired architectures.

This conceptual shift toward synthetic receptors (nanoMIPs) fundamentally redefines the logistic and maintenance infrastructure of wearable analytics. Unlike biosensors the require cold-chain storage and have limited shelf-life, nanoMIP-based device provide the environmental resilience necessary for global health applications and long-term home monitoring, ensuring that the infrastructure remains operational even in resource-limited settings or during prolonged patient use.

Looking forward, this research journey, which has spanned from fundamental principles to validation in complex matrices, from microfluidic integration to innovation in receptor materials, outlines a clear roadmap for the development of the next generation of wearable medical devices. The next steps must necessarily involve the *in vivo* validation of the most promising prototypes, to test their performance against the clinical gold standard under real conditions of use, addressing dynamic variables such as sweating rate, skin contamination, and long-term adaptation to the biological interface. In parallel, the integration of flexible electronics for signal processing, low-power wireless transmitters for data telemetry, and sustainable power solutions remains a crucial engineering challenge to enable truly continuous and autonomous monitoring. The versatility of the strategies developed, from biocompatible polymers to plasma activation, from synthetic receptors to porous carbon substrates, also invites the exploration of multi-analyte panels on a single device, and the extension of this sensing paradigm beyond neurological and

psychiatric disorders, towards other chronic conditions where continuous biomarker monitoring can revolutionize therapeutic management.

In conclusion, this doctoral research has advanced the field of wearable electrochemical sensing, progressing from fundamental material studies to the integration of functional prototypes, and ultimately to redefining the approach to molecular recognition itself. It has provided tangible solutions for the monitoring of critical analytes (such as lithium, dopamine, and levodopa) each representing a distinct challenge in personalized medicine. By consistently aligning technological development with the REASSURED criteria, the work has not only delivered sensitive and selective sensors but has also consciously addressed the intertwined requirements of biocompatibility, cost-effectiveness, and user-centric design. The journey documented in this thesis illustrates that the path toward effective wearable healthcare devices is paved by a conscious and iterative compromise between analytical rigor and practical integration. It is a path that leads from the laboratory bench toward the patient's skin, holding the promise of making continuous, personalized health monitoring an accessible and empowering reality.

8. References

[1] S. Ryu, Telemedicine: Opportunities and Developments in Member States: Report on the Second Global Survey on eHealth 2009 (Global Observatory for eHealth Series, Volume 2), Healthc Inform Res 18 (2012) 153. https://doi.org/10.4258/hir.2012.18.2.153.

[2] M. Stoltzfus, A. Kaur, A. Chawla, V. Gupta, F.N.U. Anamika, R. Jain, The role of telemedicine in healthcare: an overview and update, Egypt J Intern Med 35 (2023) 49. https://doi.org/10.1186/s43162-023-00234-z.

[3] J. Jagarapu, R.C. Savani, A brief history of telemedicine and the evolution of teleneonatology, Seminars in Perinatology 45 (2021) 151416. https://doi.org/10.1016/j.semperi.2021.151416.

[4] P.A. Anawade, D. Sharma, S. Gahane, A Comprehensive Review on Exploring the Impact of Telemedicine on Healthcare Accessibility, Cureus (2024). https://doi.org/10.7759/cureus.55996.

[5] W. Pfeil, P.L. Privalov, Thermodynamic investigations of proteins. III. Thermodynamic description of lysozyme, Biophys Chem 4 (1976) 41–50. https://doi.org/10.1016/0301-4622(76)80005-1.

[6] I.R. König, O. Fuchs, G. Hansen, E. Von Mutius, M.V. Kopp, What is precision medicine?, Eur Respir J 50 (2017) 1700391. https://doi.org/10.1183/13993003.00391-2017.

[7] K.K. Jain, Personalized medicine, Curr Opin Mol Ther 4 (2002) 548–558.

[8] S. Sugeir, S. Naylor, Critical Care and Personalized or Precision Medicine: Who needs whom?, Journal of Critical Care 43 (2018) 401–405. https://doi.org/10.1016/j.jcrc.2017.11.026.

[9] Toward Precision Medicine: Building a Knowledge Network for Biomedical Research and a New Taxonomy of Disease, National Academies Press, Washington, D.C., 2011. https://doi.org/10.17226/13284.
[10] L. Hood, M. Flores, A personal view on systems medicine and the emergence of proactive P4 medicine: predictive, preventive, personalized and participatory, New Biotechnology 29 (2012) 613–624. https://doi.org/10.1016/j.nbt.2012.03.004.
[11] J. Watkins, A. Marsh, P.C. Taylor, D.R. Singer, Personalized Medicine: the Impact on Chemistry, Therapeutic Delivery 1 (2010) 651–665. https://doi.org/10.4155/tde.10.64.
[12] P.P. Jayaraman, A.R.M. Forkan, A. Morshed, P.D. Haghighi, Y. Kang, Healthcare 4.0: A review of frontiers in digital health, WIREs Data Mining Knowl Discov 10 (2020). https://doi.org/10.1002/widm.1350.
[13] M. Zaninotto, M. Plebani, The "hospital central laboratory": automation, integration and clinical usefulness, Clinical Chemistry and Laboratory Medicine 48 (2010) 911–917. https://doi.org/10.1515/CCLM.2010.192.
[14] E. Imren-Eryilmaz, H. Kuzu-Karsilayan, A. Ogan, Spectrophotometric determination of leukocytes in urine, Clinical Laboratory Analysis 18 (2004) 251–254. https://doi.org/10.1002/jcla.20032.
[15] M.L. Efron, D. Young, H.W. Moser, R.A. MacCready, A Simple Chromatographic Screening Test for the Detection of Disorders of Amino Acid Metabolism: A Technic Using Whole Blood or Urine Collected on Filter Paper, N Engl J Med 270 (1964) 1378–1383. https://doi.org/10.1056/NEJM196406252702602.
[16] V. Vi´tek, K. Vi´tek, Chromatography ofsugars in body fluids, Journal of Chromatography A 60 (1971) 381–395. https://doi.org/10.1016/S0021-9673(00)95576-6.
[17] B. McArdle, The quantitative estimation of pyruvic and α-oxyglutaric acids by paper chromatography in blood, urine and cerebrospinal fluid, Biochemical Journal 66 (1957) 144–148. https://doi.org/10.1042/bj0660144.
[18] Y.Y. Li, S.J. Jones, Drug repositioning for personalized medicine, Genome Med 4 (2012) 27. https://doi.org/10.1186/gm326.
[19] E. Lee-Lewandrowski, K. Lewandrowski, Point-of-Care Testing: An Overview and a Look to the Future, Clinics in Laboratory Medicine 21 (2001) 217–240. https://doi.org/10.1016/S0272-2712(18)30031-3.
[20] A. Zarnegar, Point-of-Care Devices in Healthcare: A Public Health Perspective, in: K. Daimi, A. Alsadoon, S. Seabra Dos Reis (Eds.), Current and Future Trends in Health and Medical Informatics, Springer Nature Switzerland, Cham, 2023: pp. 75–92. https://doi.org/10.1007/978-3-031-42112-9_4.
[21] R. Rajendran, G. Rayman, Point-of-Care Blood Glucose Testing for Diabetes Care in Hospitalized Patients: An Evidence-Based Review, J Diabetes Sci Technol 8 (2014) 1081–1090. https://doi.org/10.1177/1932296814538940.
[22] J. Nayer, P. Aggarwal, S. Galwankar, Utility of point-of-care testing of natriuretic peptides (brain natriuretic peptide and n-terminal pro-brain natriuretic peptide) in the emergency department, Int J Crit Illn Inj Sci 4 (2014) 209. https://doi.org/10.4103/2229-5151.141406.
[23] V. Foerster, M. Severn, Point-of-Care Glycated Hemoglobin Testing to Diagnose Type 2 Diabetes, in: CADTH Issues in Emerging Health Technologies, Canadian Agency for Drugs and Technologies in Health, Ottawa (ON), 2016. http://www.ncbi.nlm.nih.gov/books/NBK476441/ (accessed December 23, 2025).

[24] C.F. Weber, K. Zacharowski, Perioperative Point of Care Coagulation Testing, Deutsches Ärzteblatt International (2012). https://doi.org/10.3238/arztebl.2012.0369.
[25] A. Di Cerbo, N. Quagliano, A. Napolitano, F. Pezzuto, T. Iannitti, A. Di Cerbo, Comparison between an Emerging Point-of-Care Tool for TSH Evaluation and a Centralized Laboratory-Based Method in a Cohort of Patients from Southern Italy, Diagnostics 11 (2021) 1590. https://doi.org/10.3390/diagnostics11091590.
[26] A.N. Konwar, V. Borse, Current status of point-of-care diagnostic devices in the Indian healthcare system with an update on COVID-19 pandemic, Sensors International 1 (2020) 100015. https://doi.org/10.1016/j.sintl.2020.100015.
[27] L.A. Cole, The hCG assay or pregnancy test, Clinical Chemistry and Laboratory Medicine 50 (2012). https://doi.org/10.1515/cclm.2011.808.
[28] J.K. Lu, W. Wang, J. Goh, A.B. Maier, A practical guide for selecting continuous monitoring wearable devices for community-dwelling adults, Heliyon 10 (2024) e33488. https://doi.org/10.1016/j.heliyon.2024.e33488.
[29] S. Burmaoglu, V. Trajkovik, T.L. Tutukalo, H. Yalcin, B. Caulfield, Evolution Map of Wearable Technology Patents for Healthcare Field, in: Wearable Technology in Medicine and Health Care, Elsevier, 2018: pp. 275–290. https://doi.org/10.1016/B978-0-12-811810-8.00014-2.
[30] X. Chen, D.-H. Kim, N. Lu, Introduction: Wearable Devices, Chem. Rev. 124 (2024) 6145–6147. https://doi.org/10.1021/acs.chemrev.4c00271.
[31] S.R. Mani Sekhar, S. Raj, G.M. Siddesh, Wearable technology and artificial intelligence in psychiatric disorders, in: Wearable Telemedicine Technology for the Healthcare Industry, Elsevier, 2022: pp. 53–70. https://doi.org/10.1016/B978-0-323-85854-0.00004-6.
[32] P. Grossman, The LifeShirt: a multi-function ambulatory system monitoring health, disease, and medical intervention in the real world, Stud Health Technol Inform 108 (2004) 133–141.
[33] V. Gold, A. McNaught, The International Union of Pure and Applied Chemistry (IUPAC), eds., The IUPAC Compendium of Chemical Terminology: The Gold Book, 5th ed., International Union of Pure and Applied Chemistry (IUPAC), Research Triangle Park, NC, 2025. https://doi.org/10.1351/goldbook.
[34] L. Eddaif, A. Shaban, Fundamentals of sensor technology, in: Advanced Sensor Technology, Elsevier, 2023: pp. 17–49. https://doi.org/10.1016/B978-0-323-90222-9.00003-0.
[35] Fundamentals of Sensor Technology, Elsevier, 2023. https://doi.org/10.1016/C2020-0-03445-6.
[36] J. Wang, Analytical Electrochemistry, 1st ed., Wiley, 2006. https://doi.org/10.1002/0471790303.
[37] S.M. Borisov, O.S. Wolfbeis, Optical Biosensors, Chem. Rev. 108 (2008) 423–461. https://doi.org/10.1021/cr068105t.
[38] H. Zhou, J. Liu, S. Zhang, Quantum dot-based photoelectric conversion for biosensing applications, TrAC Trends in Analytical Chemistry 67 (2015) 56–73. https://doi.org/10.1016/j.trac.2014.12.007.
[39] F. Lucarelli, S. Tombelli, M. Minunni, G. Marrazza, M. Mascini, Electrochemical and piezoelectric DNA biosensors for hybridisation detection, Analytica Chimica Acta 609 (2008) 139–159. https://doi.org/10.1016/j.aca.2007.12.035.

[40] K. Ramanathan, B. Danielsson, Principles and applications of thermal biosensors, Biosensors and Bioelectronics 16 (2001) 417–423. https://doi.org/10.1016/S0956-5663(01)00124-5.
[41] J. Llandro, J.J. Palfreyman, A. Ionescu, C.H.W. Barnes, Magnetic biosensor technologies for medical applications: a review, Med Biol Eng Comput 48 (2010) 977–998. https://doi.org/10.1007/s11517-010-0649-3.
[42] M. Madadelahi, F.O. Romero-Soto, R. Kumar, U.B. Tlaxcala, M.J. Madou, Electrochemical sensors: Types, applications, and the novel impacts of vibration and fluid flow for microfluidic integration, Biosensors and Bioelectronics 272 (2025) 117099. https://doi.org/10.1016/j.bios.2024.117099.
[43] J. Baranwal, B. Barse, G. Gatto, G. Broncova, A. Kumar, Electrochemical Sensors and Their Applications: A Review, Chemosensors 10 (2022) 363. https://doi.org/10.3390/chemosensors10090363.
[44] WHO Team, Global HIV, Hepatitis and STIs Programmes (HHS), Sexual and Reproductive Health and Research (SRH), Point-of-care tests for sexually transmitted infections: target product profiles, (2023). ISBN: 978-92-4-007710-2.
[45] K.J. Land, D.I. Boeras, X.-S. Chen, A.R. Ramsay, R.W. Peeling, REASSURED diagnostics to inform disease control strategies, strengthen health systems and improve patient outcomes, Nat Microbiol 4 (2018) 46–54. https://doi.org/10.1038/s41564-018-0295-3.
[46] G. Marrazza, M. Ramalingam, A. Jaisankar, L. Cheng, G. Selvolini, I.A. Vitale, Advancements and emerging technologies in biosensors for rapid and accurate virus detection, TrAC Trends in Analytical Chemistry 172 (2024) 117609. https://doi.org/10.1016/j.trac.2024.117609.
[47] R. Khan, Z. Khurshid, F. Yahya Ibrahim Asiri, Advancing Point-of-Care (PoC) Testing Using Human Saliva as Liquid Biopsy, Diagnostics 7 (2017) 39. https://doi.org/10.3390/diagnostics7030039.
[48] A. Taddeo, D. Prim, E.-D. Bojescu, J.-M. Segura, M.E. Pfeifer, Point-of-Care Therapeutic Drug Monitoring for Precision Dosing of Immunosuppressive Drugs, The Journal of Applied Laboratory Medicine 5 (2020) 738–761. https://doi.org/10.1093/jalm/jfaa067.
[49] K.H.J. Buschow, ed., Encyclopedia of materials: science and technology, Elsevier, Amsterdam ; New York, 2001.
[50] G. Liu, Z. Lv, S. Batool, M. Li, P. Zhao, L. Guo, Y. Wang, Y. Zhou, S. Han, Biocompatible Material-Based Flexible Biosensors: From Materials Design to Wearable/Implantable Devices and Integrated Sensing Systems, Small 19 (2023) 2207879. https://doi.org/10.1002/smll.202207879.
[51] H. Rashid, Z. Sheikh, F. Vohra, Allergic effects of the residual monomer used in denture base acrylic resins, Eur J Dent 09 (2015) 614–619. https://doi.org/10.4103/1305-7456.172621.
[52] M.T. Mohammed, Z.A. Khan, A.N. Siddiquee, Surface Modifications of Titanium Materials for developing Corrosion Behavior in Human Body Environment: A Review, Procedia Materials Science 6 (2014) 1610–1618. https://doi.org/10.1016/j.mspro.2014.07.144.
[53] J.M. Anderson, S. Jiang, Implications of the Acute and Chronic Inflammatory Response and the Foreign Body Reaction to the Immune Response of Implanted Biomaterials, in: B. Corradetti (Ed.), The Immune Response to Implanted Materials and Devices, Springer International Publishing, Cham, 2017: pp. 15–36. https://doi.org/10.1007/978-3-319-45433-7_2.

[54] V. Kini, S. C S, D. Mondal, N. Sundarabal, P. Nag, K. Sadani, Recent advances in electrochemical sensing and remediation technologies for ciprofloxacin, Environ Sci Pollut Res 32 (2025) 2210–2237. https://doi.org/10.1007/s11356-024-35852-9.
[55] K. Aoki, C. Zhang, J. Chen, T. Nishiumi, Fabrication of glass-coated electrodes with nano- and micrometer size by means of dissolution with HF, Electrochimica Acta 55 (2010) 7328–7333. https://doi.org/10.1016/j.electacta.2010.06.086.
[56] D. Qi, K. Zhang, G. Tian, B. Jiang, Y. Huang, Stretchable Electronics Based on PDMS Substrates, Advanced Materials 33 (2021) 2003155. https://doi.org/10.1002/adma.202003155.
[57] J. Chen, J. Zheng, Q. Gao, J. Zhang, J. Zhang, O. Omisore, L. Wang, H. Li, Polydimethylsiloxane (PDMS)-Based Flexible Resistive Strain Sensors for Wearable Applications, Applied Sciences 8 (2018) 345. https://doi.org/10.3390/app8030345.
[58] L. Li, L. Han, H. Hu, R. Zhang, A review on polymers and their composites for flexible electronics, Mater. Adv. 4 (2023) 726–746. https://doi.org/10.1039/D2MA00940D.
[59] W.-Y. Wu, X. Zhong, W. Wang, Q. Miao, J.-J. Zhu, Flexible PDMS-based three-electrode sensor, Electrochemistry Communications 12 (2010) 1600–1604. https://doi.org/10.1016/j.elecom.2010.09.005.
[60] K. Mahato, A. Srivastava, P. Chandra, Paper based diagnostics for personalized health care: Emerging technologies and commercial aspects, Biosensors and Bioelectronics 96 (2017) 246–259. https://doi.org/10.1016/j.bios.2017.05.001.
[61] C. Rial, I. Hussain, R. Hoff, S. Tompkins, D. Erickson, J. Branen, J.O. Giordano, Development and evaluation of a lateral flow-based portable optical system for determination of the pregnancy status of dairy cows, Journal of Dairy Science 107 (2024) 8642–8653. https://doi.org/10.3168/jds.2024-24899.
[62] I.H. Mahardika, J. Shin, J. Yukird, S.H. Lee, N. Pyun, B. Oh, K. Shin, From Pregnancy to Pathogens: Boosting Lateral Flow Assays Sensitivity with a Hydrogel Reaction Trap, Adv Materials Inter 11 (2024) 2400341. https://doi.org/10.1002/admi.202400341.
[63] V.B.C. Lee, N.F. Mohd-Naim, E. Tamiya, M.U. Ahmed, Trends in Paper-based Electrochemical Biosensors: From Design to Application, ANAL. SCI. 34 (2018) 7–18. https://doi.org/10.2116/analsci.34.7.
[64] P. Rider, Y. Carmi, E. Voronov, R.N. Apte, Interleukin-1α, Seminars in Immunology 25 (2013) 430–438. https://doi.org/10.1016/j.smim.2013.10.005.
[65] A.H. Rantamäki, S.K. Wiedmer, J.M. Holopainen, Melting Points—The Key to the Anti-Evaporative Effect of the Tear Film Wax Esters, Invest. Ophthalmol. Vis. Sci. 54 (2013) 5211. https://doi.org/10.1167/iovs.13-12408.
[66] J. Shu, Z. Zhou, H. Liang, X. Yang, Polyimide as a biomedical material: advantages and applications, Nanoscale Adv. 6 (2024) 4309–4324. https://doi.org/10.1039/D4NA00292J.
[67] N. Thakur, D. Mandal, T.C. Nagaiah, A novel NiVP/Pi-based flexible sensor for direct electrochemical ultrasensitive detection of cholesterol, Chem. Commun. 58 (2022) 2706–2709. https://doi.org/10.1039/D1CC07115G.
[68] G. Zhao, X. Wang, G. Liu, N. Thi Dieu Thuy, A disposable and flexible electrochemical sensor for the sensitive detection of heavy metals based on a one-step laser-induced surface modification: A new strategy for the batch fabrication of sensors, Sensors and Actuators B: Chemical 350 (2022) 130834. https://doi.org/10.1016/j.snb.2021.130834.

[69] J. Liu, H. Ji, X. Lv, C. Zeng, H. Li, F. Li, B. Qu, F. Cui, Q. Zhou, Laser-induced graphene (LIG)-driven medical sensors for health monitoring and diseases diagnosis, Microchim Acta 189 (2022) 54. https://doi.org/10.1007/s00604-021-05157-6.
[70] J.A. Schwarz, C.I. Contescu, K. Putyera, eds., Dekker encyclopedia of nanoscience and nanotechnology, M. Dekker, New York, 2004.
[71] T. Trantidou, M. Tariq, C. Terracciano, C. Toumazou, T. Prodromakis, Parylene C-Based Flexible Electronics for pH Monitoring Applications, Sensors 14 (2014) 11629–11639. https://doi.org/10.3390/s140711629.
[72] N. Chou, H. Moon, J. Park, S. Kim, Interfacial and surface analysis of parylene C-modified PDMS substrates for soft bioelectronics, Progress in Organic Coatings 157 (2021) 106309. https://doi.org/10.1016/j.porgcoat.2021.106309.
[73] D. Steck, J. Qu, S.B. Kordmahale, D. Tscharnuter, A. Muliana, J. Kameoka, Mechanical responses of Ecoflex silicone rubber: Compressible and incompressible behaviors, J of Applied Polymer Sci 136 (2019) 47025. https://doi.org/10.1002/app.47025.
[74] M. Amjadi, Y.J. Yoon, I. Park, Ultra-stretchable and skin-mountable strain sensors using carbon nanotubes–Ecoflex nanocomposites, Nanotechnology 26 (2015) 375501. https://doi.org/10.1088/0957-4484/26/37/375501.
[75] W. Zeng, L. Shu, Q. Li, S. Chen, F. Wang, X. Tao, Fiber-Based Wearable Electronics: A Review of Materials, Fabrication, Devices, and Applications, Advanced Materials 26 (2014) 5310–5336. https://doi.org/10.1002/adma.201400633.
[76] Z. Taleat, A. Khoshroo, M. Mazloum-Ardakani, Screen-printed electrodes for biosensing: a review (2008–2013), Microchim Acta 181 (2014) 865–891. https://doi.org/10.1007/s00604-014-1181-1.
[77] R.R. Suresh, M. Lakshmanakumar, J.B.B. Arockia Jayalatha, K.S. Rajan, S. Sethuraman, U.M. Krishnan, J.B.B. Rayappan, Fabrication of screen-printed electrodes: opportunities and challenges, J Mater Sci 56 (2021) 8951–9006. https://doi.org/10.1007/s10853-020-05499-1.
[78] O.D. Renedo, M.A. Alonso-Lomillo, M.J.A. Martínez, Recent developments in the field of screen-printed electrodes and their related applications, Talanta 73 (2007) 202–219. https://doi.org/10.1016/j.talanta.2007.03.050.
[79] J. Wiklund, A. Karakoç, T. Palko, H. Yiğitler, K. Ruttik, R. Jäntti, J. Paltakari, A Review on Printed Electronics: Fabrication Methods, Inks, Substrates, Applications and Environmental Impacts, JMMP 5 (2021) 89. https://doi.org/10.3390/jmmp5030089.
[80] L.K. Bommineedi, N. Upadhyay, R. Minnes, Screen Printing: An Ease Thin Film Technique, in: B.R. Sankapal, A. Ennaoui, R.B. Gupta, C.D. Lokhande (Eds.), Simple Chemical Methods for Thin Film Deposition, Springer Nature Singapore, Singapore, 2023: pp. 449–507. https://doi.org/10.1007/978-981-99-0961-2_11.
[81] B. Pérez-Fernández, A. Costa-García, A.D.L.E.- Muñiz, Electrochemical (Bio)Sensors for Pesticides Detection Using Screen-Printed Electrodes, Biosensors 10 (2020) 32. https://doi.org/10.3390/bios10040032.
[82] S. Wang, N. Liu, C. Yang, W. Liu, J. Su, L. Li, C. Yang, Y. Gao, Fully screen printed highly conductive electrodes on various flexible substrates for asymmetric supercapacitors, RSC Adv. 5 (2015) 85799–85805. https://doi.org/10.1039/C5RA16724H.
[83] W.T. Wahyuni, B.R. Putra, A. Fauzi, D. Ramadhanti, E. Rohaeti, R. Heryanto, A Brief Review on Fabrication of Screen-Printed Carbon Electrode: Materials and

Techniques, Indo. J. Chem. Res. 8 (2021) 210–218. https://doi.org/10.30598//ijcr.2021.7-wul.
[84] Y. Zhang, Y. Zhu, S. Zheng, L. Zhang, X. Shi, J. He, X. Chou, Z.-S. Wu, Ink formulation, scalable applications and challenging perspectives of screen printing for emerging printed microelectronics, Journal of Energy Chemistry 63 (2021) 498–513. https://doi.org/10.1016/j.jechem.2021.08.011.
[85] S. Zheng, H. Wang, P. Das, Y. Zhang, Y. Cao, J. Ma, S. (Frank) Liu, Z. Wu, Multitasking MXene Inks Enable High-Performance Printable Microelectrochemical Energy Storage Devices for All-Flexible Self-Powered Integrated Systems, Advanced Materials 33 (2021) 2005449. https://doi.org/10.1002/adma.202005449.
[86] Y. Aleeva, B. Pignataro, Recent advances in upscalable wet methods and ink formulations for printed electronics, J. Mater. Chem. C 2 (2014) 6436–6453. https://doi.org/10.1039/C4TC00618F.
[87] M.M. Voigt, A. Guite, D. Chung, R.U.A. Khan, A.J. Campbell, D.D.C. Bradley, F. Meng, J.H.G. Steinke, S. Tierney, I. McCulloch, H. Penxten, L. Lutsen, O. Douheret, J. Manca, U. Brokmann, K. Sönnichsen, D. Hülsenberg, W. Bock, C. Barron, N. Blanckaert, S. Springer, J. Grupp, A. Mosley, Polymer Field-Effect Transistors Fabricated by the Sequential Gravure Printing of Polythiophene, Two Insulator Layers, and a Metal Ink Gate, Adv Funct Materials 20 (2010) 239–246. https://doi.org/10.1002/adfm.200901597.
[88] A. Ambrosi, M. Pumera, 3D-printing technologies for electrochemical applications, Chem. Soc. Rev. 45 (2016) 2740–2755. https://doi.org/10.1039/C5CS00714C.
[89] J.T. Muth, D.M. Vogt, R.L. Truby, Y. Mengüç, D.B. Kolesky, R.J. Wood, J.A. Lewis, Embedded 3D Printing of Strain Sensors within Highly Stretchable Elastomers, Advanced Materials 26 (2014) 6307–6312. https://doi.org/10.1002/adma.201400334.
[90] J. Park, S. Kim, Three-Dimensionally Structured Flexible Fog Harvesting Surfaces Inspired by Namib Desert Beetles, Micromachines 10 (2019) 201. https://doi.org/10.3390/mi10030201.
[91] J.S. Stefano, C. Kalinke, R.G. Da Rocha, D.P. Rocha, V.A.O.P. Da Silva, J.A. Bonacin, L. Angnes, E.M. Richter, B.C. Janegitz, R.A.A. Muñoz, Electrochemical (Bio)Sensors Enabled by Fused Deposition Modeling-Based 3D Printing: A Guide to Selecting Designs, Printing Parameters, and Post-Treatment Protocols, Anal. Chem. 94 (2022) 6417–6429. https://doi.org/10.1021/acs.analchem.1c05523.
[92] C.L. Manzanares Palenzuela, M. Pumera, (Bio)Analytical chemistry enabled by 3D printing: Sensors and biosensors, TrAC Trends in Analytical Chemistry 103 (2018) 110–118. https://doi.org/10.1016/j.trac.2018.03.016.
[93] R. Ye, D.K. James, J.M. Tour, Laser-Induced Graphene, Acc. Chem. Res. 51 (2018) 1609–1620. https://doi.org/10.1021/acs.accounts.8b00084.
[94] J. Lin, Z. Peng, Y. Liu, F. Ruiz-Zepeda, R. Ye, E.L.G. Samuel, M.J. Yacaman, B.I. Yakobson, J.M. Tour, Laser-induced porous graphene films from commercial polymers, Nat Commun 5 (2014) 5714. https://doi.org/10.1038/ncomms6714.
[95] L.X. Duy, Z. Peng, Y. Li, J. Zhang, Y. Ji, J.M. Tour, Laser-induced graphene fibers, Carbon 126 (2018) 472–479. https://doi.org/10.1016/j.carbon.2017.10.036.
[96] X. Zang, C. Shen, Y. Chu, B. Li, M. Wei, J. Zhong, M. Sanghadasa, L. Lin, Laser-Induced Molybdenum Carbide–Graphene Composites for 3D Foldable Paper Electronics, Advanced Materials 30 (2018) 1800062. https://doi.org/10.1002/adma.201800062.

[97] Y. Chyan, R. Ye, Y. Li, S.P. Singh, C.J. Arnusch, J.M. Tour, Laser-Induced Graphene by Multiple Lasing: Toward Electronics on Cloth, Paper, and Food, ACS Nano 12 (2018) 2176–2183. https://doi.org/10.1021/acsnano.7b08539.
[98] J. Nasser, L. Groo, L. Zhang, H. Sodano, Laser induced graphene fibers for multifunctional aramid fiber reinforced composite, Carbon 158 (2020) 146–156. https://doi.org/10.1016/j.carbon.2019.11.078.
[99] Z. Zhang, M. Song, J. Hao, K. Wu, C. Li, C. Hu, Visible light laser-induced graphene from phenolic resin: A new approach for directly writing graphene-based electrochemical devices on various substrates, Carbon 127 (2018) 287–296. https://doi.org/10.1016/j.carbon.2017.11.014.
[100] K. Muzyka, G. Xu, Laser-induced Graphene in Facts, Numbers, and Notes in View of Electroanalytical Applications: A Review, Electroanalysis 34 (2022) 574–589. https://doi.org/10.1002/elan.202100425.
[101] R. Zaouk, B.Y. Park, M.J. Madou, Introduction to Microfabrication Techniques, in: Microfluidic Techniques, Humana Press, New Jersey, 2005: pp. 3–16. https://doi.org/10.1385/1-59259-997-4:3.
[102] A. Tanwar, H.A. Gandhi, D. Kushwaha, J. Bhattacharya, A review on microelectrode array fabrication techniques and their applications, Materials Today Chemistry 26 (2022) 101153. https://doi.org/10.1016/j.mtchem.2022.101153.
[103] V.M. Carriere, J.P. Rodrigues, C. Tan, P. Arumugam, S. Poh, In Vitro Electrochemical Detection of Hydrogen Peroxide in Activated Macrophages via a Platinum Microelectrode Array, Sensors 21 (2021) 5607. https://doi.org/10.3390/s21165607.
[104] Y. Wang, M. Wang, Y. Dai, Y. Song, Y. Wang, B. Lu, Y. Li, X. Cai, PtNPs/Short MWCNT-PEDOT: PSS-Modified Microelectrode Array to Detect Neuronal Firing Patterns in the Dorsal Raphe Nucleus and Hippocampus of Insomnia Rats, Micromachines 13 (2022) 488. https://doi.org/10.3390/mi13030488.
[105] Y.U. Kim, N.Y. Kwon, S.H. Park, C.W. Kim, H.D. Chau, M.H. Hoang, M.J. Cho, D.H. Choi, Patterned Sandwich-Type Silver Nanowire-Based Flexible Electrode by Photolithography, ACS Appl. Mater. Interfaces 13 (2021) 61463–61472. https://doi.org/10.1021/acsami.1c19164.
[106] P.J. Smith, A. Morrin, eds., Reactive Inkjet Printing: A Chemical Synthesis Tool, Royal Society of Chemistry, Cambridge, 2017. https://doi.org/10.1039/9781788010511.
[107] Y. Kim, S. Alimperti, P. Choi, M. Noh, An Inkjet Printed Flexible Electrocorticography (ECoG) Microelectrode Array on a Thin Parylene-C Film, Sensors 22 (2022) 1277. https://doi.org/10.3390/s22031277.
[108] A. Fendyur, M.E. Spira, Toward on-chip, in-cell recordings from cultured cardiomyocytes by arrays of gold mushroom-shaped microelectrodes, Front. Neuroeng. 5 (2012). https://doi.org/10.3389/fneng.2012.00021.
[109] N. Adly, S. Weidlich, S. Seyock, F. Brings, A. Yakushenko, A. Offenhäusser, B. Wolfrum, Printed microelectrode arrays on soft materials: from PDMS to hydrogels, Npj Flex Electron 2 (2018) 15. https://doi.org/10.1038/s41528-018-0027-z.
[110] P. Bongrand, Specific and Nonspecific Interactions in Cell Biology, Journal of Dispersion Science and Technology 19 (1998) 963–978. https://doi.org/10.1080/01932699808913226.
[111] N. Sandhyarani, Surface modification methods for electrochemical biosensors, in: Electrochemical Biosensors, Elsevier, 2019: pp. 45–75. https://doi.org/10.1016/B978-0-12-816491-4.00003-6.

[112] H. Bai, R. Wang, B. Hargis, H. Lu, Y. Li, A SPR Aptasensor for Detection of Avian Influenza Virus H5N1, Sensors 12 (2012) 12506–12518. https://doi.org/10.3390/s120912506.
[113] X. Qin, J. Zhang, W. Shao, X. Liu, X. Zhang, F. Chen, X. Qin, L. Wang, D. Luo, X. Qiao, Modification of electrodes with self-assembled, close-packed AuNPs for improved signal reproducibility toward electrochemical detection of dopamine, Electrochemistry Communications 133 (2021) 107161. https://doi.org/10.1016/j.elecom.2021.107161.
[114] T. Santhoshkumar, A.A. Rahuman, G. Rajakumar, S. Marimuthu, A. Bagavan, C. Jayaseelan, A.A. Zahir, G. Elango, C. Kamaraj, Synthesis of silver nanoparticles using Nelumbo nucifera leaf extract and its larvicidal activity against malaria and filariasis vectors, Parasitol Res 108 (2011) 693–702. https://doi.org/10.1007/s00436-010-2115-4.
[115] L.A. Dykman, N.G. Khlebtsov, Methods for chemical synthesis of colloidal gold, Russ. Chem. Rev. 88 (2019) 229–247. https://doi.org/10.1070/RCR4843.
[116] J.L. Cholula-Díaz, D. Lomelí-Marroquín, B. Pramanick, A. Nieto-Argüello, L.A. Cantú-Castillo, H. Hwang, Synthesis of colloidal silver nanoparticle clusters and their application in ascorbic acid detection by SERS, Colloids and Surfaces B: Biointerfaces 163 (2018) 329–335. https://doi.org/10.1016/j.colsurfb.2017.12.051.
[117] F.W. Campbell, R.G. Compton, The use of nanoparticles in electroanalysis: an updated review, Anal Bioanal Chem 396 (2010) 241–259. https://doi.org/10.1007/s00216-009-3063-7.
[118] Y. Takahashi, T. Tatsuma, Electrodeposition of thermally stable gold and silver nanoparticle ensembles through a thin alumina nanomask, Nanoscale 2 (2010) 1494. https://doi.org/10.1039/c0nr00230e.
[119] O. Kuntyi, A. Mazur, A. Kytsya, O. Karpenko, L. Bazylyak, I. Mertsalo, T. Pokynbroda, A. Prokopalo, Electrochemical synthesis of silver nanoparticles in solutions of rhamnolipid, Micro & Nano Letters 15 (2020) 802–807. https://doi.org/10.1049/mnl.2020.0195.
[120] J.M. Margolis, ed., Conductive Polymers and Plastics, Springer US, Boston, MA, 1989. https://doi.org/10.1007/978-1-4613-0851-5.
[121] H. Shirakawa, E.J. Louis, A.G. MacDiarmid, C.K. Chiang, A.J. Heeger, Synthesis of electrically conducting organic polymers: halogen derivatives of polyacetylene, (CH) x, J. Chem. Soc., Chem. Commun. (1977) 578. https://doi.org/10.1039/c39770000578.
[122] N. Aydemir, J. Malmström, J. Travas-Sejdic, Conducting polymer based electrochemical biosensors, Phys. Chem. Chem. Phys. 18 (2016) 8264–8277. https://doi.org/10.1039/C5CP06830D.
[123] D.G. Prajapati, B. Kandasubramanian, Progress in the Development of Intrinsically Conducting Polymer Composites as Biosensors, Macro Chemistry & Physics 220 (2019) 1800561. https://doi.org/10.1002/macp.201800561.
[124] S. Tajik, Z. Dourandish, K. Zhang, H. Beitollahi, Q.V. Le, H.W. Jang, M. Shokouhimehr, Carbon and graphene quantum dots: a review on syntheses, characterization, biological and sensing applications for neurotransmitter determination, RSC Adv. 10 (2020) 15406–15429. https://doi.org/10.1039/D0RA00799D.
[125] S. Tajik, H. Beitollahi, F.G. Nejad, I.S. Shoaie, M.A. Khalilzadeh, M.S. Asl, Q. Van Le, K. Zhang, H.W. Jang, M. Shokouhimehr, Recent developments in conducting polymers: applications for electrochemistry, RSC Adv. 10 (2020) 37834–37856. https://doi.org/10.1039/D0RA06160C.

[126] J.-M. Moon, N. Thapliyal, K.K. Hussain, R.N. Goyal, Y.-B. Shim, Conducting polymer-based electrochemical biosensors for neurotransmitters: A review, Biosensors and Bioelectronics 102 (2018) 540–552. https://doi.org/10.1016/j.bios.2017.11.069.
[127] N. Shoaie, M. Daneshpour, M. Azimzadeh, S. Mahshid, S.M. Khoshfetrat, F. Jahanpeyma, A. Gholaminejad, K. Omidfar, M. Foruzandeh, Electrochemical sensors and biosensors based on the use of polyaniline and its nanocomposites: a review on recent advances, Microchim Acta 186 (2019) 465. https://doi.org/10.1007/s00604-019-3588-1.
[128] R. Jain, N. Jadon, A. Pawaiya, Polypyrrole based next generation electrochemical sensors and biosensors: A review, TrAC Trends in Analytical Chemistry 97 (2017) 363–373. https://doi.org/10.1016/j.trac.2017.10.009.
[129] B.M. Hryniewicz, E.S. Orth, M. Vidotti, Enzymeless PEDOT-based electrochemical sensor for the detection of nitrophenols and organophosphates, Sensors and Actuators B: Chemical 257 (2018) 570–578. https://doi.org/10.1016/j.snb.2017.10.162.
[130] V. Papež, P. Novák, J. Pfleger, I. Kminek, S. Nešpúrek, The electrical and electrochemical characteristics of polyacetylene, Electrochimica Acta 32 (1987) 1087–1093. https://doi.org/10.1016/0013-4686(87)90037-5.
[131] A. Malinauskas, J. Malinauskiene, A. Ramanavičius, Conducting polymer-based nanostructurized materials: electrochemical aspects, Nanotechnology 16 (2005) R51–R62. https://doi.org/10.1088/0957-4484/16/10/R01.
[132] H.H. AL-Refai, A.A. Ganash, M.A. Hussein, Polythiophene and its derivatives – Based nanocomposites in electrochemical sensing: A mini review, Materials Today Communications 26 (2021) 101935. https://doi.org/10.1016/j.mtcomm.2020.101935.
[133] L.E. Ibarra, L. Tarres, S. Bongiovanni, C.A. Barbero, M.J. Kogan, V.A. Rivarola, M.L. Bertuzzi, E.I. Yslas, Assessment of polyaniline nanoparticles toxicity and teratogenicity in aquatic environment using Rhinella arenarum model, Ecotoxicology and Environmental Safety 114 (2015) 84–92. https://doi.org/10.1016/j.ecoenv.2015.01.013.
[134] J.R. Stetter, W.R. Penrose, S. Yao, Sensors, Chemical Sensors, Electrochemical Sensors, and ECS, J. Electrochem. Soc. 150 (2003) S11. https://doi.org/10.1149/1.1539051.
[135] H.K. Kordasht, M. Hasanzadeh, F. Seidi, P.M. Alizadeh, Poly (amino acids) towards sensing: Recent progress and challenges, TrAC Trends in Analytical Chemistry 140 (2021) 116279. https://doi.org/10.1016/j.trac.2021.116279.
[136] J.J. BelBruno, Molecularly Imprinted Polymers, Chem. Rev. 119 (2019) 94–119. https://doi.org/10.1021/acs.chemrev.8b00171.
[137] G. Selvolini, G. Marrazza, MIP-Based Sensors: Promising New Tools for Cancer Biomarker Determination, Sensors 17 (2017) 718. https://doi.org/10.3390/s17040718.
[138] A. Beltran, F. Borrull, R.M. Marcé, P.A.G. Cormack, Molecularly-imprinted polymers: useful sorbents for selective extractions, TrAC Trends in Analytical Chemistry 29 (2010) 1363–1375. https://doi.org/10.1016/j.trac.2010.07.020.
[139] T. Muhammad, Z. Nur, E.V. Piletska, O. Yimit, S.A. Piletsky, Rational design of molecularly imprinted polymer: the choice of cross-linker, Analyst 137 (2012) 2623. https://doi.org/10.1039/c2an35228a.

[140] B.-C. Iacob, A.E. Bodoki, L. Oprean, E. Bodoki, Metal–Ligand Interactions in Molecular Imprinting, in: C. Saravanan, B. Biswas (Eds.), Ligand, InTech, 2018. https://doi.org/10.5772/intechopen.73407.
[141] G. Vasapollo, R.D. Sole, L. Mergola, M.R. Lazzoi, A. Scardino, S. Scorrano, G. Mele, Molecularly Imprinted Polymers: Present and Future Prospective, IJMS 12 (2011) 5908–5945. https://doi.org/10.3390/ijms12095908.
[142] C. Malitesta, E. Mazzotta, R.A. Picca, A. Poma, I. Chianella, S.A. Piletsky, MIP sensors – the electrochemical approach, Anal Bioanal Chem 402 (2012) 1827–1846. https://doi.org/10.1007/s00216-011-5405-5.
[143] F. Canfarotta, A. Poma, A. Guerreiro, S. Piletsky, Solid-phase synthesis of molecularly imprinted nanoparticles, Nat Protoc 11 (2016) 443–455. https://doi.org/10.1038/nprot.2016.030.
[144] A.G. Ayankojo, J. Reut, V. Syritski, E. Sehit, Md Sharifuzzaman, Z. Altintas, Synthesis Techniques in Molecular Imprinting: From MIP Monoliths to MIP Films and Nanoparticles, in: Z. Altintas (Ed.), Molecularly Imprinted Polymers, Springer International Publishing, Cham, 2025: pp. 75–128. https://doi.org/10.1007/978-3-031-67368-9_4.
[145] K. Smolinska-Kempisty, O.S. Ahmad, A. Guerreiro, K. Karim, E. Piletska, S. Piletsky, New potentiometric sensor based on molecularly imprinted nanoparticles for cocaine detection, Biosensors and Bioelectronics 96 (2017) 49–54. https://doi.org/10.1016/j.bios.2017.04.034.
[146] S.A. Piletsky, K. Karim, E.V. Piletska, A.P.F. Turner, C.J. Day, K.W. Freebairn, C. Legge, Recognition of ephedrine enantiomers by molecularly imprinted polymers designed using a computational approach, Analyst 126 (2001) 1826–1830. https://doi.org/10.1039/b102426b.
[147] T. Cowen, K. Karim, S.A. Piletsky, Solubility and size of polymer nanoparticles, Polym. Chem. 9 (2018) 4566–4573. https://doi.org/10.1039/C8PY00829A.
[148] N.S. Moldovean-Cioroianu, I. Nicholls, Z. Altintas, Advanced Computational Approaches in Molecular Imprinting: Modeling Templates and in Silico Design of MIPs, in: Z. Altintas (Ed.), Molecularly Imprinted Polymers, Springer International Publishing, Cham, 2025: pp. 129–165. https://doi.org/10.1007/978-3-031-67368-9_5.
[149] S. Hyman, D. Chisholm, R. Kessler, V. Patel, H. Witheford, Mental Disorders, in: D.T. Jamison, J.G. Breman, A.R. Measham, G. Alleyne, M. Claeson, D.B. Evans, P. Jha, A. Mills, P. Musgrove (Eds.), Disease Control Priorities in Developing Countries, 2nd ed., The International Bank for Reconstruction and Development / The World Bank, Washington (DC), 2006. http://www.ncbi.nlm.nih.gov/books/NBK11766/ (accessed December 23, 2025).
[150] Comprehensive Mental Health Action Plan 2013-2030, 1st ed, World Health Organization, Geneva, 2021.
[151] S.E. Hyman, The Diagnosis of Mental Disorders: The Problem of Reification, Annu. Rev. Clin. Psychol. 6 (2010) 155–179. https://doi.org/10.1146/annurev.clinpsy.3.022806.091532.
[152] World Health Organization, ed., Pharmacological treatment of mental disorders in primary health care, World Health Organization, Geneva, 2009.
[153] R.S. McIntyre, M. Berk, E. Brietzke, B.I. Goldstein, C. López-Jaramillo, L.V. Kessing, G.S. Malhi, A.A. Nierenberg, J.D. Rosenblat, A. Majeed, E. Vieta, M. Vinberg, A.H. Young, R.B. Mansur, Bipolar disorders, The Lancet 396 (2020) 1841–1856. https://doi.org/10.1016/S0140-6736(20)31544-0.

[154] M. Dong, L. Lu, L. Zhang, Q. Zhang, G.S. Ungvari, C.H. Ng, Z. Yuan, Y. Xiang, G. Wang, Y.-T. Xiang, Prevalence of suicide attempts in bipolar disorder: a systematic review and meta-analysis of observational studies, Epidemiol Psychiatr Sci 29 (2020) e63. https://doi.org/10.1017/S2045796019000593.
[155] J.N. Miller, D.W. Black, Bipolar Disorder and Suicide: a Review, Curr Psychiatry Rep 22 (2020) 6. https://doi.org/10.1007/s11920-020-1130-0.
[156] World Health Organization, The selection and use of essential medicines 2023, Web Annex A, Model List of Essential Medicines (n.d.). https://iris.who.int/bitstream/handle/10665/371090/WHO-MHP-HPS-EML-2023.02-eng.pdf?sequence=1 (accessed December 23, 2025).
[157] A. Murru, M. Torra, A. Callari, I. Pacchiarotti, S. Romero, B. Gonzalez De La Presa, C. Varo, J.M. Goikolea, V. Pérez-Sola, E. Vieta, F. Colom, A study on the bioequivalence of lithium and valproate salivary and blood levels in the treatment of bipolar disorder, European Neuropsychopharmacology 27 (2017) 744–750. https://doi.org/10.1016/j.euroneuro.2017.06.003.
[158] V. Mani, T. Beduk, W. Khushaim, A.E. Ceylan, S. Timur, O.S. Wolfbeis, K.N. Salama, Electrochemical sensors targeting salivary biomarkers: A comprehensive review, TrAC Trends in Analytical Chemistry 135 (2021) 116164. https://doi.org/10.1016/j.trac.2020.116164.
[159] C.E. Krebs, A.P.S. Ori, A. Vreeker, T. Wu, R.M. Cantor, M.P.M. Boks, R.S. Kahn, L.M. Olde Loohuis, R.A. Ophoff, Whole blood transcriptome analysis in bipolar disorder reveals strong lithium effect, Psychol. Med. 50 (2020) 2575–2586. https://doi.org/10.1017/S0033291719002745.
[160] J. Kim, G. Valdés-Ramírez, A.J. Bandodkar, W. Jia, A.G. Martinez, J. Ramírez, P. Mercier, J. Wang, Non-invasive mouthguard biosensor for continuous salivary monitoring of metabolites, Analyst 139 (2014) 1632–1636. https://doi.org/10.1039/C3AN02359A.
[161] F. Criscuolo, F. Cantu, I. Taurino, S. Carrara, G. De Micheli, A Wearable Electrochemical Sensing System for Non-Invasive Monitoring of Lithium Drug in Bipolar Disorder, IEEE Sensors J. 21 (2021) 9649–9656. https://doi.org/10.1109/JSEN.2020.3009538.
[162] N. Elgrishi, K.J. Rountree, B.D. McCarthy, E.S. Rountree, T.T. Eisenhart, J.L. Dempsey, A Practical Beginner's Guide to Cyclic Voltammetry, J. Chem. Educ. 95 (2018) 197–206. https://doi.org/10.1021/acs.jchemed.7b00361.
[163] C. Maccà, Response time of ion-selective electrodes, Analytica Chimica Acta 512 (2004) 183–190. https://doi.org/10.1016/j.aca.2004.03.010.
[164] E. Bakker, E. Pretsch, Potentiometric sensors for trace-level analysis, TrAC Trends in Analytical Chemistry 24 (2005) 199–207. https://doi.org/10.1016/j.trac.2005.01.003.
[165] Y. Umezawa, P. Bühlmann, K. Umezawa, K. Tohda, S. Amemiya, Potentiometric Selectivity Coefficients of Ion-Selective Electrodes. Part I. Inorganic Cations (Technical Report), Pure and Applied Chemistry 72 (2000) 1851–2082. https://doi.org/10.1351/pac200072101851.
[166] V. Mazzaracchio, A. Serani, L. Fiore, D. Moscone, F. Arduini, All-solid state ion-selective carbon black-modified printed electrode for sodium detection in sweat, Electrochimica Acta 394 (2021) 139050. https://doi.org/10.1016/j.electacta.2021.139050.
[167] J. Gal, About a synthetic saliva for in vitro studies, Talanta 53 (2001) 1103–1115. https://doi.org/10.1016/S0039-9140(00)00618-4.

[168] I.A. Vitale, G. Selvolini, G. Marrazza, Lithium Detection in Peripheral Biofluids Using a Smart Electrochemical Sensor, in: S. Conoci, C. Di Natale, L. Prodi, G. Valenti (Eds.), Sensors and Microsystems, Springer Nature Switzerland, Cham, 2025: pp. 26–31. https://doi.org/10.1007/978-3-031-82076-2_4.
[169] I.A. Vitale, G. Selvolini, G. Marrazza, Smart Sensor for Lithium Detection: An Environmental Application, Chemosensors 11 (2023) 77. https://doi.org/10.3390/chemosensors11020077.
[170] Y. Lyu, S. Gan, Y. Bao, L. Zhong, J. Xu, W. Wang, Z. Liu, Y. Ma, G. Yang, L. Niu, Solid-Contact Ion-Selective Electrodes: Response Mechanisms, Transducer Materials and Wearable Sensors, Membranes 10 (2020) 128. https://doi.org/10.3390/membranes10060128.
[171] E.B. Miller, R.W. Pain, P.J. Skripal, Sweat Lithium in Manic-Depression, Br J Psychiatry 133 (1978) 477–478. https://doi.org/10.1192/bjp.133.5.477b.
[172] A.L. Suherman, B. Rasche, B. Godlewska, P. Nicholas, S. Herlihy, N. Caiger, P.J. Cowen, R.G. Compton, Electrochemical Detection and Quantification of Lithium Ions in Authentic Human Saliva Using $LiMn_2O_4$ -Modified Electrodes, ACS Sens. 4 (2019) 2497–2506. https://doi.org/10.1021/acssensors.9b01176.
[173] W.M. Carroll, The global burden of neurological disorders, The Lancet Neurology 18 (2019) 418–419. https://doi.org/10.1016/S1474-4422(19)30029-8.
[174] Valery L Feigin et al, Global, regional, and national burden of neurological disorders, 1990–2016: a systematic analysis for the Global Burden of Disease Study 2016, The Lancet Neurology 18 (2019) 459–480. https://doi.org/10.1016/S1474-4422(18)30499-X.
[175] World Health Organization, ATLAS: COUNTRY RESOURCES FOR NEUROLOGICAL DISORDERS., (2017). http://www.jstor.org/stable/resrep33099. Accessed 11 Dec. 2025.
[176] K.T. Thakur, E. Albanese, P. Giannakopoulos, N. Jette, M. Linde, M.J. Prince, T.J. Steiner, T. Dua, Neurological Disorders, in: V. Patel, D. Chisholm, T. Dua, R. Laxminarayan, M.E. Medina-Mora (Eds.), Mental, Neurological, and Substance Use Disorders: Disease Control Priorities, Third Edition (Volume 4), The International Bank for Reconstruction and Development / The World Bank, Washington (DC), 2016. http://www.ncbi.nlm.nih.gov/books/NBK361950/ (accessed December 23, 2025).
[177] L. Antoury, N. Hu, L. Balaj, S. Das, S. Georghiou, B. Darras, T. Clark, X.O. Breakefield, T.M. Wheeler, Analysis of extracellular mRNA in human urine reveals splice variant biomarkers of muscular dystrophies, Nat Commun 9 (2018) 3906. https://doi.org/10.1038/s41467-018-06206-0.
[178] K. Blennow, E. Vanmechelen, H. Hampel, CSF Total tau, Aβ42 and Phosphorylated tau Protein as Biomarkers for Alzheimer's Disease, MN 24 (2001) 087–098. https://doi.org/10.1385/MN:24:1-3:087.
[179] F. Ge, J. Ding, Y. Liu, H. Lin, T. Chang, Cerebrospinal fluid NFL in the differential diagnosis of parkinsonian disorders: A meta-analysis, Neuroscience Letters 685 (2018) 35–41. https://doi.org/10.1016/j.neulet.2018.07.030.
[180] K.J.B. Lamers, P. Vos, M.M. Verbeek, F. Rosmalen, W.J.A. Van Geel, B.G.M. Van Engelen, Protein S-100B, neuron-specific enolase (NSE), myelin basic protein (MBP) and glial fibrillary acidic protein (GFAP) in cerebrospinal fluid (CSF) and blood of neurological patients, Brain Research Bulletin 61 (2003) 261–264. https://doi.org/10.1016/S0361-9230(03)00089-3.
[181] L.A. Beckett, D.J. Harvey, A. Gamst, M. Donohue, J. Kornak, H. Zhang, J.H. Kuo, Alzheimer's Disease Neuroimaging Initiative, The Alzheimer's Disease

Neuroimaging Initiative: Annual change in biomarkers and clinical outcomes, Alzheimer's & Dementia 6 (2010) 257–264. https://doi.org/10.1016/j.jalz.2010.03.002.
[182] M.A. Findeis, The role of amyloid β peptide 42 in Alzheimer's disease, Pharmacology & Therapeutics 116 (2007) 266–286. https://doi.org/10.1016/j.pharmthera.2007.06.006.
[183] A.L. Stav, D. Aarsland, K.K. Johansen, E. Hessen, E. Auning, T. Fladby, Amyloid-β and α-synuclein cerebrospinal fluid biomarkers and cognition in early Parkinson's disease, Parkinsonism & Related Disorders 21 (2015) 758–764. https://doi.org/10.1016/j.parkreldis.2015.04.027.
[184] L.J.C. Van Waalwijk Van Doorn, M.J. Koel-Simmelink, U. Haußmann, H. Klafki, H. Struyfs, P. Linning, H.-J. Knölker, H. Twaalfhoven, H.B. Kuiperij, S. Engelborghs, P. Scheltens, M.M. Verbeek, E. Vanmechelen, J. Wiltfang, C.E. Teunissen, Validation of soluble amyloid-β precursor protein assays as diagnostic CSF biomarkers for neurodegenerative diseases, J. Neurochem. 137 (2016) 112–121. https://doi.org/10.1111/jnc.13527.
[185] C. Sharma, H. Woo, S.R. Kim, Addressing Blood–Brain Barrier Impairment in Alzheimer's Disease, Biomedicines 10 (2022) 742. https://doi.org/10.3390/biomedicines10040742.
[186] H. Wellington, R.W. Paterson, E. Portelius, U. Törnqvist, N. Magdalinou, N.C. Fox, K. Blennow, J.M. Schott, H. Zetterberg, Increased CSF neurogranin concentration is specific to Alzheimer disease, Neurology 86 (2016) 829–835. https://doi.org/10.1212/WNL.0000000000002423.
[187] D. Chung, A. Shum, G. Caraveo, GAP-43 and BASP1 in Axon Regeneration: Implications for the Treatment of Neurodegenerative Diseases, Front. Cell Dev. Biol. 8 (2020) 567537. https://doi.org/10.3389/fcell.2020.567537.
[188] M. Eller, D.R. Williams, α-Synuclein in Parkinson disease and other neurodegenerative disorders, Clinical Chemistry and Laboratory Medicine 49 (2011) 403–408. https://doi.org/10.1515/CCLM.2011.077.
[189] N. Sahara, J. Avila, eds., Tau oligomers, Frontiers Media SA, 2014. https://doi.org/10.3389/978-2-88919-261-8.
[190] A.S. Chen-Plotkin, R. Albin, R. Alcalay, D. Babcock, V. Bajaj, D. Bowman, A. Buko, J. Cedarbaum, D. Chelsky, M.R. Cookson, T.M. Dawson, R. Dewey, T. Foroud, M. Frasier, D. German, K. Gwinn, X. Huang, C. Kopil, T. Kremer, S. Lasch, K. Marek, J.A. Marto, K. Merchant, B. Mollenhauer, A. Naito, J. Potashkin, A. Reimer, L.S. Rosenthal, R. Saunders-Pullman, C.R. Scherzer, T. Sherer, A. Singleton, M. Sutherland, I. Thiele, M. Van Der Brug, K. Van Keuren-Jensen, D. Vaillancourt, D. Walt, A. West, J. Zhang, Finding useful biomarkers for Parkinson's disease, Sci. Transl. Med. 10 (2018) eaam6003. https://doi.org/10.1126/scitranslmed.aam6003.
[191] G.C. Jickling, F.R. Sharp, Blood Biomarkers of Ischemic Stroke, Neurotherapeutics 8 (2011) 349–360. https://doi.org/10.1007/s13311-011-0050-4.
[192] D. Voccia, M. Sosnowska, F. Bettazzi, G. Roscigno, E. Fratini, V. De Franciscis, G. Condorelli, R. Chitta, F. D'Souza, W. Kutner, I. Palchetti, Direct determination of small RNAs using a biotinylated polythiophene impedimetric genosensor, Biosensors and Bioelectronics 87 (2017) 1012–1019. https://doi.org/10.1016/j.bios.2016.09.058.
[193] F. Bettazzi, E. Hamid-Asl, C.L. Esposito, C. Quintavalle, N. Formisano, S. Laschi, S. Catuogno, M. Iaboni, G. Marrazza, M. Mascini, L. Cerchia, V. De Franciscis, G. Condorelli, I. Palchetti, Electrochemical detection of miRNA-222 by

use of a magnetic bead-based bioassay, Anal Bioanal Chem 405 (2013) 1025–1034. https://doi.org/10.1007/s00216-012-6476-7.
[194] A.R. Arshad, S.A. Sulaiman, A.A. Saperi, R. Jamal, N. Mohamed Ibrahim, N.A. Abdul Murad, MicroRNAs and Target Genes As Biomarkers for the Diagnosis of Early Onset of Parkinson Disease, Front. Mol. Neurosci. 10 (2017) 352. https://doi.org/10.3389/fnmol.2017.00352.
[195] P.T. Nelson, W.-X. Wang, B.W. Rajeev, MicroRNAs (miRNAs) in Neurodegenerative Diseases, Brain Pathology 18 (2008) 130–138. https://doi.org/10.1111/j.1750-3639.2007.00120.x.
[196] M. Asahina, A. Poudel, S. Hirano, Sweating on the palm and sole: physiological and clinical relevance, Clin Auton Res 25 (2015) 153–159. https://doi.org/10.1007/s10286-015-0282-1.
[197] Hideo. Uno, SYMPATHETIC INNERVATION OF THE SWEAT GLANDS AND PILORRECTOR MUSCLES OF MACAQUES AND HUMAN BEINGS, Journal of Investigative Dermatology 69 (1977) 112–120. https://doi.org/10.1111/1523-1747.ep12497915.
[198] T.M. Chalmers, C.A. Keele, THE NERVOUS AND CHEMICAL CONTROL OF SWEATING*, Br J Dermatol 64 (1952) 43–54. https://doi.org/10.1111/j.1365-2133.1952.tb16160.x.
[199] C.G. Crandall, Mechanisms and controllers of eccrine sweating in humans, Front Biosci S2 (2010) 685–696. https://doi.org/10.2741/s94.
[200] J. Warth, J.F. Desforges, Determinants of intracellular pH in the erythrocyte, Br J Haematol 29 (1975) 369–372. https://doi.org/10.1111/j.1365-2141.1975.tb01833.x.
[201] M.M. Raiszadeh, M.M. Ross, P.S. Russo, M.A. Schaepper, W. Zhou, J. Deng, D. Ng, A. Dickson, C. Dickson, M. Strom, C. Osorio, T. Soeprono, J.D. Wulfkuhle, E.F. Petricoin, L.A. Liotta, W.M. Kirsch, Proteomic Analysis of Eccrine Sweat: Implications for the Discovery of Schizophrenia Biomarker Proteins, J. Proteome Res. 11 (2012) 2127–2139. https://doi.org/10.1021/pr2007957.
[202] M.J. Nunes, C.M. Cordas, J.J.G. Moura, J.P. Noronha, L.C. Branco, Screening of Potential Stress Biomarkers in Sweat Associated with Sports Training, Sports Med - Open 7 (2021) 8. https://doi.org/10.1186/s40798-020-00294-3.
[203] N. Brasier, J. Eckstein, Sweat as a Source of Next-Generation Digital Biomarkers, Digit Biomark 3 (2019) 155–165. https://doi.org/10.1159/000504387.
[204] P.A. Di Sant'Agnese, R.C. Darling, G.A. Perera, E. Shea, Sweat electrolyte disturbances associated with childhood pancreatic disease, The American Journal of Medicine 15 (1953) 777–784. https://doi.org/10.1016/0002-9343(53)90169-7.
[205] World Health Organization, ed., Neurological disorders: public health challenges, World Health Organization, Geneva, 2006.
[206] J.F. Hernández-Rodríguez, D. Rojas, A. Escarpa, Electrochemical Sensing Directions for Next-Generation Healthcare: Trends, Challenges, and Frontiers, Anal. Chem. 93 (2021) 167–183. https://doi.org/10.1021/acs.analchem.0c04378.
[207] D. Thirumalai, M. Santhamoorthy, S.-C. Kim, H.-R. Lim, Conductive Polymer-Based Hydrogels for Wearable Electrochemical Biosensors, Gels 10 (2024) 459. https://doi.org/10.3390/gels10070459.
[208] S.A. Gheni, M.M. Ali, G.C. Ta, H.J. Harbin, S.A. Awad, Toxicity, Hazards, and Safe Handling of Primary Aromatic Amines, ACS Chem. Health Saf. 31 (2024) 8–21. https://doi.org/10.1021/acs.chas.3c00073.

[209] I.A. Vitale, G. Selvolini, S. Failli, C. Truzzi, G. Marrazza, Mercury Detection in Novel Foods by a Smart Pocket Sensor, Electroanalysis (2024) e202400192. https://doi.org/10.1002/elan.202400192.
[210] J. Yi, Y. Xianyu, Gold Nanomaterials-Implemented Wearable Sensors for Healthcare Applications, Adv Funct Materials 32 (2022) 2113012. https://doi.org/10.1002/adfm.202113012.
[211] C. Hartmanshenn, M. Scherholz, I.P. Androulakis, Physiologically-based pharmacokinetic models: approaches for enabling personalized medicine, J Pharmacokinet Pharmacodyn 43 (2016) 481–504. https://doi.org/10.1007/s10928-016-9492-y.
[212] F. Durães, M. Pinto, E. Sousa, Old Drugs as New Treatments for Neurodegenerative Diseases, Pharmaceuticals 11 (2018) 44. https://doi.org/10.3390/ph11020044.
[213] J. Siegfried, W.H. Ziegler, F. Regli, C. Fischer, W. Kaufmann, E. Perret, Treatment of parkinsonism with L-DOPA in association with a decarboxylase inhibitor: First objective results, Pharmacol. Clin. 2 (1969) 23–26. https://doi.org/10.1007/BF00404181.
[214] R. Katzenschlager, A.J. Lees, Treatment of Parkinson's disease: levodopa as the first choice, Journal of Neurology 249 (2002) 1–1. https://doi.org/10.1007/s00415-002-1204-4.
[215] L.M. Ambani, M.H. Van Woert, Start Hesitation — A Side Effect of Long-Term Levodopa Therapy, N Engl J Med 288 (1973) 1113–1115. https://doi.org/10.1056/NEJM197305242882108.
[216] U.K. Rinne, Problems associated with long-term levodopa treatment of Parkinson's disease, Acta Neurologica Scandinavica 68 (1983) 19–26. https://doi.org/10.1111/j.1600-0404.1983.tb01513.x.
[217] M. Tsunoda, M. Hirayama, T. Tsuda, K. Ohno, Noninvasive monitoring of plasma l-dopa concentrations using sweat samples in Parkinson's disease, Clinica Chimica Acta 442 (2015) 52–55. https://doi.org/10.1016/j.cca.2014.12.032.
[218] S. Tajik, M.A. Taher, H. Beitollahi, First Report for Electrochemical Determination of Levodopa and Cabergoline: Application for Determination of Levodopa and Cabergoline in Human Serum, Urine and Pharmaceutical Formulations, Electroanalysis 26 (2014) 796–806. https://doi.org/10.1002/elan.201300589.
[219] R.G. State, J. (Koos) F. Van Staden, Review. Electrochemical sensors used in the determination of L -Dopa, Electrochemical Science Adv 2 (2022) e2100040. https://doi.org/10.1002/elsa.202100040.
[220] I.A. Vitale, N. Fuochi, D. Martella, C. Parmeggiani, G. Marrazza, I. Palchetti, Skin-contact wearable electrochemical biosensing tools: A perspective for the wellbeing of neurological patients, TrAC Trends in Analytical Chemistry 180 (2024) 117965. https://doi.org/10.1016/j.trac.2024.117965.
[221] J. Moon, H. Teymourian, E. De La Paz, J.R. Sempionatto, K. Mahato, T. Sonsa-ard, N. Huang, K. Longardner, I. Litvan, J. Wang, Non-Invasive Sweat-Based Tracking of L-Dopa Pharmacokinetic Profiles Following an Oral Tablet Administration, Angewandte Chemie Intl Edit 60 (2021) 19074–19078. https://doi.org/10.1002/anie.202106674.
[222] J. Xiao, C. Fan, T. Xu, L. Su, X. Zhang, An electrochemical wearable sensor for levodopa quantification in sweat based on a metal–Organic framework/graphene oxide composite with integrated enzymes, Sensors and Actuators B: Chemical 359 (2022) 131586. https://doi.org/10.1016/j.snb.2022.131586.

[223] D.L. Glasco, A. Sheelam, N.H.B. Ho, J.G. Bell, Smartphone-based detection of levodopa in human sweat using 3D printed sensors, Analytica Chimica Acta 1273 (2023) 341546. https://doi.org/10.1016/j.aca.2023.341546.
[224] M. Zoroddu, S. Medici, A. Ledda, V. Nurchi, J. Lachowicz, M. Peana, Toxicity of Nanoparticles, CMC 21 (2014) 3837–3853. https://doi.org/10.2174/09298673216661406011623 14.
[225] G. Paimard, E. Ghasali, M. Baeza, Screen-Printed Electrodes: Fabrication, Modification, and Biosensing Applications, Chemosensors 11 (2023) 113. https://doi.org/10.3390/chemosensors11020113.
[226] S.M.A. Iqbal, I. Mahgoub, E. Du, M.A. Leavitt, W. Asghar, Advances in healthcare wearable devices, Npj Flex Electron 5 (2021). https://doi.org/10.1038/s41528-021-00107-x.
[227] N.P. Shetti, A. Mishra, S. Basu, R.J. Mascarenhas, R.R. Kakarla, T.M. Aminabhavi, Skin-Patchable Electrodes for Biosensor Applications: A Review, ACS Biomater. Sci. Eng. 6 (2020) 1823–1835. https://doi.org/10.1021/acsbiomaterials.9b01659.
[228] I. Miranda, A. Souza, P. Sousa, J. Ribeiro, E.M.S. Castanheira, R. Lima, G. Minas, Properties and Applications of PDMS for Biomedical Engineering: A Review, JFB 13 (2021) 2. https://doi.org/10.3390/jfb13010002.
[229] D. Maji, S.K. Lahiri, S. Das, Study of hydrophilicity and stability of chemically modified PDMS surface using piranha and KOH solution, Surface & Interface Analysis 44 (2012) 62–69. https://doi.org/10.1002/sia.3770.
[230] D. Bodas, C. Khan-Malek, Formation of more stable hydrophilic surfaces of PDMS by plasma and chemical treatments, Microelectronic Engineering 83 (2006) 1277–1279. https://doi.org/10.1016/j.mee.2006.01.195.
[231] C. Ingrosso, G.V. Bianco, V. Pifferi, P. Guffanti, F. Petronella, R. Comparelli, A. Agostiano, M. Striccoli, I. Palchetti, L. Falciola, M.L. Curri, G. Bruno, Enhanced photoactivity and conductivity in transparent TiO_2 nanocrystals/graphene hybrid anodes, J. Mater. Chem. A 5 (2017) 9307–9315. https://doi.org/10.1039/C7TA01425B.
[232] I. Palchetti, S. Laschi, G. Marrazza, M. Mascini, Electrochemical Imaging of Localized Sandwich DNA Hybridization Using Scanning Electrochemical Microscopy, Anal. Chem. 79 (2007) 7206–7213. https://doi.org/10.1021/ac070474h.
[233] C. Ingrosso, M. Corricelli, A. Testolin, V. Pifferi, F. Bettazzi, G.V. Bianco, N. Depalo, E. Fanizza, M. Striccoli, I. Palchetti, M.L. Curri, L. Falciola, Au nanoparticle decorated reduced graphene oxide and its electroanalytical characterization for label free dopamine detection, Mater. Adv. 5 (2024) 549–560. https://doi.org/10.1039/D3MA00785E.
[234] F. Berti, L. Lozzi, I. Palchetti, S. Santucci, G. Marrazza, Aligned carbon nanotube thin films for DNA electrochemical sensing, Electrochimica Acta 54 (2009) 5035–5041. https://doi.org/10.1016/j.electacta.2009.01.038.
[235] C.J. Harvey, R.F. LeBouf, A.B. Stefaniak, Formulation and stability of a novel artificial human sweat under conditions of storage and use, Toxicology in Vitro 24 (2010) 1790–1796. https://doi.org/10.1016/j.tiv.2010.06.016.
[236] E.R. Kirch, T. Cornbleet, O. Bergeim, Ascorbic Acid in Sweat, Experimental Biology and Medicine 54 (1943) 307–308. https://doi.org/10.3181/00379727-54-14415.
[237] J.W.H. Mali, D. Spruit, E. Seutter, Chelation in human sweat, Clinica Chimica Acta 9 (1964) 187–190. https://doi.org/10.1016/0009-8981(64)90016-6.

[238] E.C. Wilkirson, K.L. Singampalli, J. Li, D.D. Dixit, X. Jiang, D.H. Gonzalez, P.B. Lillehoj, Affinity-based electrochemical sensors for biomolecular detection in whole blood, Anal Bioanal Chem 415 (2023) 3983–4002. https://doi.org/10.1007/s00216-023-04627-5.
[239] E. Engvall, P. Perlmann, Enzyme-linked immunosorbent assay (ELISA) quantitative assay of immunoglobulin G, Immunochemistry 8 (1971) 871–874. https://doi.org/10.1016/0019-2791(71)90454-X.
[240] J. Tu, R.M. Torrente-Rodríguez, M. Wang, W. Gao, The Era of Digital Health: A Review of Portable and Wearable Affinity Biosensors, Adv Funct Materials 30 (2020) 1906713. https://doi.org/10.1002/adfm.201906713.
[241] M.A. Arnold, M.E. Meyerhoff, Ion-selective electrodes, Anal. Chem. 56 (1984) 20–48. https://doi.org/10.1021/ac00269a003.
[242] S.K. Sharma, N. Sehgal, A. Kumar, Biomolecules for development of biosensors and their applications, Current Applied Physics 3 (2003) 307–316. https://doi.org/10.1016/S1567-1739(02)00219-5.
[243] Y. Chen, Z. Wang, Y. Liu, X. Wang, Y. Li, P. Ma, B. Gu, H. Li, Recent advances in rapid pathogen detection method based on biosensors, Eur J Clin Microbiol Infect Dis 37 (2018) 1021–1037. https://doi.org/10.1007/s10096-018-3230-x.
[244] O. Hosu, G. Selvolini, C. Cristea, G. Marrazza, Electrochemical Immunosensors for Disease Detection and Diagnosis, CMC 25 (2018) 4119–4137. https://doi.org/10.2174/0929867324666170727104429.
[245] S. Patel, R. Nanda, S. Sahoo, E. Mohapatra, Biosensors in Health Care: The Milestones Achieved in Their Development towards Lab-on-Chip-Analysis, Biochemistry Research International 2016 (2016) 1–12. https://doi.org/10.1155/2016/3130469.
[246] O.I. Guliy, S.S. Evstigneeva, L.A. Dykman, Recombinant antibodies by phage display for bioanalytical applications, Biosensors and Bioelectronics 222 (2023) 114909. https://doi.org/10.1016/j.bios.2022.114909.
[247] J.K. Scott, G.P. Smith, Searching for Peptide Ligands with an Epitope Library, Science 249 (1990) 386–390. https://doi.org/10.1126/science.1696028.
[248] C. Zhu, Z. Feng, H. Qin, L. Chen, M. Yan, L. Li, F. Qu, Recent progress of SELEX methods for screening nucleic acid aptamers, Talanta 266 (2024) 124998. https://doi.org/10.1016/j.talanta.2023.124998.
[249] Z. Zhang, B.R. Adhikari, P. Sen, L. Soleymani, Y. Li, Functional nucleic acid-based biosensors for virus detection, Advanced Agrochem (2023) S2773237123000539. https://doi.org/10.1016/j.aac.2023.07.006.
[250] C. Laflamme, P.M. McKeever, R. Kumar, J. Schwartz, M. Kolahdouzan, C.X. Chen, Z. You, F. Benaliouad, O. Gileadi, H.M. McBride, T.M. Durcan, A.M. Edwards, L.M. Healy, J. Robertson, P.S. McPherson, Implementation of an antibody characterization procedure and application to the major ALS/FTD disease gene C9ORF72, eLife 8 (2019) e48363. https://doi.org/10.7554/eLife.48363.
[251] O.I. Parisi, F. Francomano, M. Dattilo, F. Patitucci, S. Prete, F. Amone, F. Puoci, The Evolution of Molecular Recognition: From Antibodies to Molecularly Imprinted Polymers (MIPs) as Artificial Counterpart, JFB 13 (2022) 12. https://doi.org/10.3390/jfb13010012.
[252] B. Tse Sum Bui, A. Mier, K. Haupt, Molecularly Imprinted Polymers as Synthetic Antibodies for Protein Recognition: The Next Generation, Small 19 (2023) 2206453. https://doi.org/10.1002/smll.202206453.

[253] H. Wang, Z. Zhao, P. Liu, X. Guo, Laser-Induced Graphene Based Flexible Electronic Devices, Biosensors 12 (2022) 55. https://doi.org/10.3390/bios12020055.
[254] Z. Altintas, M.J. Abdin, A.M. Tothill, K. Karim, I.E. Tothill, Ultrasensitive detection of endotoxins using computationally designed nanoMIPs, Analytica Chimica Acta 935 (2016) 239–248. https://doi.org/10.1016/j.aca.2016.06.013.
[255] C. Herrera León, N.A. Kalacas, A. Mier, P. Sakhaii, F. Merlier, E. Prost, I. Maffucci, V. Montagna, H. Mora-Radó, P.K. Dhal, B. Tse Sum Bui, K. Haupt, Synthetic Peptide Antibodies as TNF-α Inhibitors: Molecularly Imprinted Polymer Nanogels Neutralize the Inflammatory Activity of TNF-α in THP-1 Derived Macrophages, Angew Chem Int Ed 62 (2023) e202306274. https://doi.org/10.1002/anie.202306274.
[256] E. Akin, E. Sehit, N.S. Moldovean-Cioroianu, S. Tavaragondi, S. Slenczka, R. Süssmuth, F. Jurk, M.V. Gemmeren, Z. Altintas, Atomic-Level Engineering of Synthetic Receptors for Enhanced Virus Detection and Removal, Adv Healthcare Materials 14 (2025) 2502043. https://doi.org/10.1002/adhm.202502043.
[257] A. Behrent, C. Griesche, P. Sippel, A.J. Baeumner, Correction to: Process-property correlations in laser-induced graphene electrodes for electrochemical sensing, Microchim Acta 188 (2021) 248. https://doi.org/10.1007/s00604-021-04904-z.